FATIGUE DAMAGE ACCUMULATION IN TITANIUM ALLOY IMI 834

By

Gavin James Baxter

Vol 1

Thesis submitted for the degree of Doctor of Philosophy

Department of Engineering Materials

University of Sheffield

May 1994

FATIGUE DAMAGE ACCUMULATION IN TITANIUM ALLOY IMI 834

BY G. J. BAXTER

SUMMARY OF THESIS

As current aerospace materials are subjected in service to increasingly onerous conditions of stress and temperature, the hazard of fatigue failure becomes more acute. Engineers utilise the methodology of fracture mechanics to estimate fatigue crack growth rates but fatigue crack initiation, which involves the interplay of many microprocesses, is only investigated empirically. The aim of this study was to investigate the fatigue damage accumulation mechanisms in the titanium alloy IMI 834 in order to develop a fundamental understanding of the controlling physical processes and the micromechanisms which occur at the dislocation level.

Load controlled four point bend test specimens of IMI 834 were cyclically fatigued to failure with an R ratio of 0.1 over a range of maximum stress levels and the fatigue and fracture surfaces were examined by optical and scanning electron microscopy. The examination of cross-sectional foils prepared from the fatigue surface enabled the fatigue damage to be examined in the T.E.M. as a function of orientation and depth below the specimen surface. The distribution, orientation and type of slip bands were identified in the primary-α and the transformed-β grains, and their interaction with secondary phases, precipitates and grain boundaries was determined.

The results show that fatigue damage accumulation in IMI 834 occurs primarily on basal slip bands in the primary-α phase and on basal and prismatic slip bands in the transformed-β phase. The segregation of α-stabilising elements to the primary-α phase during alloy processing allows the formation of an ordered phase which increases the propensity for planar slip on the basal plane. A mechanism for fatigue crack initiation along this plane is proposed. In addition, the occurrence and identification of an interface phase is discussed in the light of current theories regarding this phase.

VOLUME 1

CONTENTS

VOLUME 1

VOLUME 2

ABBREVIATIONS

a	crack length
$\underline{a}$	lattice parameter
α	titanium alloy phase with hexagonal close packed crystal structure
α_2	ordered coherent phase Ti_3Al
α'	titanium martensite
a_0	initial defect size
a_f	final crack size
Al*	aluminium equivalent
at%	atomic percent
b	specimen breadth
$\underline{b}$	Burgers vector
β	titanium alloy phase with body centred cubic crystal structure
b_x	microstructural barrier of magnitude x
B	electron beam direction
bcc	body centred cubic
$\dot{\gamma}$	strain rate
γ	intermetallic compound (*eg.* TiAl)
$\underline{c}$	lattice parameter
CP	commercially pure grade of titanium
CRSS	critical resolved shear stress
d	spacing of crystal planes
d	specimen depth
ΔK	stress intensity factor range
$\Delta\sigma$	cyclic stress range (Nm^{-2})
E	Young's modulus (GPa)
fcc	face centred cubic
F_{max}	maximum force
F_{mean}	mean force
F_{min}	minimum force
$\underline{g}$	reciprocal lattice vector
hcp	hexagonal close packed
(hkl)	Miller indices
(hkil)	Miller-Bravais indices
IFP	interface phase

IMI	Imperial Metal Industries
θ	X-ray diffraction angle
θ	angle between fatigue surface and slip band
K	Kelvin
K_{1c}	plane strain fracture toughness
K_Q	provisional value of K_{1c}
λ	angle between stress axis and slip plane direction
LCF	low cycle fatigue
L.E.F.M.	linear elastic fracture mechanics
μ	modulus of τ_μ
MSC	microstructurally short crack
N	number of cycles
N_f	number of cycles to failure
ppm	parts per million
P.S.	proof stress
P.S.B.	persistent slip band
PSC	physically short crack
R	stress ratio
S	applied stress in fatigue
S.E.M.	scanning electron microscope/microscopy
σ_s	shear stress resolved on slip plane
σ_n	applied stress
σ_{ps}	0.2% proof stress
σ_v	standard deviation
STEM	scanning transmission electron microscopy
T.E.M.	transmission electron microscope/microscopy
T_m	melting temperature
τ_μ	athermal component of the critical resolved shear stress
τ^*	thermal component of the critical resolved shear stress
u′	projected direction of dislocation/slip band
U	true line sense of dislocation/slip band
U.T.S.	ultimate tensile stress
ϕ	angle between g vector and u′ on a great circle
ϕ	angle between stress axis and slip plane normal
$v/_o$	volume fraction
wt%	weight percent

CHAPTER ONE

INTRODUCTION

1.1 FATIGUE LIFE PREDICTION

The purpose of an aero engine is to provide an aircraft with propulsion. However, to economically achieve this function, weight and fuel efficiency criteria must be satisfied which results in components being subjected to high stresses and high temperatures. Under these conditions individual engine components are at a consequent risk of failure. The fracture and possible disintegration of the rotating components such as the compressor discs and the high-pressure casings can potentially cause the greatest damage to an aircraft engine.

To reliably predict the service life of an aero engine component requires a sound knowledge of all the factors which affect the performance of the material, including the microstructure, surface finish, residual stresses and the service environment. Three criteria have been established to assess possible component failure; (i) low cycle fatigue (LCF) limitations, (ii) overstress requirements and (iii) the limitation of vibratory stresses [1]. The majority of components are removed from service because of their LCF limitations. In order to provide a balance between safety and economics, great emphasis must be placed on the reliability of the low cycle fatigue prediction methods.

Traditionally, total fatigue life analysis relies on full scale component testing to statistically define a minimum life for each component. All such components are then withdrawn from service before they reach two thirds of the predicted life to failure (the predicted safe cyclic life). However, although full scale component testing

guarantees a direct fatigue life prediction, it is expensive and time consuming to perform a statistically relevant number of full scale tests. Hence it is far more economical for testing to be performed on the scale of laboratory specimens. To be able to correlate the fatigue life of a specimen to that of full scale components requires a database of results and a full understanding of the fatigue process and material behaviour [1].

1.2 HIGH TEMPERATURE TITANIUM ALLOYS

Titanium and its alloys have been used extensively since the early 1950's in both airframe and aero engine applications as high temperature, high strength-to-weight ratio materials. The most predominant and most widely used titanium alloy, IMI 318 or Ti-6Al-4V, was introduced in 1954 and still accounts for nearly 50% of the market for titanium alloys. After forty years of intensive development, the applications of titanium alloys have significantly advanced [2-6]. IMI 829, an established leader in the high temperature titanium alloy field, has been developed specifically for gas turbine aero engine components and has a maximum operating temperature of 550°C, the highest temperature at which any titanium alloy is currently reputed to be in commercial use [7]. A total weight saving of over 50 Kg is achieved by using IMI 829 as a replacement for nickel and steel in the compressor discs, rear cone and turbine blades of the Rolls-Royce RB211-535E4 engine [4]. Two titanium alloys, IMI 834 and Ti-1100, have been developed for use up to higher operating temperatures by utilising conventional alloying techniques [8, 9]. IMI 834 is being designed for potential use in the high pressure condensers of the Trent engine at temperatures up to 600°C. A possible 85 Kg weight saving over the existing design is envisaged [10].

The tensile strength and creep performance targets in the early 1950's were modest in comparison to modern aero engine requirements. With the development of more highly

alloyed and more microstructurally complex titanium alloys titanium alloy disc designs have become fatigue limited rather than creep limited [9], hence research is concentrating on the need to maximise the all-round alloy capabilities. In addition, designers are looking to utilise as much of a component's fatigue life as possible before withdrawing it from service. This places great emphasis on the reliability of current fatigue life predictions. Consequently, an understanding of the fatigue behaviour of high temperature titanium alloys is of the utmost importance.

In order to predict how high temperature alloys will perform in service, it is essential to acquire detailed knowledge of all the stages of fatigue deformation from the damage accumulation stage to final failure. The majority of titanium alloy research to date has concentrated on the short and long fatigue crack growth behaviour of alloys. Both long and short crack growth behaviour are predicted using L.E.F.M.[1] and elasto-plastic modelling. However, as the microstructure of the alloys is refined and the demands on the fatigue integrity are increased, the application of these models is limited, thus a more fundamental understanding of the processes leading to fatigue crack initiation is required. The intrusion/extrusion mechanisms of fatigue crack initiation in lightly alloyed fcc metals, such as copper, are well understood, but an understanding of fatigue crack initiation behaviour in more complex alloys, such as those of titanium, is still in its infancy.

1.3 PROJECT AIMS

The aims of this investigation are:

* To characterise the as received IMI 834 microstructure in terms of the grain sizes, texture, phases, precipitates and dislocations present.

1 L.E.F.M = linear elastic fracture mechanics

* To cyclically fatigue specimens of the alloy taken from close to the bore of a compressor disc. In this region the hoop stresses experienced in service have a maximum influence on the fatigue life of the disc.

* To prepare thin foils both parallel to the surface and perpendicular to the surface so that the damage may be assessed as a function of depth.

* To establish the types of dislocations produced, slip systems which are operative and their relative importance in the primary-α and transformed-β phases.

* To examine the dislocation mechanisms in IMI 834 which lead to crack initiation under cyclic fatigue loading.

* To propose a model of fatigue damage accumulation in IMI 834.

CHAPTER TWO

LITERATURE REVIEW

2.1 INTRODUCTION

The first section of the literature review (section 2.2) is designed to introduce titanium, the recognised classes of titanium alloys and the factors which affect the properties of the classes used in high temperature aerospace applications. The effects of aluminium and silicon additions on the formation of precipitates in the newer, more microstructurally complex alloys, and the formation of an interface phase in titanium alloys are reviewed in detail.

Microstructural modifications of titanium alloys cause alterations in their mechanical properties. The creep, ductility, ultimate tensile strength and fracture toughness of alloys are reviewed with respect to their aerospace applications in section 2.3.

Since the preferred slip systems which occur during the deformation of titanium alloys are influenced by a number of factors which can ultimately affect the alloy's fatigue crack initiation behaviour, the crystallography and deformation modes of titanium alloys are discussed in section 2.4.

Fatigue behaviour is reviewed in section 2.5. An understanding of long crack growth, short crack growth and crack initiation behaviour is outlined. The mechanism of fatigue crack initiation behaviour in lightly alloyed metals, such as copper, is also reviewed.

The damage accumulation mechanisms and sites of room temperature low cycle fatigue crack initiation in titanium alloys are reviewed in section 2.5.6. These are discussed

further in the discussion, chapter 7. The incorporation of a dwell period at maximum load into the fatigue cycle has received much attention over the past 20 years. Although no dwell tests were carried out in the present investigation, a review of the effects is presented in the light of current titanium alloy research (section 2.5.7).

2.2 GENERAL BACKGROUND TO TITANIUM ALLOYS

2.2.1 Introduction

Titanium, the ninth most abundant element in the Earth's crust, was discovered in 1790 but it was not until 1936, with the invention of the Kroll process, that industrial scale production of titanium was possible. The high strength to weight ratio of titanium alloys is achieved because the pure metal has a density of 4500 kg/m^3, which is midway between that of steel and aluminium and is about half that of nickel. The extremely high corrosion resistance of titanium can be attributed to the formation of a passive oxide layer on exposed surfaces. The oxide layer is stable up to 600°C [4], at temperatures above this, the layer dissolves into the parent metal [3]. Both the thermal expansivity and conductivity of the pure metal are low and titanium and its alloys are all non-magnetic. All these properties make titanium an attractive engineering material, a drawback being the cost of production of its alloys; about ten times that of aluminium and roughly one hundred times that of manufacturing steel.

There are two allotropes of pure titanium: The alpha (α) phase, which is hexagonal close packed (hcp) in structure with a $\underline{c}/\underline{a}$ ratio of 1.588 at room temperature, and the beta (β) phase which is stable at higher temperatures and has body centred cubic (bcc) crystal packing. The transition between the two phases occurs at the β transus temperature which, in pure titanium, is 883°C. The β-transus temperature is modified by alloying additions

which also open up a two phase field on the phase diagram (Figure 2.1). Alloying additions which raise the β-transus are known as α-stabilisers, the most important being aluminium and the interstitial elements; carbon, oxygen and nitrogen. β-stabilisers are more numerous and tend to lower the β-transus temperature. Of these elements there are two groups; those which are β-isomorphous elements and those which are β-eutectoid elements. β-isomorphous elements, such as molybdenum, vanadium and niobium, have a limited solubility in the α phase but are mutually soluble in the β phase, and act to stabilise this phase. β-eutectoid elements have a limited solubility in the β phase and promote eutectoid decomposition to give intermetallic compounds. The decomposition of β by the majority of these elements is kinetically unfavourable [12] and, therefore, it is only the more 'active' elements such as copper and silicon that promote precipitation. The remainder of β-eutectoid elements such as iron, chromium and manganese can be considered to be similar to the β-isomorphous elements since they also promote stabilisation of the β phase. A third group of elements act as solid solution strengtheners and do not significantly alter the transition temperature. Tin and zirconium are the two most important solid solution strengtheners.

2.2.2 Effect of Alloy Additions

Table 2.1 lists the compositions of some of the more important titanium alloys that have been developed over the past 40 years for use in higher temperature aerospace applications. The alloys are listed in chronological order and the β-transus temperature and maximum temperature capability are also indicated.

Aluminium, the primary α-stabiliser in virtually all titanium alloys, increases their tensile and creep strengths and reduces their density. One estimate [13] suggests that there is an increase in strength of

approximately 55 MPa for every 1% aluminium present in the alloy. However, as the α-stabilising content is increased, embrittlement can ultimately occur during prolonged exposure at temperature due to the formation of the deleterious, coherent phase α_2 (Ti_3Al). The effects of this phase on the mechanical properties of titanium alloys are discussed further in section 2.2.5.1.

Both tin and zirconium act as solid solution strengtheners in titanium alloys. Tin, also a weak α-stabiliser, is often used in conjunction with aluminium to achieve higher strengths without causing embrittlement of the alloy [4]. In alloys such as IMI 829 and IMI 834 which are designed for use at very high temperatures, increased temperature capability over IMI 685 is obtained by the replacement of zirconium with tin, a denser but more potent solid solution strengthener [14]. Zirconium is also a mild β-stabilising element and increases fatigue strength at low and intermediate temperatures. In concentrations above 5-6 wt% [4] the use of zirconium is detrimental in that it can reduce the ductility and creep strength of the alloy.

The primary β-stabiliser of titanium alloys is the β-isomorphous element, vanadium, the advantages being its low cost and low density [15]. In order to increase the creep resistance of the high temperature titanium alloys, the β-stabiliser content must be reduced (section 2.3.1) and therefore the use of vanadium in high temperature titanium alloys is limited (see Table 2.1B). Molybdenum is the primary β-stabiliser of the high temperature titanium alloys. It is added to promote increased strength and increased hardenability at elevated temperatures [4]. A drawback of the addition of molybdenum to an alloy is that it decreases its weldability [16]; a property which is critical in aero engine applications since, unlike bolt joining, welding reduces the overall component weight. A small percentage of niobium, also a β-stabiliser, is added to improve the

high temperature oxidation resistance [4] of the most advanced titanium alloys, IMI 829 and IMI 834.

The presence of the silicon, a β-stabiliser, is important in titanium alloys since in solid solution it increases the creep strength at all temperatures and has a marked beneficial effect on creep resistance [4, 14, 17]. The maximum effective concentration of silicon in high temperature alloys is governed by its tendency to form silicides, which are discussed further in section 2.2.5.2.

2.2.3 Classes of Titanium Alloys

The two allotropes of titanium (α and β) form the basis of titanium alloy classification. These classes are recognised in the literature by the nature of the predominant phase present in the microstructure at room temperature [6, 12-14]. There are five main classes: (i) Commercially pure or alpha (α). (ii) Near-alpha (near-α) or superalpha. (iii) Alpha + beta (α+β). (iv) Near-beta (near-β). (v) Beta (β) or metastable beta. The distinction between the last two classes is not well defined.

Commercially pure titanium grades are solid solution strengthened to a range of proof strength levels (130 to 480 MPa) by the inclusion of 0.07 to 0.3 at% oxygen [3, 13]. This range gives ultimate tensile strengths (UTS) of between 300 and 750 MPa [3]. These alloys are useful in low temperature applications such as airframes, casings, ductings, firewalls and exhaust shrouds [14]. High temperature exposure results in oxygen dissolution into the metal, forming a hardened, oxygen stabilised layer or alpha-case which reduces the fatigue and fracture properties of the alloy [14, 18].

β alloys are rich in β-stabilising elements and are low in α-stabilisers, and consist entirely of metastable β phase at room temperature. The advantages of β alloys are that

they have high tensile strength, excellent forgeability and good cold formability, in contrast to the α alloys [15]. However, β alloys do not possess useful high temperature properties because of their high density, low creep strength, poor oxidation resistance and low tensile ductility when compared to the α alloys. Their use in airframes is limited due to the problems caused by the segregation of β-stabilisers and the formation of intermetallic compounds (*e.g.* $TiCr_2$ and omega phase) which can embrittle the alloy [5, 19].

Of the increasingly wide range of titanium alloys now available, only the near-α and α+β alloys have been used to a significant extent in the present generation of gas turbine engines.

2.2.3.1 α+β Titanium Alloys

The α+β system contains alloys with one or more of the α-stabilising elements plus one or more of the β-stabilising elements. Examples of important α+β alloys, their composition, β-transus temperature and year of introduction are given in Table 2.1. The most widely used titanium alloy is IMI 318 or Ti-6Al-4V which was introduced in 1954. Its introduction on the JT3D engine (Boeing 747) in 1960 brought about a reduction in weight of up to 18 % when it replaced steel as the disc material [20]. IMI 318 is only creep resistant up to the relatively low temperature of 325°C, however, it still accounts for nearly 50% of the market of titanium alloys. It is used as the main component of the lower temperature compressor sections of gas turbines [13] and in less critical, non-rotating components such as compressor casings [4]. Because of the importance of IMI 318 in aero engines, numerous investigations have been published covering a wide range of its mechanical and microstructure-related properties which have formed the basis for many further studies of other titanium alloys

[21-27].

The α+β alloys have good room temperature properties but their creep resistance is limited to around 400°C by the significant amount of β phase present [6] (discussed further in section 2.3.1). The creep resistant alloys developed for service at temperatures exceeding 450°C are of the near-α type and are discussed in the following section.

2.2.3.2 Near-α Alloys

The drive for higher efficiencies and reduced weight in gas turbine engines has led to the development of a number of advanced near-α titanium alloys which have improved temperature capability over α+β alloys. Table 2.1 and Figure 2.2 list some of the near-α alloys, their composition, β-transus temperature and year of introduction.

Three basic properties required by these high temperature titanium alloys for use in gas turbine engines [9, 17] include: (i) High tensile and yield strengths from room to maximum temperature. (ii) A high fatigue strength at both low and high frequencies from room to maximum temperature in the region of maximum stress. (iii) A high creep resistance at high temperature and high stress. In addition a good thermal stability, a low level of internal stress, good weldability and good oxidation resistance are required [9, 17].

Three very thorough reports by Eylon *et al*. [4], Goosey [6] and Driver [14] review the high temperature titanium alloys, paying considerable attention to the advances in composition, heat treatments, oxidation resistance and microstructure, which have brought about beneficial changes in their performance over the last 40 years (see Figure 2.2). It is well documented [4, 6, 9, 14, 17] that to fully optimise the mechanical properties of these

alloys, their composition and thermomechanical processing (discussed in section 2.2.4) must be carefully adjusted to control the microstructure. Improved properties are obtained by increasing the strength and the amount of the more creep resistant α phase at the expense of the β phase, whilst still maintaining the low temperature strength and forgeability of the near-α alloys.

Creep performance first reached a temperature of 450°C with the introduction in 1959 of the near-α alloy, IMI 679. The development in 1968 of IMI 685 pushed the operating temperature for titanium alloys to above 500°C. IMI 829 (American notation Ti-5331S), a derivative of IMI 685, was introduced in 1977 with a composition which was designed to further improve creep performance. IMI 829 is being extensively used in the Rolls-Royce RB211-535E4 engine [4, 6] up to a maximum operating temperature of 550°C; the highest temperature at which any titanium alloy is currently reputed to be in commercial use. The replacement of nickel and steel with IMI 829 in various components of the compressor discs, the rear cone and turbine blades of the aero engine gives a total weight saving of over 50 Kg [4].

Two higher temperature near-α titanium alloys that utilise conventional alloying techniques have been developed. Ti-1100 is an American based alloy under consideration for use up to a maximum temperature of 593°C (1100°F) [8, 28, 29]. IMI 834 has been developed by 'The Total Engineering Approach' employed by Rolls-Royce [30] and is being designed for potential use at temperatures up to 600°C [6, 9], with short excursions up to 650°C [10]. If IMI 834 is used for the high pressure compressor of the Trent engine, it would save 85 Kg (or 42%) of the total drum weight compared with the existing RB211-524 design [10]. The development of IMI 834 is discussed further in section 2.3.1.

2.2.4 Heat Treatment and Microstructure

The heat treatments and resulting microstructures of α+β and near-α alloys are fundamental in determining their mechanical properties. The processing routes can be complex and need to take into account a variety of different factors which can ultimately affect the alloys performance. The following sections are designed to give an overview of different heat treatments which can be applied to α+β and near-α titanium alloys. The effects on the mechanical properties are discussed later in section 2.3.

2.2.4.1 Solution Treatment

Both near-α and α+β alloys first pass through the β-transus on cooling from the operating temperature of the vacuum arc melter, during which the α phase precipitates within the prior-β grains in the form of acicular α-platelets, as illustrated in Figure 2.3. In general, most near-α alloys tend to be re-heated to above the β-transus temperature during subsequent billet reduction, forging and solution treatment. Such alloys are termed β-processed or β-heat-treated near α-alloys. The final transformed-β microstructure consists entirely of α-platelets, the arrangement of which depends upon the last through-transus cooling rate (discussed in section 2.2.4.2).

Most α+β alloys and some near-α alloys (such as IMI 679 and IMI 834, see section 2.3.1) are solution treated, below their respective β-transus temperatures, in the α+β phase field and are thus termed as having been α+β processed. During the α+β processing some, but not all, of the α phase present at room temperature will redissolve to form β phase. On subsequent cooling, the α phase, which did not dissolve at the α+β solution treatment temperature, precipitates as equiaxed primary-α grains on the boundaries of the β phase. On cooling, the

remaining β phase transforms to form arrangements of α-platelets in the prior-β grains, as in the case for β-processed microstructures. The primary-α has the effect of pinning the β-boundaries and consequently restricts the β-grain size resulting in a duplex microstructure consisting of equiaxed primary-α grains in a matrix of fine, transformed-β grains. The proportion of primary-α depends upon the exact temperature of the heat treatment, as illustrated in Figure 2.4 for the alloys Ti-6Al-4V, IMI 829 and IMI 834 [31]. Ti-6Al-4V and IMI 834 both have a shallower β-transus approach curve than IMI 829 *i.e.*, for each unit increase in temperature below the β-transus there is a smaller increase in the volume fraction of β phase present for Ti-6Al-4V and IMI 834 compared to IMI 829. A shallower curve results in there being a wider temperature range in which a uniform microstructure can be achieved during α+β processing at temperatures just below the β-transus. In the case of IMI 834, the addition of a small quantity of carbon has the effect of 'flattening' the β-transus approach curve and therefore permits accurate, high α+β processing [8, 9, 31-33].

2.2.4.2 Effect of Cooling Rate

The morphology of the transformed-β grains at room temperature varies according to the cooling rate (see Figure 2.5) which significantly affects the resulting mechanical properties of titanium alloys. The following summary outlines the effect of cooling rate on both α+β and β-processed alloys. The resulting microstructure produced ultimately depends upon the cross-section of the component involved *i.e.* thick sections require a faster cooling rate than thinner ones to obtain an equivalent microstructure.

Furnace cooling at rates between 0.1 and 1°C/s gives well defined colonies of similarly orientated α-platelets with a relatively thick layer of grain boundary α at the

prior-β grain boundaries (see Figure 2.5a). In the transmission electron microscope (T.E.M.), thin films of retained-β are resolvable at the α-platelet boundaries.

Air cooling at rates close to 10°C/s produces aligned colonies of acicular α-platelets with several colonies existing within individual prior-β grains [35]. All the α-platelets within one colony lie parallel to one another along the same set of β planes according to the Burgers orientation relation [36-38]:

$$\{110\}_\beta // (0001)_\alpha : \langle 111\rangle_\beta // \langle 11\bar{2}0\rangle_\alpha \qquad (2.1)$$

and the other variants which must follow [38]:

$$\{1\bar{1}2\}_\beta // \{01\bar{1}0\}_\alpha : \langle 111\rangle_\beta // \langle 11\bar{2}0\rangle_\alpha \qquad (2.2)$$

$$\{01\bar{1}\}_\beta // \{01\bar{1}1\}_\alpha : \langle 111\rangle_\beta // \langle 11\bar{2}0\rangle_\alpha \qquad (2.3)$$

Adjacent colonies may contain α-platelets with different variants of this relation. Prior-β grain boundaries can be identified by a layer of grain boundary α as illustrated in Figure 2.5b. As with furnace cooled microstructures, thin films of retained-β at the α-platelet boundaries are resolvable by T.E.M.

Oil quenching at approximately 100°C/s results in Widmanstätten or basketweave arrangements of acicular α-platelets within the prior-β grains, the boundaries of which are outlined by a thin layer of grain boundary α (Figure 2.5c). Each individual α-platelet in this basketweave arrangement nucleates independently, usually from a grain boundary and is crystallographically related to the parent β phase by the Burgers orientation relation (equations 2.1 to 2.3) [36-38]. A thin, discontinuous layer of retained-β is present at the α-platelet boundaries and is resolvable by T.E.M.

Water quenching at a rate of between 350°C/s and 2000°C/s

generally results in the β-phase transforming to a very fine microstructure of martensite (α′) needles which are outlined by the prior-β grain boundaries (Figure 2.5d). Little or no retained-β phase may be detected by T.E.M. at the boundaries of individual martensite needles [13].

The transformed-β colony size is an important microstructural parameter which is related to both the prior-β grain size and the cooling rate [35]. Table 2.2 gives the effect of cooling rate on the grain and colony size of Ti-6242-Si [39]. Slow cooling rates promote larger colonies, particularly after limited working in the β phase field [40]. Large colonies are also favoured by low β-stabiliser content, high solution treatment temperatures [41, 42] or longer times spent at elevated temperature [43]. For IMI 685 the mean intercept diameter for colonies varies in size from 10 to 250 μm depending upon the processing conditions [42].

2.2.4.3 Ageing Treatment

After cooling from the solution treatment temperature, most α+β and near-α alloys are given a final annealing or ageing treatment. Ageing treatments are carried out well below the β-transus and are designed to relieve internal stresses (particularly in components of large cross section) and to develop microstructures which show improved properties, such as creep strength, compared to the as-formed microstructures [12].

The effect of ageing IMI 834 (α+β processed, oil quenched) for four hours at 600, 650 and 700°C has been investigated [32]. Spheroidisation of the small amount of retained-β phase present at the α-platelet boundaries occurs at the lowest ageing temperature. Ageing at progressively higher temperatures results in an increase in the amount of spheroidised-β. There is also a consequent decrease in the dislocation density associated with the α-platelet boundaries, due to the reduced

requirement of α and β lattice mismatch. An increase in tensile and creep properties and a decrease in ductility and crack propagation resistance is also observed [32]. In addition to the above, the formation and coarsening of silicides occurs. Silicide precipitation in titanium alloys has been the subject of a large number of investigations and is discussed further in section 2.2.5.2.

2.2.5 Precipitates Associated with Solutes

2.2.5.1 Ordered Phase, α_2

The degree of solid solution strengthening in titanium alloys is somewhat unfortunately limited by the occurrence of α_2, an ordered coherent phase based on $Ti_3(Al,Sn)$ ($\underline{c}_{\alpha 2} = \underline{c}_{\alpha}$; $\underline{a}_{\alpha 2} = 2\underline{a}_{\alpha}$ [12]). Additions of more than 5-10 wt% Al leads to the precipitation of this phase with consequent reductions in fracture toughness and ductility (section 2.3.2). Having studied the creep and tensile properties of various titanium systems, Rosenberg [44] established an empirical relationship for the aluminium equivalent, Al* (wt%):

$$Al^* = Al + Sn/3 + Zr/6 + 10(O + C + 2N) \quad (2.4)$$

In order to avoid excessive α_2 formation the aluminium equivalent should be maintained below 9 wt%. Above an Al* of approximately 5 wt%, α_2 occurs as coherent ellipsoidal fully ordered particles [12] separated by disordered regions, the size and volume fraction of which increase with Al* and ageing temperature. For example, the ageing of IMI 834 (Al* = 9.17 wt% [45]) for four hours at 700°C results in ordered precipitates of α_2 in the primary-α which are 2.5 nm in diameter and 10 nm apart [32]. The increased level of ordering within primary-α is considered to be related to the higher Al* present in these areas compared to the α-platelets in the transformed-β structure.

2.2.5.2 Silicide Precipitation

It is well established that the addition of up to 0.5 wt% silicon improves the creep resistance of high temperature titanium alloys [37, 39, 46-52]. As an example, Figure 2.6 shows the effect of silicon on the creep strain in Ti-6242-Si aged at 510°C for 100 hours at 240 MPa [53]. A minimum in the total plastic strain suggests that the best creep performance is obtained in this alloy with the addition of 0.1 wt% silicon. The mechanism by which silicon improves the creep resistance is not clear, although it has been suggested that the interaction of silicon with dislocations impedes their motion by atmosphere drag and dynamic strain ageing [54, 55]. In comparison with other alloy systems, it is possible that a low concentration of silicon decreases the stacking fault energy of alloys and consequently reduces the mobility of dislocations by restricting cross-slip [4].

As a result of the improvements in creep performance observed with silicon additions, new commercial alloys have been designed to contain up to 0.5 wt% silicon [53]. It is interesting to note that differences in design philosophy are reflected in the nominal silicon concentration [51]; in America alloys have been developed which contain $\leq$ 0.1 wt% Si whereas the British alloys (IMI designations) contain 0.25 wt% < Si < 0.5 wt% [51] (see Table 2.1).

Additions of silicon result in the precipitation of a silicon rich phase known as silicide. The silicide phase occurs either (i) on ageing a silicon containing titanium alloy which has been quenched from its processing temperature or (ii) on cooling at slow rates (< 250°C/hr [51]) from the processing temperature.

It was originally thought that silicides have a composition intermediate between Zr_5Si_3 and Ti_5Si_3, *e.g.* $(TiZr)_5Si_3$ [46]. Since then, there have been numerous

investigations into the occurrence and characterisation of titanium-zirconium silicides in Ti-2%Si [56], IMI 679 [51], IMI 685 [47, 50, 52, 57] and IMI 829 [51, 58-60]. Two different types of silicides (S_1 and S_2) with hexagonal structure were reported [61]; S_1 = $(TiZr)_5Si_3$ ($\underline{a}$ = 0.780 nm, $\underline{c}$ = 0.544 nm) and S_2 = $(TiZr)_6Si_3$ ($\underline{a}$ = 0.70 nm, $\underline{c}$ = 0.36 nm), although there were variations in the lattice parameters depending upon the alloy and the investigation [47, 50]. It was later proposed that the two silicides are distinct but that S_1 transforms to S_2 on extended ageing and that the composition can be expressed as $(TiZr)_5(SiSn)_3$ [57]. The tin content of this silicide is believed to increase with an increasing amount of tin in the parent alloy, whilst the Ti:Zr ratio decreases with ageing time due to the slower diffusion of Zr in the titanium matrix. It was suggested that the transformation from S_1 to S_2 may be caused by a change in the interstitial content (O or N) of the silicides on ageing [57]. It was proposed that the transformation initiates with a decrease (around 10%) in the $\underline{a}$ axis of the S_1 silicide followed by a collapse of the $\underline{c}$ axis which results in the formation of the S_2 type silicide [57]. There has been some disagreement in the literature on the space group of silicides in IMI 829. Banerjee *et al*. [51, 60, 62] propose that the space group was P6/mmm whereas Woodfield and Loretto [58] suggest P62m as the space group of the silicide.

Sridhar and Sarma [63] show that the size of silicides obtained on ageing IMI 829 at 625°C for 24 hours is dependent upon the cooling rate from the β-processing temperature; furnace cooling and subsequent ageing results in silicides of 0.2 to 0.8 μm in length with an aspect ratio of 1:3 to 1:4 whereas water quenching followed by ageing produces silicides of 0.05 to 0.1 μm in length and aspect ratio 1:1.5. The size of silicides also varies according to the ageing temperature and silicon content [59]. The sites of precipitation and consequent growth rates of the silicides depend strongly upon the solution

treatment temperature and quenching rate [51, 58]. For example, in IMI 829 processed at 1020°C for 1/2 hour and aged at 700°C for 10 hours [51], silicides precipitate along α/β interfaces and on α-platelet boundaries in air cooled specimens, whereas in the oil quenched specimens the silicides precipitate on the c-component dislocations within the α-platelets and at α-platelet boundaries [64] (section 2.2.4.2).

As the properties of silicon containing high temperature titanium alloys become more critical, studies to determine their response to room temperature tests are increasingly necessary. Alloys quenched from above the β-transus temperature (IMI 685 and IMI 829) show a slight increase in their tensile and yield strengths on ageing but, more significantly, show a severe loss of ductility [52, 63-68]. The cause of this loss was investigated [63, 64, 66-68] and is discussed in section 2.3.2.

2.2.6 The Interface Phase (IFP)

The detection of an interface phase (IFP) at the boundaries between α and β phases of various titanium alloys has, over the last two decades, been the subject of a wide variety of studies and considerable controversy.

In 1975, Rhodes and Williams [69] showed that the phase could be observed in the T.E.M. at the α-platelet boundaries as a distinct layer, between 0.1 and 0.4 μm wide, in as many as 40 different titanium alloys. The layer was believed to develop as (i) a hexagonal (hcp) striated phase having a different orientation than the primary-α into which it grew or as (ii) a face centred cubic (fcc) monolithic phase with a lattice parameter, a, of approximately 0.42 nm which varied depending upon the alloy composition and the processing conditions [69]. Both phases were also commonly observed together [70-72] with the monolithic phase lying closer to the retained-β phase than the striated phase [70].

The origins of these phases were clearly of importance as the α/β interface was believed to influence the fracture behaviour of titanium alloys, especially during fatigue and stress corrosion studies. The interface was thought to provide an easy crack path and was believed to be detrimental to the fatigue and corrosion lives of titanium alloys [41, 73].

During early studies, Rhodes and Paton [70] suggested that the monolithic fcc phase was an intermediate transition phase formed during the β to α transformation. A mechanism was proposed whereby sluggish β-stabiliser diffusion away from the interface region transformed the β phase to the monolithic fcc structure ($\underline{a}$ = 0.426 nm) which was then modified by the formation of (111) twins to the striated IFP layer [70]. The striated layer was then believed to transform to the α phase.

During the same period as the studies performed by Rhodes and Paton [70], a number of workers investigated the effect of the deliberate introduction of various concentrations of hydrogen into titanium alloys [74-77]. In a T.E.M. study of Ti-5Al-2.5Sn, Hall [75] analysed foils from specimens containing 50 to 1600 ppm hydrogen. The addition of 330 ppm hydrogen caused one grain in every ten to exhibit platelets which were 0.1 μm thick and often extended across α-platelets. The platelets had a fcc structure and were referred to as γ-hydrides. From the orientation relationships and lattice parameter measurements, the fcc γ-hydrides were crystallographically identical to the monolithic fcc phase observed by Rhodes and Paton [70]. As the hydrogen content was increased, the number of grains containing the fcc γ-hydrides increased and two further precipitates were observed to form. A near-basal hydride was precipitated at > 510 ppm hydrogen and at > 600 ppm, so-called hydrogen stabilised stacking faults were also precipitated [75]. The effects of deliberate hydrogen additions on Ti-6Al-4V with

different material processing treatments was also investigated by Hall [76]. Similar phases were found to form at certain α/β interfaces and across α-platelets. However, the concentration of hydrogen at which the fcc γ-hydride was first detected in the T.E.M. varied according to the microstructure. Hence, fcc γ-hydride formation was found to depend strongly upon both microstructure and hydrogen content.

Subsequently, numerous investigators [71, 72, 75, 76, 78-80] found the crystallography of the Rhodes-Paton model [70] inapplicable to their alloys. An alternative origin for this phase was proposed, using electron diffraction studies and lattice parameter measurements, based on the similarities with the binary hydride of titanium, TiH_2 (section 2.2.6.1).

2.2.6.1 The Monolithic fcc Phase

On the assumption that the interface phases observed were hydrides of titanium, the possible mechanisms of their formation were investigated. Monolithic fcc phase formation was thought to form as a hydrogen phase or hydrogen induced phase stabilised by stress, strain or compositional gradients [71, 72, 79] and was visualised to occur as follows [79]: As the β-α transformation proceeded on cooling the alloys through the β-transus, partitioning of various alloying elements occurred. The partitioning of hydrogen was particularly effective below 573 K at which point the solubility of hydrogen in α-titanium decreased rapidly. Hydrogen atoms migrating from the α phase to the interface precipitated in this region since the supersaturation exceeded the solubility limit of hydrogen. Precipitation took place when the β-α transformation was complete.

Electron diffraction studies have suggested different orientation relationships and lattice parameters for the monolithic fcc IFP. These are summarised in Table 2.3.

The lattice parameter, a, varies with alloy composition and has been reported to lie between 0.420 nm [78] and 0.453 nm [85]. The orientation relationship most frequently reported for the monolithic fcc phase [72, 75, 77, 84, 85] is:

$$(001)_{fcc}//(0001)_{\alpha}//(110)_{\beta}; \quad (2.5)$$
$$<110>_{fcc}//<11\bar{2}0>_{\alpha}//<111>_{\beta}$$

2.2.6.2 The Striated Phase

Identification of the striated form of the interface phase has led to much confusion in the literature [69-71, 78, 84, 85, 87]. This phase was originally designated as Type 2α and has been identified as either hcp [26, 69, 71, 81, 87] or fcc [70, 72, 78-80, 84, 88]. The hexagonal morphology of the striated interface phase was thought either (i) to form by mechanical twinning due to a stress induced reaction on $\{10\bar{1}2\}$ and $\{10\bar{1}1\}$ planes [87] or (ii) to be a more stable form of the α phase whose formation could possibly be caused by compositional differences [69].

Hammond and co-workers [72, 78, 84] consistently observed the striated (Type 2α) phase as thin lamellar particles both within and at the boundaries of the α-platelets. The structure of this phase was analysed as fcc or face centred tetragonal (fct) [72, 78, 84]. The particles were frequently internally striated and these striations were identified as the traces of $\{111\}_{fcc}$ twins. The occurrence of both the monolithic and striated phases was said to depend upon the cooling rate [72]; air cooling IMI 685 (at approximately 400°C/min) gave the monolithic phase (a = 0.435 nm), whereas slow cooling (at less than 5°C/min) produced the striated phase which was crystallographically identical to the monolithic fcc interface phase [78, 84]. Both forms occurred at intermediate cooling rates and it was observed that the striated phase precipitated within

the α-platelets and along the α/β interfaces whereas the monolithic phase was only found at the α/β interfaces. At higher ageing temperatures, the striated phase was determined to have a face centred tetragonal (fct) structure with a $\underline{c}/\underline{a}$ ratio of 0.9 [78].

2.2.6.3 Effect of Foil Preparation

It later appeared that the formation of the IFP was dependent on the thin foil preparation technique employed. For example, Shelton and Ralph [88] prepared foils from Ti-6Al-4V by electropolishing and observed three interface morphologies; a monolithic fcc phase, a striated fcc phase and a dislocated structure identified as hcp which was slightly misorientated with respect to the α phase. In foils prepared from ion-beam milling, no IFP regions were observed [88]. Banerjee and Williams [81] carried out similar experiments with foils of two starting thicknesses (0.05 and 0.1 mm) to observe the effect of foil thickness on interface phase formation. The results obtained suggested that both the fcc and hcp interface phases found in titanium alloys arose from processes which occurred during the electropolishing of thin foils. The fcc phase was formed in alloys with low β phase fractions and larger starting thicknesses and consequently the fcc phase was determined to be a hydride of titanium arising as a result of an increase in hydrogen concentration during electropolishing. The hexagonal interface was observed at smaller starting thicknesses in a $<10\bar{1}2>\{10\bar{1}1\}$ twin relationship to the α phase [81, 83] and was suggested to form as a result of stresses at the α/β interface arising from thin foil relaxation in the β phase during electrolytic thinning. Ion-beam milling suppressed β phase relaxation [89] and prevented the formation of the hcp phase as well as the occurrence of the fcc phase [81, 83].

Isaac and Hammond [84] agreed with the suggestion by Banerjee and Williams [81] that the interface phase was a

thin foil artefact but continued to observe the striated phase in their alloys as having an fcc or fct structure ($\underline{a}$ = 0.425 nm). X-ray diffraction revealed no reflections attributable to an fcc phase in the bulk material and it was proposed [84] that the phase only occurred due to the relaxation of surface constraints during the electropolishing of thin foils.

Having established that the IFP arose as a thin foil artefact [81, 89], a detailed study of diffraction patterns obtained from Ti-10V-2Fe-3Al was carried out by Banerjee *et al*. [85] in order to provide a consistent view-point for IFP formation. The hcp phase was found to exist in six variants formed by twinning on the six possible $\{10\bar{1}1\}$ planes of the parent Burgers α-platelet. The crystallography of this phase strongly suggested that it was a stress induced product formed by the volume expansion of the β phase caused by hydrogen absorption during electropolishing. Expansion of the β phase placed the α phase in compression which then deformed by twinning or slip. When the α-platelet size was small in relation to the surrounding β phase (*e.g.* in high temperature alloys), twinning was suggested to be the favoured deformation mechanism. According to Banerjee *et al*. [85], characteristics of the hcp phase were arced reflections in the diffraction pattern. Characterisation of the fcc IFP confirmed the existence of both the monolithic and striated morphologies, which were assigned different orientation relationships as given in Table 2.3. Both forms were determined to be hydrides of titanium that had nucleated on the α side of the α/β interface (i) in alloys with low volume fractions of β phase, or (ii) when the electropolishing times were high (*i.e.* when the hydrogen content was expected to be high). When the striated and monolithic morphologies were observed to exist together, the monolithic form lay adjacent to the α/β interface with the striated form within the α phase, in agreement with earlier work [70, 78]. The IFP was not observed in thin foils prepared by a method which

minimised increases in hydrogen concentration, such as grinding in CCl_4 followed by ion-beam milling. Despite much effort by Banerjee *et al.*, the exact mechanism of the formation of the fcc phase is still unknown.

Careful diffraction analysis by Banerjee *et al.* [85] was said to quite clearly reveal the structural differences between the strongly resembling striated fcc IFP and the hcp IFP which had caused so much confusion in earlier work. In contrast, Servant *et al.* [86] recently observed that the fcc IFP formed regardless of the thinning conditions, but only in foils from alloys which had received specific thermal treatments. Continuous cooling transformation curves constructed by Servant *et al.* showed that the width of the IFP was a function of the cooling rate from the β-processing temperature. This was in agreement with Rhodes and Paton [70]. The compositions of the α, β and interface phases were presented as a function of the cooling rate [86]. They showed an increase in the β-stabiliser content with (i) a decreasing cooling rate and (ii) on moving from the α phase, to the striated fcc phase, to the monolithic fcc, to the β phase [86]. Despite all the research carried out previously on the characterisation of the interface phases, Servant *et al.* [86] believed that the interface phases they had found, which were enriched in β-stabilisers, must be distinguished from the titanium hydride that formed after specific preparation techniques.

In current commercial alloys the hydrogen concentrations are low enough, typically 30 - 70 ppm [73, 90], that these phases are only observed as thin foil artefacts and, as such, are unlikely to affect the behaviour of the bulk material [85].

2.3 MECHANICAL PROPERTIES

2.3.1 Creep Resistance

The creep performance of high temperature titanium alloys is assessed by determining the maximum temperature at which alloys satisfy the creep test requirements, namely the temperature up to which the alloy undergoes less than 0.1% total creep strain in 100 hours at a stress of 310 MPa [6]. Generally, good creep resistance is obtained from an alloy which contains a small amount of the retained-β phase as this increases the resistance to diffusion controlled (vacancy) creep because the diffusion rate of elements can be up to one hundred times faster in the β-phase than in the α-phase [91].

Major advances in the development of creep resistant titanium alloys came in the late 1950's when it was recognised that to obtain maximum creep resistance it was necessary to have an α titanium base strengthened by solute elements [5]. The relatively highly stabilised β phase of established α+β alloys such as IMI 550 and Ti-6Al-4V did not have the required creep stability and a new family of titanium alloys, the near-α alloys (section 2.2.3.2), was investigated. In these alloys the amount of α-stabilisers used was sufficient to avoid the embrittlement of the alloy through α_2 phase formation (section 2.2.5.1). The small fraction of β-stabilising elements present in these alloys allowed reasonable strength levels to be achieved. The first major near-α alloy to be developed in the U.K., IMI 679 (Table 2.1), was α+β processed and was creep resistant to 450°C.

In the mid 1960's it was discovered that significant improvements in creep resistance could be achieved by β-processing the near-α compositions. The ductility of IMI 679 was markedly reduced by β-processing. However, the β-processed alloy, IMI 685, was developed from IMI 679 by varying the composition so that the creep resistance could

be maintained at acceptable levels of tensile strength and ductility. IMI 685 represented a major breakthrough in design philosophy because, as well as being creep resistant up to 520°C, IMI 685 was also weldable giving significant weight savings in the new high pressure compressor discs.

A comparison of the differences in properties resulting from β-processing and α+β processing is given in Table 2.4. A β-processed, acicular-α microstructure was desirable for an improved fracture toughness (section 2.3.4) and fatigue crack growth resistance (section 2.5.6) as well as an improved creep resistance. However, β-processed structures had a much larger microstructural unit size compared to α+β processed structures and this resulted in an inferior fatigue crack initiation resistance (Table 2.4 and Section 2.5.6). High temperature alloy disc designs were consequently becoming fatigue limited in the bore region rather than creep limited at the rim. The development of new alloys had to reflect the need to maximise the all-round capabilities and not just the creep and tensile properties of the alloys in the components [5]. The fatigue resistance of the alloys had to be a priority if alloys were to be developed for use at even higher temperatures and stresses.

IMI 829 was developed with aluminium, tin and zirconium contents which were chosen to maximise the creep performance. The forging routes developed were aimed at minimising the β-grain size by β-recrystallisation [92]. This technique involved working the material by a minimum amount in the α+β phase field to induce sufficient pre-strain for β-recrystallisation, and consequent grain refinement, to occur on reheating to the β-phase field [9]. Unfortunately it was difficult to produce grain diameters of less than one millimetre in alloys such as IMI 685 and IMI 829 for use in turbine engines [4, 31, 32] but it was claimed by Neal in a more recent paper [9],

that grain sizes of approximately half a millimetre were achieved in IMI 829 using the technique described above.

Even with the refinement of β-grain size achieved in IMI 829, the fatigue performance of β-processed, near-α alloys could not match that of α+β alloys with equivalent tensile strengths [9]. The grain size of near-α alloys needed to be reduced still further to achieve significant improvements in the fatigue performance whilst still maintaining the creep properties [9, 31]. A reduced grain size could be obtained by α+β processing to produce an equiaxed structure, however, this method could not be employed on IMI 829 because of the restricted α+β phase field or 'heat treatment window' (illustrated in Figure 2.4, section 2.2.4.1). Accurate heat treatment within a small temperature range was not practically possible with large aero engine components. As already described in section 2.2.4.1, the addition of a small quantity of carbon (0.06 wt%) to the alloy IMI 834 had the effect of decreasing the gradient of the β-transus approach curve and permitted accurate α+β processing. Grain sizes of 0.1 to 0.2 mm in diameter were achieved with a small volume fraction (5% to 15%) of primary-α phase. The alloy was creep resistant up to 600°C and combined the advantages of β-processed alloys with those of more fatigue resistant, α+β processed alloys. The improvements in creep capabilities are best illustrated in the form of a Larson-Miller plot; Figure 2.7 shows the improvements in creep resistance achieved (for selected alloys) over the last 40 years.

The creep resistance of titanium alloys has been found to increase with additions of silicon up to 0.5 wt% by a mechanism of dynamic strain ageing [37, 55, 93] (see section 2.2.5.2). It was suggested that the improved creep resistance of recent β-processed near-α alloys is achieved more as a result of the increased amounts of silicon being taken into solution at the higher temperatures employed than by the associated change from

an equiaxed α+β microstructure to an acicular-α morphology [91]. The changes in microstructure and composition of high temperature titanium alloys which were associated with the improvements in creep performance have, however, led to severe losses in ductility being recorded during high temperature exposure [64]. These losses are discussed in section 2.3.2.

2.3.2 Ductility

It is the ductility of an aero engine component, along with the fracture toughness (section 2.3.3), that determines its impact resistance and is particularly important where contact with debris or bird-strike may occur, for example at the anterior of the compressor section of a gas turbine engine. The two parameters used to describe ductility are the reduction in area (RA), measured as the percentage difference of the original and final cross-sectional areas, and the elongation (%E), measured as the percentage difference of the original and final specimen lengths.

As with other mechanical properties, the ductility of titanium alloys is markedly influenced by a change in the processing conditions. A decrease in RA by a factor of about two has been observed in changing from an α+β processed microstructure to processing above the β-transus [94, 95].

Banerjee *et al.* [96] observed the changes in the ductility of a near-α alloy on altering the cooling rate from the solution treatment temperature. Water quenching from the β-processing temperature resulted in a poor ductility compared with material that had been air cooled. The behaviour was related to the relative strengths of the prior-β grain boundaries and the matrix. In martensitic structures resulting from water quenched material, deformation was localised at the grain boundaries due to the restriction on slip into adjacent grains.

The boundaries became a site for void nucleation and, since they provided a continuous path across the specimen, fracture was intergranular, and a low ductility resulted. On decreasing the cooling rate deformation was no longer localised at the grain boundaries and void nucleation sites lay at the Widmanstätten α/β interfaces. Fracture was therefore intragranular and resulted in a higher ductility.

Woodfield *et al.* [64] observed that the ductility of tensile specimens of IMI 829 was reduced after ageing at 575°C for 100 hours. This loss was believed to be associated with the precipitation of silicides. However the mechanisms were found to be more complex and involved an interplay between α_2 ordering and the presence of silicides [64]. The work by Woodfield *et al.* [64] suggested that, in addition to the Al* (section 2.2.5.1), the level of silicon was also important in determining the onset of ordering which could lead to a reduction in ductility. The improvement in creep properties associated with silicon additions may also be lost during high temperature exposure due to the precipitation of silicides.

2.3.3 Ultimate Tensile Strength

The room temperature ultimate tensile strength (UTS) of titanium alloys ranges from approximately 300 MPa in commercially pure grades [3] to 2260 MPa in the case of the β alloy, Ti-13V-11Cr-3Al, in the solution treated condition [11]. The UTS values vary according to a large number of factors including; alloy composition, solute content, the nature of the transformed-β, the relative fractions of primary-α and transformed-β, the grain size and the texture of the material [97]. Strength levels for alloys are therefore quoted for a particular heat treatment or expressed as a range of values. The range of UTS at room temperature for $\alpha+\beta$ alloys is between 900 and 1400 MPa [3, 98], for example IMI 550 has a room

temperature UTS of approximately 1200 MPa in the solution treated and aged condition [3, 98]. The high temperature near-α alloys have typical room temperature UTS values of between 900 and 1250 MPa [99], for example IMI 834 has a UTS range of approximately 1030 to 1050 MPa after solution treatment, oil quenching and ageing at 700°C for two hours [6].

The most important factor affecting the UTS in α+β and near-α alloys is the nature of the transformed-β (Section 2.2.4.2). Material quenched from the solution treatment temperature has a fine microstructure and therefore has an improved strength when aged over material that has been furnace cooled and aged, as illustrated in Table 2.5 for the alloy Ti-6242-Si [99]. The increase in UTS occurs at the expense of the material ductility (section 2.3.2) and it is therefore of importance to obtain the best compromise between these properties in aero engine applications.

The UTS is dependent upon the fraction of primary-α and transformed-β phases present in the alloy which is related to the alloy composition [97]. For example, an increase in the volume fraction of the primary-α phase causes a decrease in the fraction of the β phase. At high temperatures the β phase increases in stability as a result of a promotion of solute partitioning to the β phase. Additions of neutral alloying elements, such as tin and zirconium, increase the strength of alloys without significantly altering the β-transus temperature (section 2.2.2). For every 1% tin added there is an estimated increase in strength of 28 MPa, whereas for every 1% zirconium added, there is an estimated increase of only 3.5 MPa [13]. Although tin is denser than zirconium, its use in high temperature titanium alloys is preferred because of its more potent solid solution strengthening effect. IMI 551, for example has 2% more tin than IMI 550 and is 15% stronger at room temperature, with all other properties remaining essentially unaltered [97]. The

degree of solid solution strengthening is severely limited by the formation of ordered phases such as α_2 (section 2.2.5.1) which can ultimately embrittle the alloy.

The presence of the interstitial elements, carbon, oxygen and nitrogen, increases the UTS of titanium alloys, particularly those of commercially pure grades. The effects of these additions has been extensively reviewed [100] and are also discussed in detail in section 2.4.

2.3.4 Fracture Toughness

The plane strain fracture toughness for metallic materials, K_{1c}, is determined from standard procedures [101]. The experimental conditions for K_{1c} determination are not always satisfied during testing, hence a provisional value of plane strain fracture toughness, K_Q, is normally quoted instead [38, 102].

The fracture toughness of α+β and near-α titanium alloys is very sensitive to the effects of microstructure and texture. For a given alloy, β-processing yields a much greater fracture toughness than does α+β processing (see Table 2.4) [103]. This difference can be attributed to the more tortuous crack paths and greater propensity for multiple slip at the crack tip in the β-processed material [104]. The advantage of β-processing is lost however if the cooling rate is too rapid which leads to the formation of martensite [103].

The relationship between fracture toughness, strength and ductility on three α+β processed titanium alloys (IMI 318, IMI 550 and IMI 551) was investigated [103]. In IMI 318 and IMI 550, the fracture toughness of air cooled and aged alloys increases with the solution treatment temperature whereas the proof stress, tensile strength and ductility remain fairly constant. For water quenched and aged material, there are marked minima in the proof and tensile stress values in all three alloys as the solution

temperature increases. However, the fracture toughness and ductility are not appreciably affected. The fracture toughness was found to be proportional to the volume fraction of Widmanstätten-α, and the strength was found to be proportional to the volume fraction of martensitic-α. The coarser Widmanstätten microstructures were believed to have a greater fracture toughness due to the ability of the thicker α-platelets to arrest or deviate cracks [103]. Using *in situ* tensile stage straining experiments in the T.E.M., it was suggested [41] that the minimum thickness of an α-platelet required to deviate a crack in the material examined was 2 μm (see also section 2.5.6.3).

An increase in the fracture toughness of 100% has been found in air cooled and aged IMI 550 on increasing the solution treatment temperature from 880 to 980°C [41]. This increase corresponded to a change in the volume fraction of primary-α from approximately 70% at 880°C to 10% at 980°C. Thus, higher volume fractions of primary-α led to inferior fracture toughness values and it has been suggested that this is due to an increase in the number of favourable void nucleation sites at the boundaries of equiaxed-α grains [105].

Bowen [106] highlighted the importance of test piece geometry on the fracture toughness of titanium alloy components with observations on strongly textured Ti-6Al-4V. High fracture toughness values were obtained in specimens where a crystallographic slip system was parallel to the plane of maximum shear stress. In specimens where the deformation modes were not aligned with the planes of maximum shear, much lower values of fracture toughness were recorded.

2.4 CRYSTALLOGRAPHY AND DEFORMATION MODES IN TITANIUM

A comprehensive review of the crystallography of hexagonal

close packed (hcp) metals was presented by Partridge [107]. Details on atomic positions in the hcp structure, interstitial positions, the reciprocal lattice, crystallographic indices and stereographic projections for hcp metals are discussed [107]. The review also covers the identification of dislocations and the determination of Burgers vectors, $\underline{b}$, in hcp metals (see Appendix 1) and observations on the slip and twinning behaviour in titanium and magnesium alloys.

The lattice symmetry of hcp metals is usually illustrated by means of a hexagonal prism, Figure 2.8, in which the distances between atom centres are taken as $\underline{a}$ and $\underline{c}$. Table 2.6 lists the $\underline{c}/\underline{a}$ ratios and the variations in the planar spacing and atomic density for prism and basal planes in several hcp metals. No pure metal has the ideal $\underline{c}/\underline{a}$ ratio of 1.633. The intrinsic Peierls-Nabarro stress necessary for slip is expected to be smaller for planes which have the largest interplanar spacings and contain the shortest lattice transition vectors [107, 108]. On the basis of this model, prism slip is expected to replace basal slip as the predominant slip mode when the $\underline{c}/\underline{a}$ ratio becomes less than 1.73, because below this ratio the prism plane spacing is greater than the corresponding values for the basal plane. This concept apparently accounts for the predominance of prism slip in titanium and zirconium, however, the predominance of basal slip in cobalt, magnesium and beryllium cannot be explained [107]. Investigations by various workers have suggested that a thermally activated component also affects the deformation modes in hcp metals [100]. In this section, the factors affecting the deformation modes of titanium are discussed.

The deformation modes of titanium were established by Churchman [109] and other workers [110-112]. From observations on single crystals of commercially pure titanium, it was shown that slip occurred on the basal (0001), prismatic $\{01\bar{1}0\}$ and pyramidal $\{1\bar{1}01\}$ planes with $\langle\underline{a}\rangle$ type Burgers vectors of the type $1/3\langle11\bar{2}0\rangle$. Figure

2.9 illustrates the position in the hcp structure of (i) the basal plane (0002), (ii) one of the six possible prismatic planes, $(01\bar{1}0)$, and (iii) one of the six possible pyramidal planes, $(1\bar{1}01)$. Twinning was most frequently observed to occur on the $\{10\bar{1}2\}$ planes [107, 109-113] and $\{1\bar{2}11\}$ planes [107, 111-113]. In addition, evidence of twinning on the $\{1\bar{2}12\}$ [107, 109-113], $\{1\bar{2}13\}$ [107] and $\{1\bar{2}14\}$ [107] planes has been found, however the shuffles associated with these modes are complex and consequently they are far less commonly observed.

2.4.1 von Mises Criterion

According to von Mises criterion, a polycrystal requires five independent shear systems to undergo homogeneous strain without a change in volume [114, 115]. A slip system is independent of others provided that its operation cannot be produced by a suitable combination of slip on other systems [116]. Of the six types of slip system available in hcp metals [107], the operation of only <a> type, $<11\bar{2}0>$, slip in commercially pure titanium cannot satisfy the von Mises criterion. It was therefore suggested by Tegart [117] that other slip systems in titanium must operate in which the dislocations have a component of the Burgers vector in the c direction. Such slip has been observed to occur with Burgers vectors of the type $1/3<11\bar{2}3>$ on the $\{11\bar{2}2\}$ and $\{10\bar{1}1\}$ planes and is identified as <c + a> slip [118-123].

In fine-grained commercial titanium alloys, twinning is not an important macroscopic mode of deformation [12] but it is interesting to note that $\{10\bar{1}2\}$ twins may activate various <c + a> type dislocations by interaction with <a> type dislocations [12, 107]. Such twin/dislocation interactions may account for the increased ductility observed in titanium (and zirconium) at temperatures approaching absolute zero which gives titanium a considerable cryogenic potential [107].

2.4.2 The Critical Resolved Shear Stress

The stresses required to activate the deformation modes in hexagonal metals are very dependent upon the orientation of the stress axis. This is demonstrated by plotting the Schmid factor, m, for each deformation mode:

$$m = \sigma_s/\sigma_n = \cos\phi\cos\lambda \qquad (2.6)$$

where σ_s = the shear stress resolved on the slip (or twin) plane and in the slip (or twin) direction (MPa)
σ_n = the applied stress (MPa)
ϕ = the angle between the stress axis and slip (or twin) plane normal
λ = the angle between the stress axis and slip (or twin) plane direction

Figure 2.10 shows the orientation dependence of the Schmid factor, m, versus the angle ϕ for slip on the most highly stressed basal and prism slip systems [107] in conjunction with a standard unit stereographic triangle for a hcp metal. The triangle was formed by drawing great circles through (0001), $(11\bar{2}0)$ and $(10\bar{1}0)$ poles.

σ_s must attain a critical value, the critical resolved shear stress (CRSS), before slip (or twinning) can occur on a given plane. The CRSS for different modes of deformation varies and thus, although the Schmid factor of a particular mode may be favourable, deformation on that mode may not occur if a mode with a lower CRSS is able to operate at a lower orientation factor to the stress axis. For example, twinning requires a high CRSS to be reached before it can operate, so even if the orientation factor for twinning is ideal, slip can preferentially occur at a lower stress and at a less-than-ideal orientation due to the lower CRSS for slip [107].

For basal slip, m is zero for all $\{11\bar{2}0\}$ slip vectors when the stress axis is parallel or normal to the c-axis. The

Schmid factor reaches a maximum value of 0.5 when $\phi = \lambda = 45°$ [107] (see Figure 2.10). For prism slip, the resolved shear stress on $(01\bar{1}0)[2\bar{1}\bar{1}0]$ varies from a maximum, when the stress axis is normal to the c-axis, to zero when the stress axis is parallel to the c-axis.

2.4.3 Effect of Interstitial Content

Table 2.7 shows the CRSS's and ratios of CRSS for <a> type ($(0001)<11\bar{2}0>$, $\{10\bar{1}0\}<11\bar{2}0>$ and $\{10\bar{1}1\}<11\bar{2}0>$) slip measured in studies of single crystals [109, 111, 112, 124] and polycrystals [110] of commercially pure titanium, with the interstitial contents indicated. In zone-refined titanium with an interstitial content of 4 x 10^{-4} at% O_{eq} (where O_{eq} = O + 2N + 0.75C in at% [100]), Levine [124] calculated that basal and prism slip had CRSS's of 8 kg/mm² and 2 kg/mm² respectively at room temperature. There is a preference for slip on the plane with the lowest value of CRSS and, therefore, in the case of titanium with low interstitial content, this corresponds to a preference for slip on the prismatic plane with secondary slip occurring on the (0001) and $\{10\bar{1}1\}$ planes [107, 124].

Churchman [109] reported that increasing the interstitial content of single crystal specimens led to increased slip on basal and pyramidal planes. This is reflected in the ratio of the CRSS's which are given in Table 2.7. For example, the ratio for prism to basal slip decreased from 1:3 to 1:1.2 on increasing interstitial content from 0.01 wt% (O + N) to 0.1 wt% (O + N) [109]. A possible mechanism for the role of oxygen in titanium was proposed by Churchman in which hard sphere models of the hcp lattice were used to indicate the positions of oxygen atoms. The sites occupied by these atoms were said to obstruct slip on two of the three possible slip planes in titanium, namely, the basal and prism planes. The model provided an explanation for the variation of the relative values of the CRSS with interstitial impurity content; changes in

the oxygen concentration at low total oxygen contents had a much more marked effect on the CRSS for slip on the basal and prism planes than on the pyramidal planes, which agreed with the experimental observations [109].

A comprehensive review of the effects of interstitial solutes on the strength and ductility of titanium was compiled by Conrad [100]. The review discusses the effects of very dilute solid solutions (< 1 at%) of oxygen, nitrogen and carbon on the deformation kinetics, strain hardening, grain size hardening, ductility and fracture of single crystals and polycrystals of unalloyed titanium. Three temperature regions were considered: (i) Low temperatures $T/T_m < 0.3$ (T_m = melting temperature in Kelvin). (ii) Intermediate temperatures, $0.3 < T/T_m < 0.4$. (iii) High temperatures, $T/T_m > 0.4$. Most attention is given to the more documented, low temperature regime.

A summary of the data in the literature on the effects of temperature and purity on the CRSS for prism slip in titanium was presented in graphical form [100]. The effects on the most pure material (O + N + C = 0.05 at%) are illustrated in Figure 2.11. The occurrence of a plateau in the curve at intermediate temperatures (approximately 600 - 800 K), suggested that the CRSS for prism slip below 800 K (0.4 T/T_m) consisted of two components. These were a thermal component, τ^*, which was sensitively dependent on temperature, T, and strain rate, $\dot{\gamma}$, and an athermal component, τ_μ, which varied with the modulus, μ, such that:

$$\tau_{CRSS} = \tau^*(T, \dot{\gamma}) + \tau_\mu(\mu) \qquad T < T_c \qquad (2.7)$$

$$\tau_{CRSS} = \tau_\mu \qquad T > T_c \qquad (2.8)$$

T_c = the initial temperature at the plateau and is 600 K for prism slip (see Figure 2.11) [100]. The effects of temperature and strain rate on the CRSS for basal slip in high purity titanium are compared to that for prism slip

in Figure 2.11 (T_c for basal slip is approximately 800 K). Figure 2.12 shows the effect of the interstitial solute content on the CRSS for basal slip [100, 109, 112, 124] and prism slip [100] in titanium at 300 K. It was concluded that basal slip exhibits a stronger temperature and strain rate dependence of the flow stress but a weaker dependence on the interstitial content. The relatively small amount of data regarding pyramidal and $\langle \underline{c} + \underline{a} \rangle$ slip in titanium implies that comparisons cannot be made on these systems [100].

The results of many studies on the deformation of titanium single crystals and polycrystals at low temperatures [100, 109, 111, 112, 119, 124-127] indicates that; (i) the principal slip mode is $\{10\bar{1}0\}\langle 11\bar{2}0\rangle$, (ii) the stress for this slip mode increases with an increase in interstitial content at all temperatures, (iii) the ratio of the stress for the systems (0001) and $\{10\bar{1}1\}$ to that for $\{10\bar{1}0\}$ slip increases with purity and (iv) the temperature dependence of the yield or flow stress increases with interstitial content and is independent of the strain or grain size. These and other considerations suggest that the low temperature deformation kinetics of single crystals and polycrystals of titanium are associated with the thermally activated breakdown of interstitial solute obstacles by dislocations moving on the first order prism planes [100].

A number of suggestions concerning the rate controlling mechanism for basal slip have been proposed. Levine [124] proposed that the Peierls force, or lattice friction, was rate controlling at temperatures below 400 K and Akhtar and Teghtsoonian [128] concluded that cross-slip was rate controlling for basal slip at temperatures from 500 K to 1100 K. Somewhat better agreement between observed and predicted slip plane preference was obtained when the stacking fault energies on both basal and prism planes were considered in terms of the relative phase stability, as discussed by Conrad [100]. Interstitial solutes are believed to influence the effect of temperature on the

relative ease of prism/basal glide through their direct interaction with dislocations, as well as their indirect effect through the stacking fault energy [100].

2.4.4 Aluminium Additions

The addition of up to 5 at% aluminium to titanium does not appreciably influence the effect of interstitial solutes on the thermal component of the CRSS for basal and prism slip at low temperatures. The effect of aluminium is on the athermal component of the flow stress [100]. However, additions of aluminium have a significant effect on the dislocation structure and strain hardening of titanium alloys.

Blackburn and Williams [118] studied the dislocation arrangements in deformed specimens of titanium containing 0 to 25 at% aluminium and 0.3 to 0.6 at% oxygen. In commercially pure titanium, cellular distributions of dislocations occurred with an average cell diameter of 0.5 to 1.0 μm. Many dislocation loops were also formed. As the aluminium content increased, the number of dislocation loops decreased. The addition of 5 at% Al resulted in a more homogeneous distribution of dislocations with neither a well defined cell structure nor planar groups of dislocations. Such planar groupings were observed in alloys with greater than 10 at% Al and allowed an analysis of the active slip planes to be made. Slip on the $\{10\bar{1}0\}$ planes dominated at low strains, but slip on $\{10\bar{1}1\}$ planes and, to a lesser extent, on the (0001) plane was found at higher strains. Further increases in the aluminium content produced narrower slip bands and an increase in the volume fraction of the α_2 phase. In alloys containing > 10 at% aluminium, dislocations near the head of a planar array were found to occur as pairs. As the number of dislocations that passed along a glide plane increased, the amount of pairing decreased. The changes in dislocation arrangement with increasing aluminium content were considered to rise, in part, from the development of

short range order and ordered particles in the alloys and this was confirmed by the presence of dislocation pairs at the head of the planar arrays [118].

The planar slip in Ti-Al alloys is determined to arise as a result of a decrease in the CRSS of the active slip plane, rather than a change in the ability of screw dislocations to cross-slip [129]. This is in contrast to the situation in fcc alloys where an increase in the solute content reduces the stacking fault energy and the ability to cross-slip [129].

2.5 FATIGUE BEHAVIOUR

To be able to predict when a component in an aero engine will fail under all conditions to which it may be exposed, requires a thorough understanding of its fatigue behaviour. Fatigue testing usually involves cycling specimens to failure in order to predict a lifetime or number of cycles to failure, N_f, of a component. The prediction is subsequently used to remove the component from service after around 40% N_f. As finer, more highly alloyed and more microstructurally complicated alloys are developed, the demands on the fatigue integrity are consequently increased. In addition to this, the designer is currently looking to operate components up to two-thirds N_f before removing them from service. Better fatigue modelling might allow this operating time to be extended. To this end, metal fatigue still remains an expanding and interdisciplinary subject.

There are four phases of crack growth generally accepted in the literature [1]. These are illustrated in Figure 2.13 and are summarised: (i) Initiation - the formation of a sub-grain-size crack. (ii) Short crack growth - a mixture of crack growth within a grain and crack arrest at the grain boundaries, which is microstructurally dominated. (iii) Steady or long crack growth - a function of geometry and stress which obeys linear elastic fracture

mechanics (L.E.F.M.) and is independent of microstructure. (iv) Rapid fracture - unstable crack growth under steady loading.

The application of L.E.F.M. to long crack growth is now well understood, apart from materials of very high toughness which require alternative prediction algorithms [130]. Research is now concentrating on short fatigue crack growth, the current understanding of which is discussed in sections 2.5.2 and 2.5.3. As the prediction of component life has become increasingly critical, an improved understanding of the fatigue crack initiation and damage accumulation mechanisms in metals and alloys is necessary. Fatigue crack initiation in titanium and titanium alloys is discussed in section 2.5.6.

2.5.1 Long Fatigue Crack Growth

For over 150 years the study of fatigue has involved the use of S-N endurance curves (where S is the applied stress and N is the number of cycles) such as those in Figure 2.14 [131]. The interpretation of these curves has been the subject of much research and intense discussion by materials scientists, materials engineers and mechanical engineers [130].

L.E.F.M. analysis of crack tip stress-strain fields in a component enables designers to estimate the period of long crack growth lifetime between an initial defect size as small as half a millimetre [132], to the final crack size, which can be as large as several hundred millimetres. The use of L.E.F.M. is of considerable benefit to engineers, permitting a direct comparison between large engineering structures and small laboratory specimens via the use of the elastic stress intensity factor, ΔK ($MN/m^{3/2}$) [130, 132, 133]:

$$\Delta K = Y\Delta\sigma(\pi a)^{1/2} \qquad (2.9)$$

where:

Y = specimen geometry and loading system factor

$\Delta\sigma$ = cyclic stress range (N/m^2)

a = the crack length (m)

However, L.E.F.M. is limited to cases where the plastic zone size associated with the crack tip is less than one fiftieth of the crack size and can therefore be ignored.

Commercial pressures to develop more advanced materials and to perfect new techniques for monitoring the growth of small cracks has led to the inability of L.E.F.M. to characterise the behaviour of very small cracks. This is attributable to the fact that the plastic strain field of a small crack can be the same size as the crack, rendering the use of L.E.F.M. inapplicable. A recent development in the interpretation of short fatigue crack growth is based initially on an understanding of the fatigue limit [130].

2.5.2 The Fatigue Limit

The fatigue limit is a limit on the ability of a crack to propagate to failure or the stress required to overcome the strongest barrier to crack propagation. Figure 2.15 illustrates that at cyclic stress levels, $\Delta\sigma_3$, $\Delta\sigma_4$ and $\Delta\sigma_5$, failure does not occur since the crack is arrested at barriers b_3, b_4 and b_5, *e.g.* α-platelet, colony and grain boundaries respectively. At $\Delta\sigma_2$, which is greater than the fatigue limit, these barriers are not sufficiently strong to arrest the crack and so failure ultimately occurs [130].

In order to appreciate the behaviour of short cracks, analytical models incorporating three separate zones have been proposed [132]. The zones vary in extent depending on the material under investigation. An example is given in Figure 2.16. Zone A-B represents the microstructurally short crack (MSC) growth regime. Zone B-C is referred to as the physically short crack (PSC) growth regime and zone

C-D corresponds to low stress, linear elastic fracture mechanics type cracks.

Microstructural barriers b_5, b_4 and b_3 of increasing resistance are illustrated in the microstructurally short crack (MSC) growth regime and match the conditions shown in Figure 2.15. According to Miller [134], it is the thermomechanical control of these barriers, in terms of their position, size and strength, that will provide the higher fatigue resistant materials of the future.

2.5.3 Short Fatigue Crack Growth Rate

The fatigue crack growth rate from Figures 2.15 and 2.16 varies according to Figure 2.17. At the lowest value of the stress range, $\Delta\sigma_5$, the MSC grows until it is stopped at the fatigue limit represented by the barrier b_5. It can only continue to grow under the same stress range if it has a length greater than a_5. Even if the stress is increased to the range $\Delta\sigma_3$, which is sufficient to overcome the barrier, b_5, the crack is arrested by the stronger barrier, b_3. However, if the stress range $\Delta\sigma_2$ is imposed, fatigue failure occurs since the MSC growth curve and PSC growth curve cross at this stress range which is sufficiently high to overcome all the barriers (b_5, b_4 and b_3).

All the zones of fatigue crack growth behaviour identified require their own branch of fracture mechanics to fully characterise their behaviour [130]. Miller [130, 132, 134] reviewed the extent and practical relevance of each zone with the effects on short fatigue crack growth that could arise from crack closure, environment, surface preparation and notching of specimens.

The manufacture of safe and long-life engineering components requires a detailed understanding of the factors affecting the short crack growth behaviour of the metal or alloy. These factors include: (i) The type of

test and geometry of test specimen, R ratio ($\sigma_{min}/\sigma_{max}$), frequency of testing and load pattern (square wave, sinusoidal etc.). (ii) The microstructure and prior processing history of the material, *i.e.* grain size, secondary phase distributions, inclusion sizes, orientation and distribution. (iii) Test environment. (iv) Test temperature. (v) Surface topography of the test specimen.

In fact, as stated by Miller [130], all the classical work of the past 150 years, which characterised long crack fatigue behaviour and fatigue limits can now be reanalysed from the point of view of short fatigue crack growth.

2.5.4 Fatigue Crack Initiation

Crack initiation plays an important role in the fatigue life of either a component in a structure or a specimen in a laboratory, and is one of the major aspects of all fatigue studies. It is of interest to be able to define fatigue crack initiation as it is then possible to ascertain the periods of lifetime required for the crack to initiate and consequently to propagate to failure.

Miller [134] considered the fatigue lifetime to be composed entirely of fatigue crack propagation from an initial defect size, a_0, as small as 2 to 3 μm (micronotches on an engineering surface) to the final crack size, a_f. To simplify calculations, a_0 was assumed to be zero since the growth of a crack from 0 to 3 μm was said to make minimal difference to the lifetime. For example, in Figure 2.15 it was assumed that the fatal fatigue crack and its associated plasticity were initiated simultaneously in the first fatigue cycle.

Funkenbusche and Coffin [135] defined crack initiation as the formation of a crack which was detectable using the scanning electron microscope (approximately 1 μm). As a consequence, cracks were considered to initiate after 3%

to 30% of the total fatigue lifetime, depending upon the scatter of the results obtained and on the cyclic strain amplitude [21, 135]. A new theory of crack initiation based on the accumulation of dislocations in slip bands was developed by Lin *et al.* [136] whereby fatigue cracks were shown to be less than 0.5 μm in size when first initiated.

Many workers have shown that the duration of crack initiation occupies the first 50% to 90% of the total fatigue lifetime in high strength materials [137-139]. Provan [137, 138], for example, considered that the initiation and coalescence of microcracks led to a macroscopic crack over the first 90% of the total fatigue life and has endeavoured to derive the Provan reliability law based entirely on the modelling of fatigue crack initiation and propagation [137].

Clearly the definition of crack initiation is a debatable one and a large amount of confusion concerning this issue has been generated. With an ever increasing number of more detailed theories and investigations, this issue will no doubt continue to be raised.

2.5.5 Damage Accumulation in Copper

Research into fatigue damage accumulation and crack initiation mechanisms has concentrated on lightly alloyed metals, in particular, copper [137, 138, 140-142]. This is understandable since the fundamental processes in lightly alloyed metals are more easily observed and interpreted than they are in more heavily alloyed materials containing precipitates and secondary phases, such as titanium alloys.

The theory behind fatigue damage accumulation in pure polycrystalline materials, such as face centred cubic (fcc) copper, nickel and silver, and to a lesser extent in body centred cubic (bcc) metals such as α-iron and 0.1%

carbon steel, is based on an understanding of the behaviour of persistent slip bands (P.S.B.'s) [137, 138, 140-144].

As long ago as 1902 P.S.B.'s were observed by Ewing and Humfrey [145] who reported that: (i) Slip bands formed in favourably orientated crystallites. (ii) With increasing strain new bands developed and old ones widened. (iii) The slip band markings were decidedly above the general surface, and were rough and jagged. (iv) Cracks developed at the slip bands. (v) There was a stress amplitude below which slip bands were not observed. (vi) There were fewer bands at lower stresses than at higher stresses.

More recently, theoretical studies on crack nucleation in copper focuses on the effect of internal stresses within the P.S.B.'s, the development of the surface profile of P.S.B.'s and the identification of the most likely sites for crack formation. Various dislocation mechanisms for the production of extrusions and intrusions have been proposed, theories have been formulated and an ever increasing number of investigations using novel experimental procedures have been made in order to accumulate data and knowledge on all aspects of the subject [137, 138, 140-143, 146-150].

For low strain amplitude fatigue in lightly alloyed fcc metals, cyclic hardening initiates fatigue damage by changing the microstructure of the material to a vein structure of unidirectional dislocation structures. A saturation stage is reached where cellular bundles of dipole and multipole dislocation configurations act as effective barriers to continued dislocation motion [137, 141, 142, 147]. At this saturation point the hardening rate slows to zero. Watt *et al.* [146] observed that the micromechanical structure of the material changes with the achievement of saturation. Strain localisation manifests itself in the evolution of surface relief which is

characterised by depressions and elevations along the lines of intensive slip [150]. These depressions and elevations develop into intrusions and extrusions, or persistent slip bands, either within a grain or at grain boundaries (persistent slip grain boundaries) [150]. The term persistent slip band originated from the "persistence" of some of the slip bands formed during fatigue tests when a thin layer had been removed from the surface by electropolishing [138]. The P.S.B. has been extensively researched [137, 138, 141-143, 148, 150]. Its ladder-like structure consists of highly concentrated dipole edge dislocations, of the order of 10^{15} /m^2 [151], in the walls (approximately 1 to 1.5 μm apart) and a screw dislocation density between the walls as high as 10^{13} /m^2 [138]. The motion of dislocations inside the walls and a P.S.B. formation theory for low strain amplitude fatigue have been proposed by Kuhlmann-Wilsdorf and Laird [147]. The extrusions and intrusions which form at the surface of a test specimen to a height and depth of up to 4 μm, respectively [136, 142], act as stress raisers to initiate microcracks along the interface between the P.S.B. and the matrix [143]. When P.S.B.'s intersect with a free surface, the microcracks nucleate transgranularly, whereas intergranular cracking is observed at persistent slip grain boundaries. Once the microcracks have initiated, they propagate along slip planes to form macrocracks.

Although much progress has been made, a general observation is that due to the complexity of the fatigue damage mechanism, this area of fatigue is still in a qualitative rather than a quantitative stage [138].

2.5.6 Damage Accumulation in Titanium Alloys

2.5.6.1 Commercially Pure Titanium

Both twins and slip bands are known to operate as deformation modes in commercially pure α titanium (section 2.4) but the preferred sites for fatigue crack

initiation have been found to vary. Preferential cracking on twin boundaries was observed by Partridge [152], Stevenson [153] and at low strains by Sugano and Gilmore [154]. Suhua *et al.* [155] observed cracks to initiate at grain boundaries which separated highly misorientated grains whose dominant deformation modes were different. Some cracking from slip band interaction on prism planes was also observed [155]. Slipless cracking, believed to be geometrical in nature, was found at low frequencies [156] and at high frequencies [157, 158]. However, the most commonly reported sites for crack initiation in α titanium alloys are planar slip bands in the α phase [113, 154, 157-160]. It was shown that, as the frequency of testing increased; (i) a decrease in the number of grains with slip bands and cracks was observed, and (ii) an increase in the percentage of life to crack initiation and number of cycles to failure (N_f), occurred [157, 158].

2.5.6.2 Ti-6Al-4V

Due to its extensive use in aero engines, considerable interest has been generated in the low cycle fatigue behaviour of the α+β alloy Ti-6Al-4V [21-25, 27, 161, 162]. Low cycle tests were carried out at frequencies between 30 Hz and 1 cycle per minute (cpm). The large variation in microstructure encountered in different forgings of this alloy stimulated research to identify the preferred sites of crack initiation and to observe the early stages of crack propagation in relation to the microstructure.

In a study of Ti-6Al-4V by Wells and Sullivan [21], surface crack initiation occurred early in life (around 5 to 10% N_f), after low cycle fatigue at room temperature (testing at a frequency of 1 to 2 cpm). Crack initiation occurred on the scale of the primary-α phase, primarily along slip bands, with some cracking along the boundaries between the primary-α and transformed-β phases. Fatigue crack initiation along slip bands was also observed in

Ti-6Al-4V in the primary-α and transformed-β [22, 27] and along intense planar slip bands normal to the α/β interfaces in Widmanstätten microstructures [162]. Only rarely was α/β interface cracking observed in these investigations [22, 27, 162] but extensive studies by Sparks and Long [163] found crack nucleation at the α/β interface regardless of microstructure in twenty three different α+β alloys including Ti-6Al-4V.

A probable mechanism for crack initiation along localised slip bands was proposed by Brown and Smith [27]. Dislocations on a slip plane in the primary-α phase pile up against a β particle. When the stresses at the head of the pile-up reach a sufficient magnitude, a crack initiates and grows back along the plane of weakness represented by the slip line.

Fatigue deformation in annealed Ti-6Al-4V microstructures has been observed to be localised and associated with phase or grain boundaries [25]. The presence of β phase appears to be an integral factor in the initiation of a microcrack, particularly in the case of an α+β annealed specimen [25]. A mechanism of fatigue crack initiation has been proposed to explain how the accumulation of damage leads to cracking at the grain boundaries [25]: During fatigue cycling, jogged dislocations moving on highly strained slip planes create a trail of vacancies as they move to and from an impenetrable obstacle, such as a grain boundary. The sheets of vacancies so formed can coalesce to form a larger microcrack in the vicinity of the impenetrable grain boundary barrier.

2.5.6.3 High Temperature Alloys

Recent investigations on the low cycle fatigue behaviour of more advanced α+β and near-α titanium alloys have concentrated on the short crack propagation behaviour. Despite this, many of the studies have suggested sites of fatigue crack initiation. The majority, reported crack

initiation to occur on planar slip bands either; (i) across transformed-β colonies in β-processed microstructures [9, 17, 38, 40, 42, 43, 73, 95, 164] or (ii) across primary-α grains [135, 165-169] and/or transformed-β colonies [99, 165, 166] in duplex (α+β processed) microstructures. Crack initiation along α/β interfaces was observed at low strains in Ti-6246 [165, 166] and in low temperature α+β processed Ti-17 [135]. In both cases extrusion formation was observed as a precursor to crack initiation in these microstructures. Four possible mechanisms of extrusion formation were postulated and are discussed in detail by Mahajan *et al.* [165].

Many studies show that intense slip lines and slip related cracks in β-processed, Widmanstätten and basketweave microstructures extend across a colony seemingly uninhibited by the α/β interfaces at the α-platelet boundaries [9, 17, 38, 40, 42, 43, 73, 95, 162, 164, 170, 171]. Crack or slip band arrest most frequently occurs at grain or colony boundaries where slip transferal into the adjacent grains/colonies is not possible due to the high angles associated with these boundaries. In most cases, the planes on which the slip occurs are determined to be the prism and/or the basal planes. Such behaviour is consistent with the fact that colonies of similarly orientated α-platelets transform from the β phase according to the Burgers orientation relationships, equations 2.1 to 2.3 in section 2.2.4.2. Consequently, slip in the α-platelets is readily accommodated by slip in the β phase and, although the β phase offers some resistance to dislocation motion in the α phase [38], the β phase does not act as a major barrier to slip (in some cases [41, 105, 162, 171] the β phase acts as an effective crack stopper, as discussed later in this section).

The yield strength has been found to depend on the colony size in a similar manner to a Petch type relationship [38, 95]; a decrease in colony size results in an increase in

the yield strength. Thus, the colony size can be thought of as the effective grain size in the β-processed (Widmanstätten) microstructures [172]. In subsequent investigations, an effective colony size has been proposed [43] to account for cases where two (or more) adjacent colonies share a common basal plane and thus deform as if they are a single colony [38, 43]. The upper limit of α-colony size is the prior-β grain size [43]. A fine β-grain size, achieved by close control of the forging route (section 2.3.1), is therefore very desirable as it results in good fatigue crack initiation life (Table 2.4). This limits the size of the initial fatigue crack, thereby increasing the number of cycles of crack propagation to failure [40, 95]. A fine β-grain size also results in an improved ductility (see Table 2.4).

In slow (furnace) cooled microstructures, the α-platelet boundaries (not the colony boundaries) are the slip/crack arresting features when the retained-β phase is relatively thick and continuous across the α/β interface [41, 105, 162, 171]. T.E.M. evidence [41, 105] has suggested that α-platelets thicker than approximately 2 μm can strongly deviate cracks by up to 80° along α/β interfaces without undergoing any plastic deformation. The retained-β phase which is obtained on slow cooling has been observed to provide a route for deviation of the crack path when its thickness is of the order of 0.2 μm. Several mechanisms by which the thick retained-β phase may retard cleavage crack growth have been suggested [162, 171]. It is possible that a combined effect of thicker α-platelets and retained-β phases might be relevant to the mechanisms of crack retardation in slow cooled microstructures [171]. It has been shown however, that the thickness of α-platelets, and not necessarily the Widmanstätten colony size, may govern the intrinsic crack growth resistance in titanium alloys [171].

2.5.7 Introduction of a Dwell Period at Maximum Load

The load pattern of many aircraft structures, including turbine and compressor discs, essentially consists of a load applied at take-off which is held at a constant level during cruise and removed on landing. Since the in-service failure of RB-211 fan discs of IMI 685 in the early 1970's, the introduction of a holding time at the maximum load, has received much attention with respect to its effect on the low cycle fatigue behaviour of titanium alloys.

To simulate in-service conditions in laboratories, load (or strain) is held at the maximum value of the cycle for a given period of time, referred to as the dwell time (or hold time). The response to the introduction of a dwell-on-load has been extensively studied as the conditions of testing can be as widespread as those for normal continuous fatigue cycling. For example, the effects of microstructure, temperature of testing, load level, texture, specimen size and shape and environment have been considered for a given alloy as well as the effects of different dwell durations.

In the first studies of dwell effects, Ryder *et al*. [173] ran a number of fatigue crack propagation experiments on specimens of IMI 685 with different microstructures using different dwell times, temperatures and environments. The effect of introducing a dwell at maximum load increased the fatigue crack growth rate compared to continuous fatigue tests. A maximum influence of dwell occurred at hold times between 15 seconds and 1 minute at maximum load. No obvious effect of temperature on fatigue crack growth rate was found between -40 and 150°C, however, the effect of a dwell on load decreased as the temperature was raised to 300°C. A larger detrimental effect on the fatigue crack growth rate was found in tests carried out in de-ionized water compared to laboratory air. Further

studies on the response to dwell time conditions have concentrated on IMI 685 and Ti-6Al-4V since these alloys have the widest application in the aircraft industry.

2.5.7.1 Microstructural Effects

Eylon and Hall [40], Postans and Jeal [174] and Evans and Gostelow [175] tested IMI 685 with an aligned α-platelet microstructure with and without a five minute dwell on load. Postans & Jeal and Evans & Gostelow showed that there was a definite increase in fatigue crack growth rate in specimens which had been dwell tested. However, no discernible fatigue crack growth rate increase was observed between non-dwell and dwell test specimens by Eylon and Hall [40]. Bania and Eylon [176] worked on a range of microstructures and textures of Ti-6Al-4V. They did not find a fatigue crack growth rate increase which was caused by the introduction of a dwell on load; infact, for certain microstructures, the fatigue crack growth rate during dwell tests was lower than that in non-dwell specimens. Postans and Jeal [174] carried out similar tests on IMI 685 containing a basketweave microstructure. No difference in the fatigue crack growth rates between the tests was detected in these specimens.

Although no significant difference was found in the fatigue crack growth rates between non-dwell and dwell test specimens, Eylon and Hall [40] observed a large 'dwell debit', or reduction in the number of fatigue cycles to failure (N_f), in test specimens of IMI 685. In the most severe case, tests were conducted at a maximum load of 827 MN/m² and frequency of 0.33 Hz, and the number of cycles to failure of five-minute-dwell test specimens was reduced by an average of 98.6% compared to non-dwell tests. During five-minute-dwell tests at 750 to 850 MN/m² and 2.4 Hz, a reduction in N_f by 94% was found by Evans and Gostelow [175], confirming the observations made by Eylon and Hall [40]. Evans [177] concluded that the dwell effect in IMI 685 was sensitive to microstructure. The

number of cycles to failure was most severely reduced when the alloy was slow cooled following its heat treatment to produce an aligned α-platelet microstructure.

A recent study by White *et al.* [178] found that a marked decrease in the fatigue lifetime was particularly notable in β-processed near-α alloys such as IMI 829. T.E.M. observations revealed no significant difference in the deformation modes observed in dwell and non-dwell test specimens. However, a higher dislocation density was observed in the dwell test specimens and was consistent with the higher strain associated with the dwell tests.

The paths of crack growth were studied by Postans and Jeal [174] in basketweave-α and aligned-α microstructures of IMI 685. In the non-dwell specimens, cracks propagated through α-platelets sometimes crossing several different colonies without changing direction by using different slip planes in each. A strong tendency for cracks to propagate along the basal planes in the α phase was noted in the specimens subjected to a dwell on load and, as a result, the crack path frequently changed direction causing a more tortuous crack path morphology.

2.5.7.2 Texture Effects

Stubbington and Pearson [179] studied the dwell effect in Ti-6Al-4V at frequencies of 0.3 and 25 Hz. Test pieces were cut from a forged and rolled bar with a strong preferred orientation. When the stress direction was parallel to the basal plane, the cracks ran approximately normal to it and the crack growth rate under dwell cycling at room temperature was similar to that for continuous cyclic fatigue testing. When the stress was normal to the basal plane, the cracks ran approximately parallel to the basal plane and the crack growth rate under dwell increased considerably. The fatigue crack growth rate was increased by increasing both the dwell time and stress intensity factor (ΔK). Tests were also carried out with

the plane of maximum stress at approximately 30° and 70° to the basal plane. The results showed that the specimens with their basal planes closest (30°) to the maximum stress plane had a much greater dwell effect than those with the basal plane further away (70°) from the maximum stress plane.

Although the material used by Evans and Gostelow [175] was not highly textured, X-ray analysis showed a strong tendency for the fracture planes to lie parallel to the basal planes. Facets on the fracture surfaces of IMI 685 tested with and without a five-minute-dwell on load were examined by Davidson and Eylon [180] using selected area channelling. The crystallographic planes of the facets were identified as near-basal. For non-dwell specimens 75% of the initiation sites were at the surface of the test specimen, whereas for dwell tested specimens 80% of the initiation sites were subsurface [180]. Evans [181] proposed that subsurface cracking was more prevalent if specimens were highly polished, the mean stress was high or there was a dwell at maximum load. Calculations suggested that facet formation, and hence subsurface crack nucleation was associated with the attainment of a critical level of strain [181].

2.5.7.3 Temperature Effects

Stubbington and Pearson [179] found that the increase in fatigue crack growth rate produced by cycling with a dwell at maximum load was greater at 20°C than at 40°C and became negligible above 75°C. Evans and Gostelow [175] carried out tests on IMI 685 at 150°C and also observed that the increase in fatigue crack growth rate caused by a dwell on load effectively disappeared. However, a significant reduction in the number of cycles to failure (up to 96%) in dwell specimens was still observed [175]. The explanation given for this divergence of behaviour was that the material in the specimens and the material ahead of the crack tip experienced different stress states

[175].

Neal [45] reported that the influence of dwell on cyclic life reduced as the temperature of testing increased, such that from about 200°C to 400°C there was no influence of a dwell on load and above 400°C the effect of dwell returned. The effects were explained by dynamic strain ageing occurring at between 200 and 400°C and by true creep-fatigue interactions taking place at higher temperatures (> 400°C). The effect of a dwell on load at low temperatures (< 200°C) was extensively investigated [45]. The alloys studied included Ti-6Al-4V, IMI 550, IMI 679, IMI 685, IMI 829, Ti-6242S and an experimental alloy of very high alpha stabiliser content. None of the alloys exhibited any loss in N_f at 200°C but at 20°C losses of up to 75% were seen, as summarised in Table 2.8. Neal [45] related the degree of cycle life loss with dwell in the various alloys examined to their aluminium and molybdenum equivalents, such that a greater cyclic loss could be expected in alloys containing a higher aluminium equivalent and lower molybdenum equivalent. The model for the dwell effect given by Neal [45] is discussed in section 2.5.7.5.

2.5.7.4 Hydrogen Additions

Almost all investigations observed that quasi-cleavage facetting at subsurface nucleation sites was closely associated with a reduction in N_f and an increase in fatigue crack growth rate, associated with introducing a dwell on load into the fatigue cycle. Many investigators, including Postans and Jeal [174], Stubbington and Pearson [179] and Evans and Gostelow [175], proposed that strain-induced hydrogen interaction with dislocations at, and near, a crack tip was responsible for this effect. To this end, several investigations have been carried out to study the effect of deliberately introducing hydrogen in various concentrations into the material prior to testing.

An increase in hydrogen concentration from 40 ppm to 140 ppm was shown to dramatically reduce the fatigue life [182]. Evans [183] illustrated that hydrogen acted as a strengthening element in IMI 685 up to a concentration of 60 ppm, improving both continuous and dwell fatigue lives. However, at higher concentrations of hydrogen the strength was maintained, but premature failure occurred due to a reduction in ductility. The role of hydrogen was complex and was found to affect basketweave and aligned-α microstructures to different degrees [183].

Neal [45] observed that hydrogen did not play a part in the dwell process. On comparing dwell and non-dwell lifetimes, degassed material (IMI 685) of less than 10 ppm hydrogen produced virtually identical losses in N_f to material containing 50 ppm (as received) and material hydrogenated to 190 ppm.

2.5.7.5 Proposed Models

Evans and Gostelow [75] demonstrated that the quasi-cleavage facets, which were commonly observed in dwell tested specimens, could also form during creep deformation at ambient temperatures. Fracture surfaces in the dwell test specimens were virtually identical in appearance to those from static creep experiments. Furthermore, the times to failure in dwell and creep tests were quite similar, thereby indicating that the number of cycles to failure in dwell tests was merely the number of periods at peak stress that were necessary for the creep failure strain to be attained. The implication was that facet formation was a function of the plastic strain accumulation at peak stress rather than being dependent on the response of the material to stress reversals. It was therefore proposed that the low cycle fatigue dwell effect and facet formation under cyclic conditions was caused by time dependent plastic strain accumulation. Hydrogen was said to influence this behaviour by inter a cting with the dislocations and enhancing the hardening process [175].

Evans [184] concluded that, at the comparatively low concentrations of hydrogen relevant to the service applications of high temperature titanium alloys, the role of hydrogen is secondary to time dependent deformation.

White *et al.* [178] also concluded that the accumulation of strain in the dwell test specimens was primarily attributable to time dependent deformation accrued during the dwell on load part of the fatigue cycle. A comparison between the creep and dwell curves showed that higher rate of strain accumulation in the dwell test specimens could not be attributed to creep alone but may have been caused by a greater degree of surface cracking observed in the dwell specimens arising from the interaction of creep and fatigue.

Neal [45] believed that the basic mechanism of the dwell effect during fatigue and creep were the same, namely planar slip in the α phase on, or near to, the basal plane. The anomalies in the results of dwell tests by different workers could be reconciled by examination of the texture of the material used. High levels of α-stabilisers and low levels of β-stabilisers promoted the creep-fatigue interactions at ambient temperatures, (Table 2.8) and at temperatures of around 150°C, the dwell effect reduced to zero. No evidence was found to suggest that hydrogen was involved in the dwell effect [45].

CHAPTER THREE

EXPERIMENTAL PROCEDURE

3.1 MATERIAL PREPARATION

The titanium alloy, IMI 834, used in this investigation was obtained from a section of an experimental 'Spey Data Base Compressor Disc' of rectilinear shape provided by Rolls-Royce. The following heat treatment process was carried out at Rolls-Royce: In order to obtain a duplex microstructure, the disc was $\alpha+\beta$ solution treated at 1030°C (below the β-transus temperature of 1045°C, Table 2.1B) for two hours. The disc was oil quenched from the solution treatment temperature to give a fine grained, Widmanstätten-like microstructure in the transformed-β. Subsequent ageing at 700°C for two hours relieved stresses induced in the oil quenching and thus strengthened the microstructure. After ageing, the disc was air cooled to room temperature.

3.1.1 Test Specimens

Metal fatigue has been investigated under a wide variety of testing conditions. The options considered in the current investigation were tensile, torsional, three point bend and four point bend fatigue testing using un-notched specimens. Four point bend testing was chosen to observe the fatigue damage accumulation in IMI 834 for many reasons. The flat surface of a bend specimen (three or four point) can be polished more easily for detailed observations of the damage accumulation on the fatigue surface, than the concave or circular surface of tension or torsional type specimens. Only one surface is subject to tensile fatigue damage in bend testing and therefore just one surface requires polishing. At least two surfaces need to be polished and observed in tension specimens and the whole gauge length of torsion specimens

must be polished in order to satisfactorily observe the effects of fatigue testing. In addition, because of the respective specimen geometries, the sectioning of bend test specimens for back-thinned foil (section 3.3.5.2) and cross-sectional (section 3.3.5.3) thin foil observations is much simpler than the sectioning of tension or torsion type specimens. Four point bend test specimens were chosen in preference to three point bend test specimens since a much larger area of the fatigue surface is subjected to the maximum stress during fatigue and thus more foils for transmission electron microscope (T.E.M.) observations may be obtained from each specimen. The four point bend test geometry was also chosen so that preferential yielding, a problem that can occur in three point bending, is less likely to occur.

Four point bend test specimens of 10.0 x 10.0 x 80.0 mm were accurately machined at Rolls-Royce from the radially and tangentially orientated locations in the disc section, which are illustrated in Figure 3.1A to 3.1F. All specimens were labelled on immediate removal from the disc in order to define their exact position and orientation within the disc. A fine ultrasonic drill was used for this purpose to give a permanent marking on each specimen. The position and orientation of radial specimens were identified by marking the 10.0 x 10.0 mm end closest to the disc bore with a number (Figure 3.2A). For example, the number OR6B corresponds to an outer radial specimen in layer B at position 6. The position and orientation of tangential specimens were defined by marking the 10.0 x 80.0 mm surface facing towards the disc bore with a small circle close to one end and marking the adjacent 10 x 10 mm end with a number, see Figure 3.2B. A metallographic specimen, M1, of approximately 15 x 20 x 50 mm was cut from the centre of the disc section and used for observations of the unfatigued material.

In a compressor disc, the area subjected to the greatest fatigue stresses during in-service conditions is the area

closest to the bore of the disc. High hoop stresses act in this region which can cause cracks to initiate at the bore, which then propagate radially into the disc. In order to obtain the conditions closest to those in service, the specimens chosen for fatigue testing were orientated tangentially. The surface of maximum stress in these specimens faces towards the disc bore and corresponds to a 10.0 x 35.0 mm area in the centre of the 10.0 x 80.0 mm surface, see Figure 3.3, which is defined by the position of the inner rollers. This is explained further in section 3.2.2. The 10.0 x 80.0 mm surface which faces the disc bore in tangential specimens will be referred to as the 'fatigue surface' throughout this thesis.

3.1.2 Specimen Polishing

An important stage in the preparation of the test specimens was to obtain a flat, polished fatigue surface of which the microstructure could be distinguished under both the optical and scanning electron microscopes. The fatigue surface was ground flat on 1200 grit paper to remove any scratches and surface damage resulting from the extraction of the specimen from the compressor disc. A Struers lapping wheel was used at a speed of 40 rpm to polish two specimens at a time using 6 μm and then 1 μm diamond pastes. A solution of 1 part colloidal silica (Silco of 0.05 μm diameter) to 10 parts water was then used to obtain a smooth fatigue surface by hand polishing at 250 rpm on a Struers O.P. polishing cloth.

After polishing, the specimens were lavishly coated with a lacquer resin over all but an area of 10.0 x 40 mm across the centre of the fatigue surface and an adjacent 2 x 40 mm on the sides of the specimens. The remaining, unprotected area was electropolished; (i) to 'round' the corners and thus reduce the tendency for specimens to initiate fatal cracks at the corners and (ii) to remove any residual surface deformation from the polishing

process. Electrical contact with the specimen was made by carefully scratching enough lacquer resin from one end of the specimen to attach a large crocodile clip (anode). The specimen was then carefully lowered into a steel beaker (cathode) containing 500 ml of 5% perchloric acid, 35% 2-butoxyethanol and 60% methanol, so that the unprotected area to be electropolished was completely submerged. The solution was magnetically stirred and cooled to a temperature of < -55°C using liquid nitrogen. This temperature was maintained by placing the beaker in a plastic container with methanol cooled with liquid nitrogen. Successful results were obtained on electropolishing at a voltage of 54 V and current of 60 to 80 mA for two minutes. The specimens were thoroughly washed in methanol before removing the lacquer.

3.2 MECHANICAL TESTING

3.2.1 Tensile Testing

An important parameter required for carrying out fatigue testing is the 0.2% proof stress (P.S.) of the material. This was determined for specimens in both the tangential and radial directions by testing five standard tensile test specimens which were machined from 10.0 x 10.0 x 80.0 mm specimens. The diameter of the tensile specimens was 3.99 $\pm$ 0.01 mm and the gauge length was 25 mm. Tensile testing was carried out using a Mayes Servohydraulic testing machine with an extension rate of 0.06 mm/minute.

The five tensile test specimens were chosen from strategic locations in the disc section (see Figure 3.1). Specimens TC13 from the disc rim, TC7 from close to the centre of the section and TD1 from close to the disc bore, were used to determine the proof stress in the tangential direction and specimens OR11B and IR5B were used to determine the proof stress in the radial direction.

3.2.2 Four Point Bend Fatigue Testing

A Mand servohydraulic testing machine was used to carry out load controlled, low cycle fatigue (LCF) tests in the form of cyclic four point bending. The tests were carried out at room temperature, with a frequency of 5 Hz and an R ratio ($\sigma_{min}/\sigma_{max}$) of 0.1. A four point bend rig was supplied by Mayes for the purpose of this investigation. Figure 3.4 illustrates the stress profile across the 80.0 mm specimen length. The specimen geometry was chosen so that the maximum load was well within the maximum load capability of the testing machine when fitted with a 25 kN load cell. Figure 3.5 illustrates the four point bending configuration; the two outer rollers were positioned on the fatigue surface 70.0 mm apart and 5.0 mm from each end of the specimen, and the position of the inner rollers was half way between the specimen centre and the outer rollers on the opposite surface *i.e.* 17.5 mm from the centre of the specimen. The maximum and mean loads (F_{max} and F_{mean} respectively) to subject a tangential specimen to A% of its 0.2% P.S. (where A = 80 to 100) were calculated for each specimen tested using simple bending theory [133]. The derivations of the following formulae for F_{max} and F_{mean} are given in Appendix 2:

$$F_{max} = 0.1905\sigma_{ps}bd^2A \qquad (3.1)$$

$$F_{mean} = 0.0857\sigma_{ps}bd^2A \qquad (3.2)$$

where:

σ_{ps} = 0.2% Proof Stress (N/m²)
b = average specimen breadth (m)
d = average specimen depth (m)
A = percent of 0.2% P.S.
F_{max} and F_{mean} have units of Newtons (N)

The specimen breadths and depths were determined by averaging at with least four micrometer readings. Table 3.1 lists the value of A, average depth and breadth, F_{max}

and F_{mean} for each tangential specimen tested. All the fatigue tests were carried out to failure at a maximum stress of A = 80% to 100% of the calculated 0.2% P.S. Testing was monitored using a graduated optical telescope focussed on a mirror orientated at 45° to the specimen surface.

Two radial specimens (OR6B and OR9B, see Figure 3.1) were fatigue tested at A = 80% before any tangential specimens were tested, using the 0.2% P.S. calculated for the radial specimens. These initial tests were carried out to provide an indication of the four point bend fatigue lifetime at this stress level.

3.3 MICROSTRUCTURAL EXAMINATION

3.3.1 Composition

The composition of IMI 834 was determined from 0.5 g sections taken from specimen M1 (Figure 3.1). The elements; carbon, oxygen and nitrogen were measured using LECO. The percentage of the remaining elements were determined by ICP.

3.3.2 X-ray Diffraction

X-ray diffraction was carried out using cobalt radiation (wavelength 0.179021 nm) between 2θ = 35° and 2θ = 100°. Scanning rates of 1°/min and 0.5°/min were used. A surface from specimen M1 was polished and lightly etched for 10 seconds in a solution of 2% HF, 8% HNO_3 and 90% H_2O for the determination of α- and β-titanium lattice parameters and d spacings.

The three orthogonal surfaces of a cube of material cut from one end of specimen TA3 (after fatigue failure) were polished and scanned from 2θ = 40° to 100°. A suggestion of the preferred texture close to the disc bore was

obtained by comparing the ratios of the peak intensities in the resulting X-ray traces, notably the intensity of the $(0002)_\alpha$ peak.

3.3.3 Optical Microscopy

Unfatigued specimens for optical microscopy were ground and polished using 6 μm and 1 μm diamond pastes. Colloidal silica (Silco of 0.05 μm diameter) was used for the final polish. The specimens were etched in 2% HF, 8% HNO_3 and 90% H_2O for 20 to 30 seconds. The volume fraction of primary-α was determined by identifying the phase (primary-α or transformed-β) at 3000 points on each of the three orthogonal surfaces of a cube cut from specimen TA3 (see section 3.3.2). The 95% confidence limits, $2\sigma_v$, were calculated from the equation;

$$\sigma_v = \frac{(V\%\ \alpha\ (1-\ V\%\ \alpha))^{1/2}}{(No.\alpha)^{1/2}} \qquad (3.3)$$

where:

No.α = the number of points counted in the primary-α phase

V% α = the volume fraction of primary-α

σ_v = the standard deviation.

Optical microscopy provides a quick and useful technique for observing the fatigue surfaces of failed specimens. These surfaces were observed under both reflected light and Nomarski interference conditions.

3.3.4 Scanning Electron Microscopy (S.E.M.)

Sections were cut from failed specimens at a distance of approximately 3 mm from the fracture surface using a slow speed, 0.5 mm silicon carbide slitting wheel. The sections were mounted using silver dag in order to observe the fracture surface in a Camscan series 2 S.E.M.

A section of the fatigue surface (see Figure 3.5) from a

specimen tested at 100% P.S. was carefully removed after etching for 20 seconds in 2% HF, 8% HNO_3 and 90% H_2O. The fatigue surface section was then placed in the S.E.M. to examine the distribution of slip bands and secondary cracking.

3.3.5 Transmission Electron Microscopy (T.E.M.)

The majority of T.E.M. was carried out on a Jeol 200CX electron microscope operating at 200 kV. A Philips 400T electron microscope was also used, operating at 100 kV.

3.3.5.1 Foil Preparation from Unfatigued Material

In order to characterise the microstructure of unfatigued IMI 834, thin foils were electropolished. To observe and determine the effect of fatigue on the microstructure of the alloy, it was initially necessary to determine the unfatigued foil microstructure in terms of the identification and distribution of phases and the nature and distribution of dislocations present.

Rods of IMI 834 3.0 mm in diameter were machined from unfatigued specimens (M1 and TE1, see Figure 3.1) using a sharp lathe at slow speeds and using water as a coolant. The rods were sectioned into approximately 0.5 mm thick discs using a 0.5 mm silicon carbide slitting wheel. A low speed of 200 to 300 rpm was used to keep deformation as a result of the preparation to a minimum. The discs were carefully ground from both sides on 1200 grit paper to a thickness of 200 μm. Electropolishing was carried out at 90 V and 22 mA using a Struers Tenupol-2 electropolisher. A solution of 5% perchloric acid, 35% 2-butoxyethanol and 60% methanol, cooled with liquid nitrogen was used at a temperature of approximately -55°C. All foils were cleaned twice in methanol before observation in the T.E.M.

3.3.5.2 Back-thinned Foil Preparation

Back-thinned foils were prepared from fatigued specimens in order to observe the dislocation structures induced by fatigue testing at a position which was parallel to the fatigue surface and, ideally, at the fatigue surface. Slices of 0.5 mm thick x 4 mm x 10.0 mm were carefully cut from the 35.0 x 10.0 mm area of maximum stress in specimens which had been fatigue tested at 95% and 100% of the 0.2% P.S. A silicon carbide slitting wheel was used at low speeds with water as a coolant. The slices were mounted using low melting point wax on a clean glass plate with the fatigue surface facing downwards, and then thinned to a thickness of 200 μm using 1200 grit paper. After removal from the glass plate, any excess low melting point wax was cleaned from the thin slice by ultrasonic agitation in methanol. Three discs of 3 mm diameter were punched from each slice (ensuring that the fatigue surface was facing downwards before punching). An attempt to spark erode 3 mm discs in deionised water proved unsuccessful. The fatigue surface of each disc was covered with a lacquer resin and left to dry before the discs were electropolished from the unprotected side (back-thinned) using the same conditions as for unfatigued foil preparation (section 3.3.5.1).

Attempts to obtain back-thinned foils with a thin area at the fatigue surface were unsuccessful. A more successful technique employed an average total electropolishing time which was calculated from back-thinning to perforation at least three 200 μm thick unfatigued foils. A fatigued foil was subsequently back-thinned for at least 90% of the total electropolishing time. The lacquer was removed and the remainder of the foil was thinned from both sides to perforation. The total electropolishing time varied between 240 and 300 seconds and depended upon the conditions, notably temperature, but also solution concentration and flow rate. A variation in the depth of the thin areas below the fatigue surface was expected from

this technique.

3.3.5.3 Cross-sectional Foil Preparation

Figure 3.6 summarises the technique devised for T.E.M. examination of damage accumulation in cross-section below the fatigue surface, based on the methods by Goodhew [185] and Newcombe *et al*. [186, 187].

Sections of > 2.5 x 10.0 x 0.5 mm from failed specimens were cut from within the 35.0 x 10.0 mm area of maximum stress by the method described in section 3.3.5.2 (see Figure 3.6A). To avoid areas which contained plastic deformation due to fatal crack propagation, the sections were cut at a distance of greater than 3 mm away from the fracture surfaces. The sections were carefully ground to 2.0 x 10.0 x 0.5 mm by the method described in section 3.3.5.2. Two techniques, (a) and (b), for obtaining thin foils from the sections were devised:

(a) The first technique involved nickel-plating the fatigue surface in order to protect and identify this surface during further preparation, see Figure 3.6A. A lacquer resin was used to cover all but the fatigue surface of a section so that only this surface was available for nickel-plating. A strike coat of Woods nickel (60 g $NiCl_2$, 31 ml HCl and 250 ml H_2O) was electrolytically plated at room temperature for thirty minutes on to the clean fatigue surface using a pure nickel sheet as the anode. A slow deposition rate was used to ensure that a good bond formed between the titanium and nickel plate. After the strike coat had been deposited, a faster deposition rate was obtained using a nickel Watts bath (165 g/l $NiSO_4$, 22.5 g/l $NiCl_2$, 20 g/l HBO_3, 500 ml H_2O and 2 ml H_2O_2), which was magnetically stirred at 60°C. The nickel-plate was allowed to build up to approximately 150 μm in thickness. Excess nickel plating was carefully ground away after the plating process and the lacquer was removed. The

resulting composite was glued into a slit in a 2 mm diameter rod using Araldite. The slit was cut off-centre so that the fatigue surface could be mounted at the rod diameter. The rod, containing the composite, was glued into a tube of internal diameter just greater than 2 mm and outer diameter of 3 mm so that the cut ends were flush with each other and a minimal gap was present between the rod and tube, see Figure 3.6A. The resulting composite was cured for at least 24 hours. The remaining steps in the preparation of cross-sectional foils are described at the end of technique (b) since these steps are common for both techniques (a) and (b).

(b) The second technique required two sections of the same orientation to be glued with their fatigue surfaces facing, see Figure 3.6A. A slit was cut central to a 2 mm diameter rod and the two sections were glued into the rod and tube in a similar manner to that described above (a).

The remaining steps of the preparation, common to both techniques, are illustrated in Figures 3.6B and 3.6C. Discs of > 0.3 mm in thickness were carefully cut from the composite rod using a 0.5 mm silicon carbide cutting wheel at a slow speed. The discs were carefully ground to 200 μm from both sides and then mounted onto a glass plate using low melting point wax. A subsequent stage of preparation (ion-beam milling) required that the thin area was smooth and clean, thus it was necessary at this stage to polish the exposed surface with 6 μm and 1 μm diamond pastes, finishing with colloidal silica. To provide extra support for the disc, a 3 mm diameter slotted copper grid was glued onto the polished surface to leave the fatigue surface(s) visible. The glue was left to cure before the disc was removed from the glass plate.

The disc was dimpled from the unpolished side using 6 μm and 1 μm diamond pastes to a remaining thickness of 80 μm (Figure 3.6C). This thickness was calculated using a travelling microscope by the method described in Appendix

3. It was important to ensure that the dimple was positioned centrally in the disc so that the electron transparent region occurred at the area of interest (the fatigue surface(s)). A final dimple using colloidal silica gave the polished surface required for ion-beam milling.

Ion-beam milling was carried out on a conventional stage of a Gatan Duomill operating at a voltage of 6 kV and gun current of 0.5 mA. The angle of the beams was initially 16° to the surface and a total ion-beam milling time of around 40 hours was required to thin the remaining 80 μm of material. The beam angle was reduced to 11 or 12° on perforation to improve the quality and increase the size of the thin area.

3.3.5.4 Alternative Foil Preparation Techniques

In light of the results obtained from cross-sectional foils prepared using the nickel plating technique (chapter 5), three alternative foil preparation techniques were devised. The techniques were designed to determine the effect of the dimpling and ion-beam milling stages of the cross-sectional foil preparation technique on the appearance of the thin foil microstructure. Unfatigued foils 3 mm in diameter and 200 μm in thickness were used because of their availability. The details of each technique were adapted from those already described (sections 3.3.5.1 to 3.3.5.3). (i) Foils were dimpled to 80 μm thickness remaining and electropolished from both sides to perforation. (ii) Foils were electropolished to 80 μm remaining thickness and ion-beam milled to perforation. (iii) Foils were dimpled to 80 μm remaining thickness and ion-beam milled to perforation.

CHAPTER FOUR

MATERIAL CHARACTERISATION

4.1 COMPOSITION

The composition of IMI 834 used in this investigation was determined to be: 5.81 ± 0.05 wt% Al, 3.78 ± 0.03 wt% Sn, 3.39 ± 0.03 wt% Zr, 0.70 ± 0.02 wt% Nb, 0.45 ± 0.02 wt% Mo, 0.32 ± 0.02 wt% Si and < 0.02 wt% Fe, the balance being titanium and the interstitial elements O, N and C. The interstitial content was determined to be 0.058 ± 0.001 wt% C, 885 ± 25 ppm O and 23 ± 1 ppm N. The hydrogen content of the material was not determined.

4.2 OPTICAL MICROSCOPY

Optical micrographs of the duplex microstructure of IMI 834 are shown in Figures 4.1A and 4.1B. These clearly show the fine, acicular α-platelets which are arranged in colonies of similarly orientated platelets. Several colonies exist within each transformed-β grain. The average transformed-β grain size of the material was determined to be 66.4 ± 30.4 μm and the average colony size was determined as 35.3 ± 16.5 μm. The prior-β grain boundaries are outlined by a thin layer of α phase and by elongated primary-α grains which occur at triple points. These have an average length determined to be 35.2 ± 9.3 μm and average width determined as 17.9 ± 4.5 μm which occur at triple points (aspect ratio 2:1).

Table 4.1 summarises the data used to determine the volume fraction of the primary-α phase within a specimen taken from the centre of the compressor disc. A volume fraction of 18.8 ± 1.9% primary-α was determined by point counting (see section 3.3.3).

4.3 X-RAY DIFFRACTION

4.3.1 Phase Identification

An X-ray diffraction trace acquired from a polished and lightly etched sample of IMI 834 is shown in Figure 4.2. The reflections in the trace arise from the different planes present in the α phase. Their {hkil} indices have been assigned. The planes are listed in Table 4.2 along with their corresponding d spacings. The calculated lattice parameters for the α-phase have been determined to be $\underline{a}$ = 0.2951 nm and $\underline{c}$ = 0.4686 nm which gives a $\underline{c}/\underline{a}$ ratio of 1.588. Reflections from the retained-β phase are also identified in this trace, but since the volume fraction of retained-β is small, the peaks are of low intensity. Accurate d spacings from the retained-β phase were obtained by using a slower scanning rate over the relevant ranges of 2θ, see Figure 4.3. The peak at 2θ = 45.65° corresponded to a $\{011\}_\beta$ type reflection and that at 2θ = 66.55° nm corresponded to the $\{002\}_\beta$ reflection. From these peaks, the lattice parameter of the retained-β was calculated to be $\underline{a}$ = 0.326 nm. Table 4.3 lists the planes and d spacings for the retained-β phase using this value of the lattice parameter.

4.3.2 Texture Determination

Figure 4.4A shows optical micrographs taken from the three orthogonal surfaces of a tangential four point bend specimen. The surfaces are identified as the fatigue surface, fracture surface and axial surface according to Figure 4.4B which indicates the position of these surfaces in relation to the compressor disc geometry. The primary-α grains in the fatigue and fracture surfaces have a higher aspect ratio (approximately 1:2) than in the axial surface (approximately 1:1). This suggests that the compressor disc has a preferred texture.

X-ray traces from the three orthogonal surfaces were obtained from polished and lightly etched specimens and are illustrated for comparison in Figure 4.5. The relative intensities of the α-phase reflections were calculated, based on the most intense reflection ($\{10\bar{1}1\}_\alpha$) being set to 100 in each case (see Table 4.4). The $\{0002\}_\alpha$ peaks provide a broad indication of the texture present in the disc. Relative $\{0002\}_\alpha$ peak intensities of 18.8, 15 and 4.8 were obtained from the fracture, fatigue and axial surfaces, respectively. A comparison of the $\{0004\}_\alpha$ intensities shows a similar trend. These results indicate that a greater number of basal planes are parallel to the fatigue and fracture surfaces than are parallel to the axial surface. Based on these results, a schematic diagram illustrating the preferred texture in the compressor disc is given in Figure 4.6.

The $(011)_\beta$ peak was only identified in the trace obtained from the fracture surface. This surface also yielded the most intense $(0002)_\alpha$ reflection (see Figure 4.5 and Table 4.4). This observation suggests that the orientation relationship $\{011\}_\beta//(0001)_\alpha$ (equation 2.1) reported by Williams [36] is present in this alloy.

4.4 THIN FOIL MICROSTRUCTURE

4.4.1 Transformed-β grains

Figure 4.7 shows the arrangement of α-platelets in adjacent colonies within a transformed-β grain. The α-platelet boundaries within a colony contain the retained-β phase which appears dark and discontinuous along the length of the boundaries, Figure 4.8.

Figure 4.9A is a higher magnification micrograph of an area showing the retained-β phase along α-platelet boundaries in two adjacent colonies. The retained-β phase

is present as angular, discontinuous particles of 0.1 to 0.5 μm in width. Figure 4.9B is a corresponding dark field micrograph taken using the $(011)_\beta$ spot in the diffraction pattern, Figure 4.9C. Diffraction pattern analysis of the retained-β particles was difficult, due to their small size. However, the lattice parameter for the retained-β phase obtained from diffraction patterns agrees well with the X-ray diffraction data given in Table 4.3.

Small particles of 0.05 to 0.3 μm in length such as those illustrated in Figure 4.10 were found along the α-platelet and transformed-β grain/colony boundaries, within the retained-β phase and occasionally on dislocations within α-platelets. Figure 4.11A is a dark field micrograph of an area containing a large number of particles within an α-platelet. From the analysis of diffraction patterns, such as those in Figures 4.11B and 4.12, the particles were identified as titanium-zirconium silicides. Table 4.5 lists the d spacings obtained from the analysis. The lattice parameters of the silicides were calculated: $\underline{a}$ = 0.703 ± 0.004 nm and $\underline{c}$ = 0.360 ± 0.015 nm. An orientation relationship between the silicides, s, and the α phase was established from the diffraction pattern in Figure 4.12A:

$$[01\bar{1}1]_\alpha // [\bar{2}110]_s;$$
$$(\bar{2}110)_\alpha // (01\bar{1}0)_s \qquad (4.1)$$

Complex interactions between silicide particles, retained-β and dislocations, such as those in Figure 4.13, were observed in the transformed-β grains when α-platelet boundaries occurred in the plane of the foil plane.

The density of dislocations observed in the α-platelets of unfatigued foils varied between colonies. Some colonies were relatively dislocation free and only contained dislocations along the α-platelet boundaries which were associated with the retained-β. In most

colonies, however, the dislocation density was relatively high, as illustrated in Figure 4.14. Dislocations with a c-component in the Burgers vector (c-component dislocations) as well as a type (perfect) dislocations were identified. The density of dislocations was generally higher in regions closer to the α-platelet boundaries and lower near the centre of an α-platelet. Under certain conditions, parallel fringes were observed in some α-platelets, see Figure 4.15. A close inspection of the fringes revealed that they were bounded by c-component dislocations. The fringes were identified as stacking faults and the bounding dislocations were identified as partial dislocations (see section 7.1.2.4).

A few dislocations in some of the platelets, Figure 4.16, appeared straight and perpendicular to g under the condition g = [0002]. These were identified, by their absence under g = [11$\bar{2}$0] (see Appendix 1), as dislocations with Burgers vectors of the type <0001>. Figure 4.16 also shows some small particles on these dislocations which were identified by electron diffraction as silicide particles.

The presence of the ordered phase, Ti_3Al, was established by the presence of reflections in diffraction patterns at half the distance of reflections from the α phase (see section 2.2.5.1). Ti_3Al reflections of very low intensity were detected in some transformed-β grains which suggested that a small amount of this phase was present. However, in the majority of transformed-β grains the presence of Ti_3Al was not detected.

4.4.2 Primary-α grains

Primary-α grains in thin foils from unfatigued IMI 834 contained a dislocation density which varied from grain to grain. Most grains contained only a few dislocations, see Figure 4.17. This was confirmed by tilting these grains under appropriate two beam conditions. Single

dislocations or bands of dislocations present had Burgers vectors ($\underline{b}$) of the type $1/3\langle 11\bar{2}0\rangle$. Some primary-α grains contained hexagonal dislocation arrays such as that illustrated in Figure 4.18. By tilting the grain, it was clear that such arrays of dislocations separated two primary-α sub-grains with a low misorientation. In a few, randomly distributed primary-α grains a much higher dislocation density was present in the form of dislocation networks such as those in Figures 4.19 to 4.21. The dark field micrograph, Figure 4.19 shows that these networks occurred in sub-grains within the primary-α phase. Diffraction analysis and trace analysis of the dislocations revealed that they were $\langle \underline{a} \rangle$ type screw dislocations ($\underline{b} = 1/3\langle 11\bar{2}0\rangle$) which lay on either a prism or pyramidal plane. However, accurate trace analysis was difficult due to the large variation in θ (the angle between the dislocation and the $\underline{g}$ vector), see Figures 4.20 and 4.21.

Figures 4.22A to 4.22C are diffraction patterns taken from zone axes in primary-α grains showing additional reflections which correspond to the presence of the ordered phase, Ti_3Al (see section 2.2.5.1). The zones are: (A) $[1\bar{2}10]$, (B) $[2\bar{4}23]$ and (C) [0001]. The Ti_3Al reflections are more intense than those obtained from transformed-β grains (using the same selected area aperture size) and were observed in all the primary-α grains analysed. However, the relative intensities of the reflections varied, suggesting that the amount of Ti_3Al may vary between primary-α grains. Figure 4.22D is a bright field T.E.M. micrograph of the bend centre from which diffraction pattern C was taken.

CHAPTER FIVE

THE INTERFACE PHASE

5.1 CROSS-SECTIONAL THIN FOILS

Cross-sectional thin foils of a fatigue surface were prepared from specimens which had been nickel-plated using the technique described in section 3.3.5.3. Figure 5.1 is a low magnification T.E.M. micrograph showing the extent of the thin area obtained with respect to the fatigue (nickel-plated) surface. Figure 5.2 is an example of the microstructure which was typical of that observed at about 100 μm from the fatigue surface. Much of the transformed-β microstructure had been changed dramatically making the original microstructure barely identifiable. α-platelet boundaries, two of which are identified in Figure 5.2, appear to have been transformed either as a result of fatigue damage or thin foil preparation techniques. Parallel streaks which crossed the α-platelets in several directions are also present in this region. Figure 5.3A is a dark field micrograph of a similar α-platelet boundary (observed at about 100 μm from the fatigue surface) which clearly shows that a phase has formed in the boundary region that is distinct from the retained-β and α-platelet phases of titanium. The diffraction pattern containing the reflection from which the dark field micrograph (Figure 5.3A) was imaged is given in Figure 5.3B.

Figures 5.4A to 5.4D are examples of the microstructure in regions of the transformed-β phase at approximately 150 μm from the fatigue surface. The features present are similar to those seen closer to the surface (Figures 5.2 and 5.3A) but are more clearly defined. A phase is observed which had formed along the interface of the retained-β phase and α-platelets, the width of which varies between 0.1 and 0.5 μm. Acicular features or

bands, between 0.02 and 0.2 μm wide, also formed across the α-platelets. These features crossed the α-platelets parallel to each other in several directions (Figure 5.4B), suggesting that they had occurred in very strict crystallographic directions. The majority of the bands crossed the α-platelet width. Figure 5.5A and 5.5B are bright and dark field micrographs highlighting both the phase along the α-platelet boundaries and the acicular features occurring across the α-platelets. A thin layer of retained-β phase is resolvable at the centre of one of the α-platelet boundaries in Figure 5.5B.

The density of acicular bands decreased on moving further from the surface (> 150 μm) and none were observed at greater than about 250 μm from the surface. However, at > 250 μm, the phase along the α-platelet boundaries was observed in the thin area of the foil.

Limited thin areas were obtained from two other cross-sectional foils prepared by the same technique. Similar features to those seen in Figures 5.2 and 5.3 were found at the fatigue surfaces and to a depth of between 100 and 150 μm. Regions containing both phases were found at approximately 150 μm from the fatigue surfaces, although the number of acicular bands observed was not as high as in the first foil described.

It is important to establish the origin(s) of both the phase observed along the α-platelet boundaries and the features observed across the α-platelets. This is discussed in detail in section 5.2.

5.2 EFFECT OF PREPARATION TECHNIQUES

On discovering the phases in the cross-sectional foils described in section 5.1, it was important to establish whether they were wholly or partly artefactual *i.e.* whether they were introduced during foil preparation, or indeed, whether they were the result of fatigue damage.

Thin foils from unfatigued specimens were therefore prepared by the techniques (i), (ii) and (iii), described in section 3.3.5.4 and, in addition, foils from fatigued specimens were prepared by the method of back-thinning (section 3.3.5.2). The foils were examined by T.E.M., with some interesting results. Table 5.1 summarises these results.

No phases along or between α-platelet boundaries were formed in the following: Unfatigued and fatigued foils thinned by electropolishing at < -55°C (section 3.3.5.1), unfatigued foils thinned by dimpling and then electropolishing (technique (i), section 3.3.5.4) or unfatigued and fatigued foils prepared by back-thinning (section 3.3.5.2).

Figures 5.6 and 5.7 show evidence of a phase which had formed along α-platelet boundaries in foils which had been electropolished and then ion-beam milled to perforation (technique (ii)) and dimpled and ion-beam milled to perforation (technique (iii)), respectively. However, in these foils the phase had formed along fewer of the α-platelet boundaries and these were distributed throughout the thin areas of the foils. Acicular features were not found in foils prepared by either technique ((ii) or (iii)).

It appeared from the above results that ion-beam milling induced a phase to form along some of the α-platelet boundaries in the transformed-β microstructure. The phase was not observed in foils which had been prepared by techniques such as electropolishing (section 3.3.5.1). It is suggested that the nickel plating process, used in the preparation of cross-sectional thin foils, caused a similar phase to form along the α-platelet boundaries and a second, acicular feature to form across the width of some of the α-platelets. The microstructure of the cross-sectional foils changed dramatically as the distance from the nickel-plated surface increased such that, within

about 150 μm of the surface the original microstructure was barely identifiable (Figure 5.2). Between about 150 and 250 μm from the surface both the phase along the α-platelet boundaries and the bands across the α-platelets were observed. At greater than 250 μm from the surface, only the phase along the α-platelet boundaries was observed. The results are discussed further in section 7.2.

5.3 CRYSTALLOGRAPHY OF THE PHASES

Analysis of the crystallography of the phases observed in cross-sectional foils was carried out using selected area diffraction patterns and convergent beam electron diffraction with a spot size of approximately 100 nm. Figure 5.8A is a bright field T.E.M. micrograph of an area containing both the phase along the α-platelet boundaries and the acicular features across the α-platelets. The diffraction pattern in Figure 5.8B was obtained by careful tilting of the thin foil. Reflections corresponding to the two phases of interest and to a $[1\bar{2}13]_\alpha$ zone are present in this diffraction pattern. Figure 5.8C is a schematic representation of the diffraction pattern in Figure 5.8B. By selecting each reflection in turn to give a dark field image, it was possible to determine which reflections gave rise to particular features. The results are represented in Figure 5.8C by the use of different symbols for the α phase, the phase along the α-platelet boundaries and the phase across the α-platelets. Selecting the spot marked F in Figure 5.8C gave the dark field micrograph of the boundary phase, Figure 5.8D. The dark field micrograph, Figure 5.8E, was taken using the reflection marked H in Figure 5.8C and highlights the phase across the α-platelets in the same region as Figure 5.8D. The α-platelets appear grey rather than black in Figure 5.8E due to the close proximity of the reflections from the acicular phase and reflections from the α phase. Figure 5.8E indicates that the acicular phase was also present

between the edge of the phase along the α-platelet boundaries and the α-platelets.

Figure 5.9A is a selected area diffraction pattern obtained by tilting a region of the foil containing both the phases of interest to an $[0001]_\alpha$ zone. This is drawn schematically in Figure 5.9B. Also of interest in this diffraction pattern are the presence of reflections from the retained-β phase which correspond to an $[011]_\beta$ zone and agree with the Burgers orientation relationship: $[0001]_\alpha // [011]_\beta$ [36]. Figures 5.10A, 5.10B and 5.10C are convergent beam electron diffraction patterns taken from an area containing the two phases of interest and the α phase, without tilting the foil. These figures show an [0001] zone from the α phase, a zone from the phase along the α-platelet boundaries and reflections from the acicular phase. In both Figures 5.10B and 5.10C, reflections from the α phase are also present as less intense discs. The small size of the additional phases made it impossible to focus the beam on areas which did not contain some α phase.

Determination of the d spacings corresponding to the phase along the α-platelet boundaries from the diffraction patterns in Figures 5.8B and 5.9A, identified this phase to be face centred cubic in structure. The lattice parameter was calculated to be $\underline{a} = 0.434 \pm 0.004$ nm. Table 5.2 lists the corresponding reflections to which the d spacings refer. The phase was determined to be equivalent to the interface phase (IFP) described in the literature (see section 2.2.6, Table 2.3) and will, therefore, subsequently be referred to as the fcc interface phase. Having established the structure of the fcc interface phase, it was possible to index the diffraction patterns with respect to this phase. The fcc phase reflections in Figure 5.8B correspond to a $[112]_{fcc}$ zone and those in Figure 5.9A correspond to a $[001]_{fcc}$ zone. From these diffraction patterns, two orientation relationships, between the α phase and fcc interface

phase, are suggested:

$$[1\bar{2}13]_\alpha // [1\bar{1}2]_{fcc} \; ; \quad (10\bar{1}0)_\alpha // (110)_{fcc} \qquad (5.1)$$

and

$$[011]_\beta // [0001]_\alpha // [001]_{fcc} \; ; \quad (1\bar{1}2)_\beta // (10\bar{1}0)_\alpha // (110)_{fcc} \qquad (5.2)$$

The crystal structure of the acicular phase which occurred across the α-platelets could not be determined conclusively despite much deliberation over results from the diffraction pattern analysis and from high resolution electron microscopy of the phase. The occurrence and identification of both phases are discussed with reference to the literature in section 7.2.

CHAPTER SIX

FATIGUE DAMAGE

6.1 TENSILE TESTS

Table 6.1 lists the results of tensile tests on specimens which were taken from the locations in the compressor disc indicated in Figure 3.1. The ultimate tensile strength (U.T.S.) and 0.2% proof stress (P.S.) were determined for specimens taken from both the tangential and radial orientations. A 0.2% P.S. of 872 MPa was obtained from tangentially orientated specimens which were taken from positions close to the disc bore (TD1 and TC7). A 0.2% P.S. of 880 MPa was obtained from radially orientated specimens. These values for the 0.2% P.S. were used in the determination of F_{max} and F_{mean} (see equations 3.1 and 3.2). Average U.T.S. values of 993 MPa and 1008 MPa were obtained from the tangentially orientated and radially orientated specimens, respectively. From the gradient of the stress-strain curves, the Young's modulus, $E_{average}$, was calculated to be 117 GPa.

6.2 FATIGUE TESTS

Two radial specimens (OR6B and OR9B) which had not been electropolished were tested at a maximum stress (σ_{max}) of 80% P.S. in order to obtain an estimate of the fatigue lifetime at this stress level. The specimens failed after 75230 and 90260 cycles respectively. The fatal cracks had initiated from a corner of the surface of maximum stress (see Figure 3.3). Optical and S.E.M. observations close to the crack origin on both specimens did not reveal any information on the cause of failure. To reduce the undesirable tendency for specimens to fail at the corners, all subsequent fatigue tests were carried out on specimens which had been electropolished as described in section 3.5.1.

Table 6.2 lists the number of cycles to failure, N_f, of tangentially orientated specimens which were tested at a maximum stress level of between 80% and 100% P.S. The fatigue lifetimes are plotted as a stress versus number of cycles (S-N) curve in Figure 6.1. As expected, an increase in the number of cycles to failure with a decrease in the maximum stress level was observed. Specimen TA1 tested at 80% P.S. did not fail after 126880 cycles.

6.3 FATIGUE SURFACES

The majority of fatigue surface observations were carried out using optical microscopy. Observations were also made using scanning electron microscopy (S.E.M.).

6.3.1 Slip Bands

Optical microscopy of the fatigue surfaces revealed that slip bands had occurred during fatigue testing in favourably orientated primary-α and transformed-β grains present in the area of maximum stress in all failed specimens. Figure 6.2 is an optical micrograph taken from a specimen which had been fatigue tested at 100% P.S. which shows slip bands within primary-α grains. The slip occurred across the widths of the grains as individual or parallel bands. The orientation of these bands was observed to have occurred between 40° and 90° to the applied stress direction. Only in the more highly stressed areas, such as those adjacent to the fatal cracks (fracture surfaces), were slip bands observed in more than one direction in a given grain. Slip within the transformed-β was less commonly observed and positive identification was difficult because slip bands were obscured by the α-platelet structure of the transformed-β grains. Thus an estimate of the slip band distribution in the transformed-β could not be made by optical or scanning electron microscopy. In transformed-β grains where the

slip bands could be identified, the slip was found to occur at 60° or 90° to the direction of the α-platelets. Figure 6.3 is an example of the fatigued microstructure typical of that observed across the fatigue surface in a specimen tested at 100% P.S., and clearly shows that the slip bands were more easily identifiable in the primary-α grains than in the transformed-β grains.

The density of slip bands is a function of the applied stress. In a specimen tested at 100% P.S., slip bands were observed in favourably orientated primary-α grains across the entire fatigue surface. As the maximum stress level was reduced, the number of primary-α grains containing slip bands also reduced and the average number of slip bands within those grains was also lower. A higher slip band concentration close to the fatal fatigue crack in all specimens was due to the large plastic zones present, and higher stresses imposed, during long-crack propagation.

6.3.2 Secondary Cracking

Secondary cracks (*i.e.* cracks which did not propagate to cause failure) were observed on the fatigue surfaces of all the specimens tested. An increase in the number of secondary cracks was observed with increasing maximum stress. For example 20 secondary cracks were found in a specimen tested at 85% P.S., between 60 and 80 secondary cracks were observed in specimens tested at 95% P.S. and close to 100 secondary cracks were observed in a specimen tested at 100% P.S.

6.3.2.1 Secondary Crack Initiation

Figures 6.4A and 6.4B are examples of secondary cracks which were observed in a specimen tested at 100% P.S. The cracks initiated within primary-α grains in a direction which was parallel to the slip bands present suggesting that the cracks had occurred along slip bands.

The majority of secondary cracks in all fractured specimens were greater than one primary-α grain diameter (35 μm) in length. In many of the shorter secondary cracks (< 200 μm), such as those in Figures 6.5 and 6.6, it was possible to determine the probable crack initiation site as a primary-α grain which occurred approximately at the middle of the secondary crack length. The orientation of the secondary cracks in the initiating primary-α grains was between 50° and 90° to the applied stress direction. Only occasionally were cracks observed which had initiated from colonies in the transformed-β grains. The initiation of many secondary cracks, however, could not be positively identified, particularly as some cracks may have initiated in sub-surface grains.

6.3.2.2 Secondary Crack Propagation

The majority of secondary cracks of over 200 μm in length, such as those in Figures 6.7A and 6.7B, were found to have occurred by the coalescence of two, or more, shorter secondary cracks. The cracking in Figure 6.7A was observed in a specimen tested at 100% P.S. and clearly illustrates the tortuous and bifurcating nature of crack propagation in IMI 834. There was a tendency for the longer cracks to group or cluster, particularly in specimens tested at the higher stress levels (95% and 100% P.S.). For example, Figure 6.7B shows a cluster of cracks in a specimen tested at 95% P.S.

It was found that there was a preference for short cracks to propagate through the transformed-β colonies perpendicular to the α-platelet direction. The short secondary cracks illustrated in Figures 6.4A, 6.4B and 6.5 have propagated in the adjacent transformed-β at 90° to the α-platelet direction in colonies which were suitably orientated with respect to the initial crack and the applied stress direction. Where no suitably orientated colonies were available, the paths of the respective

cracks were more tortuous in nature, or were arrested. For example in Figure 6.5, the α-platelets in a colony on one side of the initiating primary-α grain lie almost parallel to the initial crack direction. It is observed that the propagating crack path through this grain is more tortuous than the crack path through the colony on the opposite side of the primary-α grain in which a path perpendicular to the α-platelets is followed. Further examples of a preferred short crack path perpendicular to the direction of α-platelets are illustrated in Figures 6.7A and 6.8. The crack path in Figure 6.8 is particularly interesting and is discussed in detail in the figure caption.

6.3.3 Fatal Fatigue Cracks

Figure 6.9 is a low magnification optical montage taken with Nomarski interference, showing the path of the fatal crack in a specimen tested at 100% P.S. The test was terminated just prior to failure so that the detail of the fatal crack path could be observed. It is possible to identify the region in which the crack initiated by the observation of the surface relief which is associated with the increase in crack tip plasticity with crack propagation. The surface relief is enhanced by the Nomarski interference conditions used and the region in which the crack initiated is indicated. Similar surface relief associated with the fatal crack propagation was observed on other fractured specimens.

Figures 6.10A and 6.10B are higher magnification montages of the area containing the crack initiation site. Figure 6.10A was taken with Nomarski interference and Figure 6.10B was taken after the fatigue surface had been etched to reveal the microstructure. In Figure 6.10B, two primary-α grains are indicated where the fatal crack passes parallel to slip bands contained within them. It is possible that one of these grains initiated the fatal crack, but without more substantial evidence it is equally

possible that the crack initiated in an adjacent transformed-β grain, a sub-surface site or even at two sites. In Figure 6.10A slip bands in some transformed-β grains (indicated) can be seen at close to 90° to the applied stress direction. By comparison of the grains with the equivalent grains on the etched surface (Figure 6.10B), it is clear that the slip bands occur at either 60° or 90° to the direction of the α-platelets.

Figure 6.11 is a high magnification montage of the two complementary fatigue surfaces of the area containing the origin of the fatal fatigue crack in a specimen fatigued to failure at 90% P.S. Prior to the propagating crack becoming more tortuous in nature, the crack traverses at least three primary-α grains maintaining a direction parallel to the slip bands contained within them (at 60° and 70° to the stress direction). The initiation site was identified by S.E.M. as the primary-α grain indicated (see section 6.4.1 below).

6.4 FRACTURE SURFACES

6.4.1 Crack origins

Figure 6.12 compares the fatigue and fracture surfaces of one half of a fractured specimen tested at 90% P.S. (the same specimen as that shown in Figure 6.11 in section 6.3.3). By using the river markings on the fracture surface as a guide, the origin of the crack was traced to a primary-α grain at the fatigue surface. The diameter of the primary-α grain on the fatigue surface was approximately 20 μm. This figure also shows a crack branch at the primary-α/transformed-β grain boundary.

In the S.E.M. micrograph of the fracture surface in Figure 6.12, a small elliptical-shaped feature of approximately 2 μm in diameter was observed at 2 to 3 μm from the fatigue surface in the initiating primary-α grain. An attempt to analyse the composition of this feature by energy

dispersive spectroscopy (EDS) in the S.E.M. found no difference in composition between this feature and the adjacent primary-α phase. The feature was surrounded by a very smooth area of approximately 5 μm in radius from which the river markings extended radially. This featureless area suggests that the fatal crack had initiated crystallographically along a slip band within the primary-α grain without any deviation in the plane of the crack path. It is interesting to note that the river markings in the initiating primary-α grain extend up to 50 μm below the fatigue surface and cross at least one boundary between two primary-α grains. It is considered that such low misorientation boundaries can effectively double the length over which damage can accumulate on a given slip band and may influence the mechanism of fatigue crack initiation (see section 7.5).

Figures 6.13A and 6.13B show the two complementary fracture surfaces in a specimen tested at 95% P.S. The crack origin occurred at approximately 20 μm below the surface of the test specimen. The features associated with this origin were similar to those observed in a specimen tested at 90% P.S. (Figure 6.12), suggesting that the initiation site was also a primary-α grain. The changes in contrast which can be seen in Figure 6.13A correspond to the boundaries between the initiating primary-α grain (darker) and adjacent primary-α grains of slightly different orientation. A feature of about 2 to 3 μm in diameter was observed on one fracture surface of the initiating grain, close to the boundary with an adjacent transformed-β grain. This feature is similar in appearance to the elliptical feature present in Figure 6.12. A comparison between the two complementary fracture surfaces shows that the feature was elevated on one surface and depressed on the other surface.

6.4.2 Crack Propagation

When the fracture surfaces of all failed specimens were

observed by eye under bright light, the region in which the fatal crack had initiated appeared as a shiny region of up to 3 millimetres in radius. The remainder of the fracture surface had a more matt appearance. This macroscopically visible transition in fracture appearance was investigated by S.E.M.

Figure 6.14 is a S.E.M. montage taken near to the fatal crack origin of a specimen tested at 95% P.S. The extensive facetting observed in this area is similar to that observed around the crack origins of all the specimens and suggests that a quasi-cleavage (cleavage-like) mode of fracture operates close to the crack origins. The facets occur on the scale of the primary-α grain/transformed-β colony size and contain river markings similar to those illustrated in Figures 6.12 and 6.13. It is considered that the majority of the facets arise from cleavage of the primary-α phase. The remainder of the fracture surface appears blocky in nature and is likely to arise from the transformed-β phase. Material which has fractured in layers on the scale of α-platelet widths can clearly be seen in these blocky regions.

Figures 6.15A to 6.15C were taken from areas greater than 3 mm from the fatal crack origins, *i.e.* beyond the transition in fractographic appearance, of various test specimens. The more ductile appearance of these areas shows features such as flutes and micro-serrated ridges [188]. Figures 6.15A and 6.15B show regions of fluting up to 60 μm in length which are typical of the post-transition fracture surfaces. The micro-serrated ridges in Figure 6.15C are approximately 0.5 μm apart which suggests that these arise from a transformed-β colony which has been fractured perpendicular to the α-platelets contained within it. No evidence of any fatigue striations on these post-transition fracture surfaces was found.

An estimate of the alternating stress intensity factor, ΔK ($MPam^{1/2}$), at which the macroscopically visible transition in fracture appearance is observed, was calculated from (equation 2.9 [130, 132, 133]):

$$\Delta K = Y\Delta\sigma(\pi a)^{1/2} \qquad (6.1)$$

where:

- a = crack depth at the transition (m)
- Y = specimen geometry and loading system factor
- $\Delta\sigma$ = the stress range at the crack depth (MPa), a, below the fatigue surface

The crack depth, a, was measured from the projected crack length below the fatigue surface, perpendicular to the applied stress axis using a travelling microscope. A value of Y = 1 for four point bend testing was used as this corresponds to a crack which had initiated from an infinite surface and also since no alternative values of Y for four point bend test specimen geometries have been suggested [189]. The value of $\Delta\sigma$ (MPa) was calculated according to the following equation:

$$\Delta\sigma = (\sigma_{max} - \sigma_{min})(y-a)/y \qquad (6.2)$$

where:

- σ_{max} = maximum stress at the fatigue surface (MPa)
- σ_{min} = $\sigma_{max}/10$ since R = 0.1
- y = 5 mm *i.e.* the specimen centre line depth or depth of the neutral axis from the fatigue surface, see Appendix 2 (m)
- a = crack depth at the transition (m)

The data measured from specimens which had failed with a crack that had initiated from a non-corner site are given in Table 6.3. Average ΔK values measured at the change in fractographic appearance for the different stress levels are 32.7 $MPam^{1/2}$ at σ_{max} = 95% P.S., 32.0 $MPam^{1/2}$ at σ_{max} = 90% P.S. and 31.6 $MPam^{1/2}$ at σ_{max} = 85% P.S. These

results are discussed in section 7.3.3. with reference to the reverse plastic zone size of the material.

6.5 THIN FOIL OBSERVATIONS

Thin foils from specimens fatigued to failure were prepared by two techniques: (i) Back-thinning (see section 3.3.5.2). (ii) By cross-sectional thin foil preparation (see section 3.3.5.3). All the foil sections were taken from the 35.0 x 10.0 mm area of maximum stress at a distance of at least 3 mm from the fracture surface of specimens which had been fatigued at 95% P.S. or 100% P.S.

6.5.1 Foil Preparation Results

6.5.1.1 Back-thinned Foils

The most successful back-thinned foils were obtained from 200 μm thick discs which had been back-thinned for at least 90% of the total electropolishing time and then electropolished from both sides to perforation (see section 3.3.5.2). It was observed that the variation in total electropolishing time, resulted in the electron transparent region of the foil occurring at between 5 and 10 μm from the fatigue surface. The electron transparent areas were far more extensive using this technique than those obtained from back-thinning foils to the fatigue surface.

6.5.1.2 Cross-sectional Thin Foils

Figure 6.16 is a low magnification T.E.M. micrograph showing the extent of the thin area obtained in a cross-sectional foil taken from a fatigued specimen (prepared by technique (b) in section 3.3.5.3). The preparation of the majority of cross-sectional thin foils was successful in that it was possible to identify the position of the fatigue surface in relation to the underlying microstructure and associated fatigue damage.

The presence of the interface phase (see chapter 5) was not detected in any of the cross-sectional foils obtained by this technique.

6.5.2 Slip in Primary-α Grains

Intense parallel planar slip bands were characteristic of fatigue deformation in the primary-α grains, Figure 6.17. In foils which contained relatively extensive thin areas, the slip bands were observed to traverse the length of primary-α grains. The slip bands were arrested at grain boundaries between the primary-α and adjacent transformed-β grains. In cases where two primary-α grains were adjacent to each other, Figure 6.18, the slip bands crossed low angle boundaries with a change in direction corresponding to the misorientation between the grains. In the example given in Figure 6.18, the misorientation between the primary-α grains is approximately 9°. In all the examples found where two adjacent primary-α grains were crossed by slip bands, the misorientation between them was observed to be $\leq$ 10°.

6.5.2.1 Slip in Back-thinned Foils

Figures 6.19A to 6.19C are examples of slip bands in primary-α grains, which were examined in back-thinned foils. The dislocations in the bands have piled up against the boundary between the primary-α and an adjacent transformed-β grain. By measuring the width of the slip band under different beam directions, it was possible to determine on which plane slip had occurred. The boxed region in Figure 6.19B was imaged under the twelve conditions listed in Table 6.4, six of which are shown in Figures 6.20A to 6.20F. The width of the band was measured at each zone and was found to decrease from a maximum at a beam direction, B, close to [0001] to a minimum at B close to [$2\bar{4}23$] (see Table 6.4). From the measured widths, it was most probable that the dislocations were lying on the basal plane. In Figure

6.21 the slip plane was confirmed to be the basal plane using trace analysis. All slip bands within the primary-α grain in Figure 6.19 were on parallel basal planes.

Table 6.4 also lists the $\underline{g}$ vectors used to determine the Burgers vectors of dislocations in the basal slip band (Figures 6.19 and 6.20) using the invisibility criterion. The three dislocations, labelled A, B and C in Figures 6.20A to 6.20F, have different Burgers vectors since each dislocation went out of contrast under different two beam conditions. By referring the contrast values in Table 6.4 to those listed in the table in Appendix 1, the dislocations were determined to have <$\underline{a}$> type Burgers vectors; (A) $\underline{b}$ = 1/3[11$\bar{2}$0], (B) $\underline{b}$ = 1/3[1$\bar{2}$10] and (C) $\underline{b}$ = 1/3[$\bar{2}$110], which are permitted Burgers vectors for slip on the basal plane. The dislocations marked B are of near screw type since the true direction, U, lies close to $\underline{b}$. The dislocations marked A and C have a mixture of edge and screw components.

Using the techniques described above, the majority of slip bands observed in primary-α grains were identified to have occurred on the basal plane. The Burgers vectors of dislocations in these bands were of the 1/3<11$\bar{2}$0> type.

Figure 6.22 is an example of a primary-α grain from a back-thinned foil in which slip had occurred on two perpendicular planes. Slip on the band marked b was basal and slip on the band marked p occurred on a prism plane at 90° to the basal plane. It is interesting to note the nature of the dislocations within the slip bands. The dislocations in the basal slip band are often paired (see Figure 6.22) whereas those in the prism slip band are much more random in nature and contain many cut off loops and dislocation debris perhaps arising through the interaction of dislocations on the two slip planes.

6.5.2.2 Slip in Cross-sectional Thin Foils

The preparation of thin foils in cross-section afforded two main advantages: (i) The extent of fatigue damage as a function of depth below the fatigue surface could be determined. (ii) The angle between the slip bands and the fatigue surface could be measured. However it was observed that the depth below the fatigue surface to which the fatigue damage was present depended upon the orientation of the individual grains. Due to the limited extent of the thin areas obtained in cross-sectional thin foils, it was only possible to estimate the extent of fatigue damage below the fatigue surface. As expected, the highest density of dislocations was observed within the first few microns below the fatigue surface, generally over the extent of the adjacent primary-α/transformed-β colonies. All grains which were adjacent to the fatigue surface contained a relatively high concentration of slip band activity. As the distance below the fatigue surface increased, the slip band/dislocation density decreased. At greater than approximately 100 μm from the fatigue surface, the dislocation density was equivalent to that observed in unfatigued foils.

The majority of primary-α grains within 100 μm of the fatigue surface contained at least one active slip system. For example, the primary-α grain shown in Figure 6.23 shows basal slip occurring at 20° to the fatigue surface. Slip had occurred in primary-α grains at between 15° and 90° to the fatigue surface with a high proportion of the grains containing slip at between 35° and 55° to the fatigue surface, *e.g.* Figure 6.24. Basal slip was found to have occurred in all the primary-α grains which contained slip bands. In some grains where the angle between the basal slip and the fatigue surface was less than 20° or greater than approximately 70° other slip systems were activated. The planes of these slip systems were identified as either prism or pyramidal planes using trace analysis (see later in this section).

The two slip systems shown in Figure 6.25 were activated in a primary-α grain which was located at the fatigue surface of a cross-sectional foil. The slip bands occurred at 90° and at 40° to the fatigue surface. Table 6.5 lists the beam directions and two beam conditions under which the grain was imaged by T.E.M. and also the measured thicknesses of the two slip bands (marked 1 and 2 in Figures 6.25 and 6.26) at these zones. Figures 6.26A to 6.26C were taken under the conditions indicated in Table 6.5. By plotting the measured thicknesses of the bands on a standard stereographic projection, Figure 6.27, the slip which occurred at 90° to the surface (band 1) was identified as basal slip. Using trace analysis (explained in detail in Figures 6.28A to 6.28C), the other slip system activated at 40° to the fatigue surface was found to be on the $(\bar{1}101)$ pyramidal plane. Thus, the two active slip systems in this grain were; basal slip at 90° to the fatigue surface and pyramidal slip on the $(\bar{1}101)$ plane at 40° to the fatigue surface. Many of the dislocations in the basal slip bands in Figures 6.26A and 6.26B appear to be paired similar to those observed in the basal slip bands in Figures 6.17 and 6.22. Analysis of the basal planes edge-on (Figure 6.26C) shows that these dislocations are contained within a single slip band, strongly suggesting that they are ordered dislocations or superdislocations and are not dipoles.

The primary-α grain shown in Figure 6.29 was located within 5 μm of the fatigue surface in a cross-sectional foil. Two slip systems were activated at 15° and 75° to the surface. Table 6.6 lists the zones and two beam conditions used in tilting experiments. The measured thicknesses of the bands at each zone are also indicated. From this data, the two systems were identified to have occurred on the basal plane, at 75° to the fatigue surface, and the $(0\bar{1}10)$ prism plane, at 15° to the fatigue surface.

High densities of dislocations with a more tangled and wave-like appearance were found in two primary-α grains adjacent to the fatigue surface of cross-sectional foils, see Figures 6.30A and 6.30B. Analysis of these grains under the condition of B close to $[1\bar{2}10]$ and $\underline{g}$ = [0002], showed that dislocations with Burgers vectors of the <$\underline{c}$ + $\underline{a}$> type were present, Figure 6.30B. The traces of long, parallel slip bands can also be seen under this condition at 90° to $\underline{g}$ = [0002]. These slip bands occur on the basal plane. The angle between the basal slip bands and the fatigue surface was 20° in both the grains. An attempt to identify the plane on which the <$\underline{c}$ + $\underline{a}$> slip occurred was unsuccessful. However, based on the crystallography of titanium, the <$\underline{c}$ + $\underline{a}$> slip was probably on a pyramidal $\{10\bar{1}1\}$ type plane with a Burgers vector of the type $1/3\langle 11\bar{2}3\rangle$.

The primary-α grain in Figure 6.31 occurred adjacent to the fatigue surface in a cross-sectional foil. The single slip system in this grain occurred on the basal plane, at 75° to the fatigue surface. Figure 6.31 also shows a particle at the boundary between two primary-α grains which have a low misorientation. At the thickest region (centre) of this particle, basal slip bands have been arrested. However, at least two bands have passed through the particle where they have met with thinner regions. The deformation associated with these thinner regions is imaged in Figure 6.32. Figure 6.33A is a dark field micrograph of the particle imaged using the reflection indicated in Figure 6.33B. The particle was identified as a β phase particle using this and a convergent beam electron diffraction pattern, Figure 6.34. Smaller particles associated with the β phase particle were identified as titanium-zirconium silicides. The montage in Figure 6.35 was imaged under different diffraction conditions and substantiates the fact that the basal slip was arrested at the β particle. No evidence of cracking resulting from this interaction was observed, however, the build up of intense slip at such particles may lead to

crack initiation at the interface between a primary-α grain and a β particle.

6.5.2.3 Grain Orientations

The approximate orientations of over 30 grains (primary-α and transformed-β) in cross-sectional thin foils were determined by tilting the foils through less than 5° in order to obtain a zone axis diffraction pattern that could be indexed. The results are listed in Table 6.7 and are illustrated schematically on a standard stereographic triangle (0001)-(10$\bar{1}$0)-(11$\bar{2}$0) for titanium in Figure 6.36. When the preferred texture found in the disc (section 4.3.2, Figure 4.6) is interpolated onto such a triangle, it suggests that few grains in cross-sectional foils are orientated close to B = [0001] with the majority orientated nearer to B = {10$\bar{1}$0} and B = {11$\bar{2}$0}. The observed grain orientation measurements provide additional data to support the putative preferred texture measurement given in section 4.3.2

6.5.3 Slip in Transformed-β Colonies

Low magnification T.E.M. micrographs taken from the transformed-β in a back-thinned foil are shown in Figures 6.37A and B. These areas are typical of the transformed-β and show a higher dislocation density and a more homogeneous nature of deformation in grains close to the fatigue surface than in the primary-α (section 6.5.2). However, as the distance from the fatigue surface increases, the distribution of deformation becomes more inhomogeneous and most transformed-β colonies contain little or no deformation at greater than about 30 μm from the surface.

An example of the deformation within a transformed-β grain less than 4 μm from the fatigue surface in a cross-sectional foil is shown in Figure 6.38 and, at higher magnification, in Figure 6.39. The high

dislocation density was associated with slip on two systems within the α-platelets. Figure 6.40 shows two slip bands which cross an α-platelet boundary approximately 10 μm below the fatigue surface. Band 1 occurred almost parallel to the platelet boundary (dark) and band 2 at 60° to band 1. Table 6.7 lists the zones from which the slip plane of band 2 was determined to be the $(1\bar{1}00)$ prism plane, see also Figures 6.41A and 6.41B. From trace analysis, band 1 occurred on the $(01\bar{1}0)$ prism plane. Figures 6.40 and 6.41B show a high dislocation density built up at the α-platelet boundary in slip band 2 which suggests that the α-platelet boundary has caused some restriction to dislocation motion on the $(1\bar{1}00)$ plane. Prism slip was most commonly arrested at grain and colony boundaries.

Slip in the transformed-β was not confined to the prism planes. Figure 6.42 shows a transformed-β colony adjacent to the fatigue surface in a cross-sectional foil. A high density of slip occurred at 45° to the fatigue surface on basal planes, at 90° to the α-platelet boundaries. The α-platelet boundaries appeared to offer no restrictions to dislocation motion and basal slip was only arrested at the colony/grain boundaries, see Figure 6.43 and Figure 6.44. In Figure 6.44, the adjacent primary-α grain is the same grain as that illustrated in Figure 6.30A (section 6.5.2.2), which contained dislocations with Burgers vectors of the <**c** + **a**> type ($\underline{b} = 1/3\langle 11\bar{2}3\rangle$). The high density of basal slip in the transformed-β, which piled up at the grain boundary, may have increased the stresses in the adjacent primary-α leading to stresses high enough to generate <**c** + **a**> slip.

6.5.4 Microcracking

A total of four microcracks were observed in: (i) A transformed-β grain present in a back-thinned foil. (ii) A primary-α grain in a back-thinned foil. (iii and iv) A primary-α grain in a cross-sectional thin foil.

6.5.4.1 Microcracking in Transformed-β

Figure 6.45 is a low magnification montage illustrating a microcrack, approximately 6.5 μm in length, observed in a transformed-β grain present in a back-thinned foil. The crack followed a 'zig-zag' path through the microstructure, sometimes changing direction by up to 90°. It appeared that the crack followed an α-platelet or colony boundary and changed direction at slip bands which passed through the boundary or at particles such as silicides contained within the boundary. Because of the heavy deformation associated with the crack, it was not possible to fully characterise the crack path. The high level of deformation associated with the microcrack is illustrated in Figures 6.45 and 6.46. The density of dislocations was so high that individual dislocations were unresolvable, in contrast to the observations of transformed-β which did not contain a microcrack (Section 6.5.3). The plastic zone ahead of one end of the microcrack is illustrated in Figures 6.46 and 6.47. Figure 6.47 shows that the region of high dislocation density did not extend far from the crack. The build up of deformation at the boundary between the transformed-β and an adjacent primary-α grain caused a significant amount of strain in the primary-α grain. Evidence of this strain is shown in Figure 6.46 by the high dislocation density, localised nature of the thickness fringes and streaking, in a band of deformation which extends into the primary-α grain.

6.5.4.2 Microcracking in Primary-α

Figure 6.48 is a low magnification T.E.M. micrograph of a crack approximately 2 μm in length which occurred in a primary-α grain in a back-thinned foil. The area in Figure 6.48 is sketched in Figure 6.49 and shows that the crack occurred parallel to slip bands in the primary-α. Figure 6.50 shows the deformation associated with the crack which is highlighted by the bend contours around the

crack tip and also the dislocations which can be resolved along the crack length. Dislocations which extend in pairs from the crack tip to a distance of approximately 1 μm indicate the presence of short range order in the primary-α. The Burgers vector and slip plane of the dislocations were identified as $1/3[1\bar{2}10]$ and the (0001) plane, respectively (see Figure 6.51). Since the microcracking is parallel to the slip plane under the condition $\underline{g} = 0002$, this suggests that the microcrack had occurred on the basal plane in the primary-α. Also shown in Figures 6.50 and 6.52 are four bands of dislocations on one side of the crack which are up to 0.5 μm in length and 0.2 μm apart. These lay at 75° to the crack in a region just ahead of the crack tip. Figure 6.52 shows that a significant amount of deformation had occurred along the length of the crack, however, analysis of the deformation was not possible due to the strain associated with the crack. Observation of the crack tip closest to the edge of the foil was not possible because of pitting which had occurred during the electropolishing process (Figure 6.49). Two pits were present between the crack and the thin foil edge but no deformation was observed in this region.

Figure 6.53 is a low magnification T.E.M. montage from a cross-sectional thin foil. Two microcracks occurred parallel to each other in a primary-α grain, about 15 μm below the fatigue surface. The angle at which the cracks occurred was at 75° to the fatigue surface. One of the microcracks was approximately 4.2 μm long and the other about 2.2 μm in length.

The crack tip closest to the fatigue surface of the longer crack was bounded by an elliptical particle about 0.6 μm long. The particle was located on the boundary between two similarly orientated primary-α grains (labelled A and B in Figure 6.53) and identified from diffraction pattern analysis as a β phase particle, see Figures 6.54A and B. A high dislocation density across the β particle occurred at

the point where dislocations from the slip band in grain A had piled up. It is suggested that the dislocation pile up in the primary-α caused the β particle to deform as illustrated in Figure 6.54. In Figure 6.55 the slip bands in grain A are imaged under the condition $\underline{g}$ = 0002. The plane of the microcrack is parallel to the slip bands and therefore lies on the basal plane.

The crack tip furthest from the fatigue surface is shown as a dark field image ($\underline{g} = 20\bar{2}0$) in Figure 6.56. The region ahead of the crack tip contained a high density of <$\underline{a}$> type dislocations. Figure 6.56 also shows a zone of about 5 μm in length which extends into the region of high dislocation density. Figure 6.57 was taken under different conditions and shows Moiré fringes extending 2 μm from the apparent crack tip, indicating that the crack extended further into the foil than it appears in Figure 6.57. Figure 6.58 shows these fringes at high magnification to be between 6 and 10 nm apart.

6.5.5 Summary of Thin Foil Observations

Intense planar slip bands which traversed the grain widths are characteristic of fatigue damage accumulation in the primary-α grains of IMI 834. Basal slip of the type $1/3<11\bar{2}0>(0001)$ is the predominant mode of deformation in primary-α grains, under the testing conditions studied and is present in all primary-α grains observed to contain slip bands. Basal slip is the only slip system present in over 50% of primary-α grains, in the remainder of primary-α grains either no slip systems or two slip systems (one of which is basal slip) are observed. Many of the basal slip bands contain dislocations which occur in pairs (see Figures 6.17, 6.22, 6.26 and 6.52). The occurrence of these paired dislocations is discussed further in section 7.3.4.1. The secondary slip systems observed to form in primary-α grains are prismatic ($1/3<11\bar{2}0>\{10\bar{1}0\}$) slip or pyramidal ($1/3<11\bar{2}0>\{10\bar{1}1\}$) slip and these occur when the angle between the fatigue surface

and the basal slip is high (> 70°). <c + a> slip is also identified in primary-α grains close to the fatigue surface when the angle between the basal slip and the fatigue surface is low (about 20°in the cases found). The slip plane and Burgers vectors of the <c + a> slip are not determined, but are probably pyramidal $\{10\bar{1}1\}$ and $1/3<11\bar{2}3>$, respectively. Primary-α/transformed-β grain boundaries and β phase particles on low angle boundaries between primary-α grains are observed to act as effective barriers to slip in the primary-α grains.

Slip in the transformed-β appears more homogeneous in nature than in the primary-α and a greater slip band density is generally observed, especially near the fatigue surface. Prismatic ($1/3<11\bar{2}0>\{10\bar{1}0\}$) slip and basal ($1/3<11\bar{2}0>(0001)$) slip are observed with about equal frequency in the transformed-β colonies. The basal slip occurs at 90° to the α-platelet direction and appears to cross the α-platelet boundaries with little or no effective slip band arrest. The prismatic slip normally occurs in two of the three possible directions and runs nearly parallel to α-platelet boundaries and/or approximately 60° to them when observed 'edge-on'.

Basal slip in the transformed-β is arrested at colony boundaries and at boundaries of adjacent primary-α or transformed-β grains. Prismatic slip in transformed-β is arrested at similar boundaries to basal slip. In addition, some restriction to the motion of dislocations through a colony is caused by the α-platelet boundaries (for example Figure 6.41B), however, these boundaries are not considered to be a major barrier to slip in IMI 834.

The microstructure associated with four microcracks found in thin foils is presented. Two of the microcracks occurred in a transformed-β grain and a primary-α grain in foils which had been back-thinned (by electropolishing). The most notable feature associated with the microcrack in the transformed-β is the high

dislocation density around the crack and in the plastic zone ahead of the crack tip. The microcrack in the primary-α grain was determined to occur along a basal plane. Two other microcracks were found in a primary-α grain which was approximately 15 μm below the fatigue surface of a cross-sectional thin foil. Both microcracks were found to have occurred along a basal plane at 75° to the fatigue surface.

CHAPTER SEVEN

DISCUSSION

7.1 OBSERVATIONS ON UNFATIGUED MATERIAL

7.1.1 Composition

Table 7.1 compares the compositions of IMI 834 analysed by different workers [32, 33, 90, 190], the nominal composition [6] and the composition determined in the present investigation. All the values are consistent apart from those for tin and zirconium which vary from 3.5 to 4.7 wt% and 3.4 to 4.0 wt%, respectively. The aluminium equivalent, Al*, was determined, using equation 2.4 (section 2.2.5.1), to be greater than 9 wt% in each case. This value of Al* was considered by Rosenberg [44] to be the limit of Al*, above which excessive α_2 (Ti_3Al) formation seriously reduces the fracture toughness and ductility of titanium alloys. However, Neal [9] stated that an alloy which had been α+β processed was less susceptible to ordering instability than if it were β-processed. Consequently, for α+β alloys such as IMI 834, the Al* could be increased to give an improvement in the creep and fracture properties.

In the above analyses, the value of Al* was determined from the compositions of the bulk material. However, during alloy processing, the segregation of α-stabilisers to the primary-α grains and β-stabilisers to the prior-β grains occurs [32]. This segregation results in the primary-α and α-platelets having different chemistries. Scanning transmission electron microscopy (STEM) analysis of these grain types has been carried out on IMI 834 [191] and the results (in atomic %) are presented in Table 7.2 (Also given are the composition of the silicide precipitates and retained-β phase along the α-platelet boundaries). From the results of this analysis, the

difference in chemistry between the primary-α and α-platelets is small. The Al* (at%) in the primary-α is only slightly higher than in the α-platelets, yet Ti_3Al reflections in diffraction patterns from primary-α grains were always observed and were often fairly intense (Figure 4.22A), whereas reflections from Ti_3Al in the α-platelets were only occasionally observed and were barely resolvable (section 4.4). However, the difference in the composition between the two grain types will also be influenced by the interstitial elements, carbon and oxygen, which were not analysed by Shollock [191]. Both oxygen and carbon are α-stabilisers and it is therefore probable that the diffusion of these elements to the primary-α occurs during processing causing a marked increase in the Al* of the primary-α phase.

The addition of a small quantity of carbon to the alloy IMI 834 is important for three reasons: (i) It allows a practical α+β heat treatment (see Figure 2.4, section 2.2.4.1 and section 2.3.1). (ii) It increases the β-transus temperature [192]. (iii) It improves the tensile strength of the alloy throughout the desired temperature range [31, 131, 192]. However, the addition of carbon is detrimental as it increases the Al* by up to 0.6 wt% (equation 2.4, section 2.2.5.1), bringing it above the 9 wt% level considered to be the upper limit to avoid excessive Ti_3Al formation in titanium alloys [44]. This point has been overlooked in the literature [31, 131, 192], possibly because of the larger number of advantages brought about by the addition of carbon to IMI 834. However, this increase in the Al* is significant, since the formation of Ti_3Al has important implications on the deformation behaviour of IMI 834 (see section 7.4.1.1).

7.1.2 Microstructure

7.1.2.1 Optical Microstructure

A fine, duplex microstructure of equiaxed primary-α and basketweave transformed-β was observed in specimens taken from the compressor disc section (section 4.2). This is typical of an α+β processed, oil quenched and aged titanium alloy (see section 2.2.4.2). Such a microstructure was designed to produce the optimum balance of properties, combining the advantages of β-processed near-α alloys (*e.g.* IMI 829 and IMI 685) with those of α+β processed alloys (*e.g.* Ti-6Al-4V) [6, 9, 10, 192]. Thus, the high creep resistance was maintained by a high α-stabiliser content and favourable fatigue resistance and crack tolerance were achieved from the a fine grained microstructure (see section 2.3.1).

7.1.2.2 Effect of Primary-α Content

One of the microstructural parameters considered by workers during the development of IMI 834 was the volume fraction of primary-α present in the microstructure after solution treatment. In the present work, a volume fraction ($^{v}/_{o}$) of 18.84 ± 1.9% primary-α phase was determined (section 4.2).

The volume fraction of primary-α was typically altered by varying either the solution treatment temperature (see Figure 2.4, section 2.2.4.1) or the cooling rate from the solution treatment temperature. For example, Table 7.3 gives some of the results of heat treatments carried out on IMI 834 by various workers [32, 168, 190]. Figure 7.1 illustrates the effect of the volume fraction of the primary-α on the creep and fatigue performance of IMI 834. The cross-over in the fatigue performance and creep resistance curves indicates the point at which the two conditions can be optimised. A range of optimum values has been reported, for example, Neal [9] suggested 5 $^{v}/_{o}$

primary-α and Bate *et al.* [33] 7 to 8 $^{v}/_{o}$ primary-α. Postans [10] and Goosey [6] suggested that 12 to 15 $^{v}/_{o}$ primary-α provided the best balance between creep and fatigue properties. More recently Neal [31] and Daeubler [192] found that a higher primary-α content of 15 $^{v}/_{o}$, together with a 700°C ageing temperature provided the optimum property combination. The value of 18.84 $^{v}/_{o}$ in the present work is therefore slightly higher than that suggested as the optimum by most workers. However, as discussed later (section 7.3.2), the fatigue behaviour of IMI 834 appears to be insensitive to the volume fraction of primary-α [168].

7.1.2.3 X-ray Diffraction

All lattice parameters in the present work were determined at room temperature. The lattice parameters, $\underline{a}$ = 0.2951 nm and $\underline{c}$ = 0.4686 nm, obtained from the α phase (section 4.3.1) agree with those listed for α-titanium in the standard X-ray powder data files [193]. In the present investigation, the lattice parameter of the retained-β was measured by X-ray diffraction as $\underline{a}$ = 0.3264 nm. This value agrees favourably with a value for β-titanium of $\underline{a}$ = 0.33065 nm determined from a commercially pure titanium alloy [194]. However, direct comparison is not possible since pure β phase titanium cannot be retained on quenching to room temperature and thus the lattice parameter for β-titanium was measured at a temperature above the β-transus temperature (882°C). The addition of β-stabilising elements to an alloy, such as IMI 834, causes the β phase to be retained on quenching (section 2.2) and, consequently, allows measurement of the lattice parameter to be made at room temperature. A number of workers calculated the lattice spacing of pure β-titanium at room temperature by extrapolation to zero β-stabiliser content of the lattice spacing curve of quenched alloys [195, 196]. Values extrapolated from different alloy systems were; $\underline{a}$ = 0.3282 nm (Ti-Mo-Cr) [196] and $\underline{a}$ = 0.3294 nm (Ti-V) [195]. The lattice parameter, $\underline{a}$ = 0.319

nm was obtained from the α+β alloy Ti-6Al-4V by X-ray diffraction at room temperature [197]. Since the β-stabiliser content of IMI 834 is low, the lattice parameter of the β phase ($\underline{a}$ = 0.3264 nm) is comparable to the extrapolated values ($\underline{a}$ = 0.3282 nm and $\underline{a}$ = 0.3294 nm), but is higher than that determined for Ti-6Al-4V because of the higher β-stabiliser (vanadium) content which has the effect of reducing the lattice parameter.

7.1.2.4 T.E.M. of Transformed-β Grains

The α-platelet morphology observed in thin foils of IMI 834 corresponds with the basketweave microstructure observed in oil quenched, near-α titanium alloys [32, 63, 64, 66, 178, 198]. Many investigations have observed the effect of different processing temperatures, cooling rates and ageing times on; (i) the morphology of the α-platelets, (ii) the distribution of dislocations within the α-platelets, (iii) the amount of retained-β phase and (iv) the precipitation of silicide particles, in various near-α titanium alloys [51, 64, 90, 198]. In general, material which is cooled at a faster rate from the processing temperature (oil or water quenched) is found to contain a higher dislocation and stacking fault density in the α-platelets when compared to material which has been air cooled [64, 66]. The higher dislocation density of quenched material is generated by the stresses associated with the faster β to α transformation.

Cope and Hill [32] studied the effect of ageing temperature on the microstructure of α+β processed and oil quenched IMI 834 which was aged at 600, 650 and 700°C for four hours and observed by T.E.M. Material aged at 600°C contained thin films of retained-β which were surrounded by dislocation arrangements at, or close to, the α/β interface. These arrangements accommodated the lattice mismatch between the α and β phases. In material aged at 700°C, some retained-β had spheroidised and appeared discontinuous along the α-platelet boundaries.

As a consequence of the β-spheroidisation, the dislocation density in the interface region decreased due to the reduced requirement for α and β lattice accommodation [32]. Since the alloy in the present investigation was aged for two hours at 700°C, the T.E.M. observations of the transformed-β (Figures 4.8 and 4.9) are in good agreement with those made from material which was aged for four hours at 700°C [32]. Similar lattice mismatch dislocations were also observed in IMI 829 which had been aged at 575°C for up to 1000 hours [64, 66].

The precipitation, distribution and subsequent growth of silicides has caused much excitement in the literature as already discussed in section 2.2.5.2. Silicides with lattice parameters, $\underline{a}$ = 0.703 ± 0.004 nm, $\underline{c}$ = 0.360 ± 0.015 nm, were observed in the present investigation (section 4.4.1). The lattice parameters are similar to those measured from aged specimens of IMI 834; $\underline{a}$ = 0.70 nm and $\underline{c}$ = 0.36 nm [90] and $\underline{a}$ = 0.69 and $\underline{c}$ = 0.33 nm [33]. The lattice parameters correspond to silicides of the S_2 type (*i.e.* $(TiZr)_6(SiSn)_3$, section 2.2.5.2). Ramachandra *et al.* [90] observed the S_2 type silicide to form in IMI 834 after α+β and β-processing treatments which were followed by water quenching and ageing at between 600 and 700°C. From their results they concluded that S_2 was the only type of silicide to form in IMI 834 under the conditions given. The orientation relationship between the silicides (s) and the α-platelets (α) determined in the present work agrees with that found by Ramachandra *et al.* (in their case the orientation relationship was between the silicides and the martensite laths (α′)):

$$[01\bar{1}1]_\alpha // [\bar{2}110]_s \; ; \; (\bar{2}110)_\alpha // (01\bar{1}0)_s \qquad (7.1)$$

In the present work, the precipitation of silicides was observed on α-platelet, colony and grain boundaries and occasionally on dislocations within α-platelets. These observations agree with those in the literature [33, 64, 67, 90]. Ramachandra *et al.* [90] concluded that, in the

β-processed condition, the precipitation of silicides in IMI 834 was predominantly at the α-platelet boundaries, whereas, in the α+β processed condition, silicides also precipitated at the primary-α/transformed-β boundaries. The higher precipitation kinetics in the latter condition were attributed to the role of the β-stabilising elements which partitioned to the transformed-β [90].

Woodfield *et al.* [64, 66, 198, 199] and White *et al.* [178] analysed the nature of the dislocations within the transformed-β microstructure. In the α-platelets of oil quenched IMI 829, the majority of dislocations had Burgers vectors of the type $1/3\langle 11\bar{2}0\rangle$ and $1/3\langle 11\bar{2}3\rangle$. In addition, a significant fraction of the dislocations produced by oil quenching were observed to bound stacking faults [64, 66, 178, 198]. In the present investigation, $1/3\langle 11\bar{2}0\rangle$ type dislocations were observed, however the presence of the $1/3\langle 11\bar{2}3\rangle$ dislocations was not actively sought. Similar observations of stacking faults and bounding dislocations were also observed in the present investigation (Figure 4.15, section 4.4.1). The bounding dislocations were identified by Woodfield *et al.* [199] as partial dislocations which had Burgers vectors of the type $1/6\langle 20\bar{2}3\rangle$ and the stacking faults were found to lie on the basal plane. It was argued that the faults may have been produced by mis-stacking events during the growth of α-platelets [199].

7.1.2.5 T.E.M. of Primary-α Grains

Hexagonal dislocation networks were observed in the primary-α grains of IMI 834 (section 4.4.2, Figures 4.18 and 4.19). Similar networks were observed in annealed α-titanium and represented low angle grain boundaries between two primary-α sub-grains [200]. Their formation was believed to occur from interactions between two sets of dislocations lying on two parallel non-basal slip systems. The sets were formed between either two screw dislocation arrays with $\underline{b}_1 = \underline{b}_2$ or two edge dislocation

arrays with $\underline{b}_1 = -\underline{b}_2$ [200]. Agrawal *et al.* [201] also analysed similar networks in commercial Ti-A50 titanium and concluded that, in the as-annealed condition, hexagonal dislocation networks occurred on the prism, basal and {$\bar{2}$11X} planes.

In a study of the titanium alloy VT5-1ct (similar in composition to Ti-5Al-2.5Sn), Grinberg *et al.* [202] found dislocation networks in the primary-α sub-grains. The networks were commonly observed and were formed during the high temperature compaction initially given to the alloy [202]. In the present study similar networks are found in primary-α sub-grains in IMI 834 (Figures 4.19 to 4.21). On the basis of the observations by Grinberg *et al.* [202], the networks observed in IMI 834 in the present study are considered to have formed as a result of the initial forging process.

The presence of Ti_3Al was detected in all primary-α grains of IMI 834 by the occurrence of extra reflections in diffraction patterns (section 4.4.2). Ti_3Al reflections were not observed in the majority of the transformed-β grains. This distribution of Ti_3Al in the alloy is expected due to the segregation of α-stabilising elements, such as aluminium, to the primary-α phase during solution treatment [32, 191]. The growth of Ti_3Al precipitates occurs on ageing. Cope and Hill [32] observed Ti_3Al precipitates to be approximately 2.5 nm in diameter and 10 nm apart after ageing IMI 834 for four hours at 700°C. In the present investigation the precipitates were too small to be resolved by T.E.M. since the alloy was aged for just two hours at 700°C. The precipitation of Ti_3Al has important implications on the fatigue behaviour of IMI 834 and this is discussed in section 7.4.1.1

7.2 THE INTERFACE PHASE (IFP)

7.2.1 Foil Preparation Techniques

Initial attempts to prepare cross-sectional foils of fatigued specimen sections involved plating the fatigue surface of interest with nickel in order to protect the surface and to aid its identification in the T.E.M. (section 3.3.5.3). When observed by T.E.M. a change from the expected microstructure was found, this is summarised schematically in Figure 7.2. Within 150 μm of the plated surface the microstructure had dramatically altered such that the original microstructure was barely identifiable (Figures 5.2 and 5.3). Between about 150 and 250 μm from the surface, an interface phase along the α-platelet boundaries and a second phase, in the form of acicular bands across the width of α-platelets, were observed (Figures 5.4 and 5.5). At distances of greater than 250 μm from the surface only an interface phase along the α-platelet boundaries was found.

The origin and identification of the interface phases was important as it was unclear whether they were wholly or partly artefactual or, indeed, whether they were the result of fatigue damage. Several different preparation techniques were carried out to establish at which stage of foil preparation these phases had formed (see Table 5.1). The interface phases were never found in either; (i) unfatigued or fatigued foils prepared by electropolishing, (ii) back-thinning or (iii) dimpling followed by electropolishing. However, foils prepared by dimpling followed by ion-beam milling and by electropolishing followed by ion-beam milling contained an interface phase along some of the α-platelet boundaries. The absence of any interface phases in electropolished foils suggests that the interface phase along the α-platelet boundaries is a thin foil artefact which was formed during the ion-beam milling process. It is suggested that the nickel plating process used in the preparation of cross-sectional

foils has induced both interface phases to form.

A review of the theories in the literature regarding the origin of the interface phases (IFP's) is given in section 2.2.6. A similar phase to that identified in the present study was found along the α-platelet boundaries of various titanium alloys and was determined to be a face centred cubic (fcc) hydride of titanium which arose as a result of an increase in hydrogen concentration in thin foils during electropolishing [81, 83-85, 89]. A second phase with an hcp structure was found in a $<10\bar{1}2>\{10\bar{1}1\}$ twin relationship to the α phase and was considered by some workers to form as a result of stresses at the α/β interface arising from thin foil relaxation in the β phase during electrolytic thinning [81, 83]. Ion-beam milling was said to prevent the formation of both the fcc phase along the α-platelet boundaries and the hcp phase [81, 83, 89].

In the present investigation, the observation that the IFP's are thin foil artefacts (Table 5.1, section 5.2) agrees with the observations given in the literature [81, 83-85, 88, 89]. However, the observation of an fcc IFP along some α-platelet boundaries in foils prepared by techniques involving ion-beam milling and the absence of any interface phases after electropolishing, are in conflict with the literature (Table 7.4). A possible explanation for the observations in the present work is that water may have been an impurity in the argon gas used during the ion-beam milling process. Hydrogen ions derived from this water may have been absorbed by the thin foil causing the interface phase to form along some of the α-platelet boundaries. In electropolished foils, the hydrogen content was minimised by maintaining the temperature at < -50°C (section 3.3.5.1).

In the nickel plated cross-sectional thin foils it is proposed that hydrogen was absorbed into the alloy during the plating process. A hydrogen gradient may have been

established which was a maximum concentration at the fatigue surface and decreased as the distance into the bulk material increased. At between 150 and 250 μm from the surface, two interface phases were observed. The fcc phase along the α-platelet boundaries was crystallographically identical to the IFP identified in the literature to be a hydride of titanium [85]. The second phase which formed as acicular bands across the width of α-platelets could not be fully identified in the present investigation despite analysis using high resolution T.E.M. However, from the evidence available, this phase was probably hcp in structure. It is possible that this phase may result from twinning which may be induced by the increased stresses in the foil from the formation of the fcc IFP along the α-platelet boundaries and the relaxation of surface constraints in the foil (see section 7.2.2). At greater than 250 μm from the surface, the hydrogen content of the foil was sufficiently high to form the fcc IFP along the α-platelet boundaries but not high enough to form the acicular phase.

7.2.2 Crystallography of the IFP

The lattice parameter, $\underline{a}$ = 0.434 ± 0.004 nm, determined in the present investigation lies within the range found in the literature for the monolithic fcc IFP (0.420 nm ≤ $\underline{a}$ ≤ 0.453 nm, Table 2.3). The actual value of $\underline{a}$ is dependent on the alloy composition, prior heat treatment, cooling rate and/or foil preparation technique [70-73, 75, 78-86]. In the present investigation two orientation relationships between the fcc phase and the α phase were found (equations 5.1 and 5.2), however, when the stereographic projections from both the primary-α phase and fcc IFP are compared, both equations may simply be represented by the orientation relationship (equation 5.2);

$$[011]_{\beta}//[0001]_{\alpha}//[001]_{fcc}\ ;$$
$$(112)_{\beta}//(10\bar{1}0)_{\alpha}//(011)_{fcc} \qquad (7.2)$$

Equation 7.2 agrees with the orientation relationship found for the monolithic fcc phase by Banerjee *et al.* [85], indicating that the interface phase found along the α-platelet boundaries in the current study is identical to that found by Banerjee *et al.*

A second crystallographic form of the fcc IFP was referred to in the literature [78, 81-86] as the striated fcc IFP. A different orientation relationship has been determined for the striated phase by many workers [78-81, 83-86]:

$$[111]_{\beta}//[11\bar{2}0]_{\alpha}//[110]_{fcc}$$
$$(110)_{\beta}//(0001)_{\alpha}//(1\bar{1}1)_{fcc} \; ; \qquad (7.3)$$

Banerjee *et al.* [85] suggested that careful diffraction pattern analysis could clearly reveal the structural differences between the strongly resembling striated fcc morphology and hcp phase morphology, which had caused so much confusion in earlier work (see section 2.2.6). In their work appropriate ageing treatments were chosen for the alloy Ti-10V-2Fe-3Al in the range 500 to 700°C so that the α-platelets were large enough to be analysed individually by selected area diffraction. The hcp phase was found to exist in six variants formed by twinning on the six possible $\{10\bar{1}1\}$ planes of the parent α-platelets [85]. Banerjee *et al.* [85] believed that the hcp phase was a stress induced phase formed by the volume expansion of the β phase and concomitant compression of the α phase due to hydrogen absorption during electropolishing. Twinning was suggested as the favoured deformation mode when the α-platelet sizes were small. Figure 5.4 shows examples of acicular bands, which are considered to be the same phase, observed at between 150 and 250 μm from the fatigue surface. As shown in Figures 5.5 and 5.8, the bands occurred in specific crystallographic directions both across the α-platelets and also parallel to the α-platelet boundaries (between the monolithic fcc phase and the α-platelet phase). It is suggested that the acicular bands are stress induced during ion-beam milling.

In agreement with Banerjee *et al.* [85], hydrogen in the bulk material is believed to segregate to the retained-β phase. At high hydrogen concentrations, such as those in the nickel plated foils, this effectively places the β phase in compression. The removal of material during ion-beam milling promotes the relaxation of bulk material constraints allowing the β phase to expand. The expansion of the retained-β is accompanied by the formation of the monolithic fcc IFP along the α-platelet boundaries which places the α-platelets under compression. The stresses induced in the α-platelets cause the formation of the acicular bands across them. In view of the observations made by Banerjee *et al.* [85], it is probable that the bands are twins and have an hcp structure.

7.3 FATIGUE DAMAGE

7.3.1 Mechanical Testing

7.3.1.1 Tensile Tests

Table 7.5 compares the room temperature tensile properties of IMI 834 specimens determined in the present investigation with values obtained in the literature [31, 32, 168, 169, 190, 203] for similarly processed material. The room temperature 0.2% proof strength (P.S.) and ultimate tensile strength (U.T.S.) of tangential and radial specimens are lower in the present work than those quoted in the literature [31, 32, 168, 203]. The reasons for this difference are unclear but may have arisen from variations in the exact locations of test specimens, processing conditions and/or testing conditions. However, in comparison with other high temperature near-α titanium alloys such as IMI 829 and Ti-6242-S [6], the values determined in the present work are over 60 MPa higher. It is probable that a range of properties exist across the compressor disc section which may have arisen from differential cooling rates caused by variations in the

compressor disc thickness. The higher tensile strength values determined for the specimen from the disc rim (Figure 3.1C, Table 6.1) is likely to have resulted from a faster cooling rate from the solution treatment temperature at the rim, compared to other areas of the compressor disc section.

7.3.1.2 Fatigue Tests

Figure 7.3A compares, as a function of the maximum stress (σ_{max}), the fatigue life data of IMI 834 obtained in the present investigation with those determined for similarly processed material [131, 190, 192, 204]. Figure 7.3B shows the same data as a function of the 0.2% proof stress.

The number of cycles to failure are significantly higher in the present work [31, 190, 192, 204] (Figure 7.3B). However, because the type of test specimen and frequency of testing used are different from those used by Daeubler *et al.* [31, 190, 192, 204], it is difficult to compare these results directly. Load controlled four point bend specimens were fatigue tested in the present investigation, whereas load controlled tension-tension type specimens of IMI 834 were tested by Daeubler *et al.* An investigation into the effects of different fatigue test types was carried out by Yates [205] on Waspaloy, a nickel based superalloy. The results showed statistically that four point bend testing produces a longer fatigue lifetime than tension-tension type testing under the same loading conditions.

The frequency of testing in the present work was 5 Hz, whereas in the tests by Daeubler *et al.*, a frequency of 0.3 Hz was used. Munz *et al.* [157] observed the effect of increasing the testing frequency on the fatigue life of titanium (Contimet 30). On increasing the frequency from 0.5 Hz to 5 Hz, the average number of cycles to failure increased from approximately 9 x 10^4 to 14 x 10^4, which

represents an increase in lifetime of over 50% [157].

It is probable that the higher fatigue lifetimes determined in the present investigation, compared to those found by Daeubler *et al.*, are influenced by the testing type and the higher testing frequency used.

7.3.2 Fatigue Surfaces

Slip bands occurred in suitably orientated primary-α grains of fatigued specimens over the entire 35.0 x 10.0 mm area of maximum stress. The bands were observed at between 40° and 90° to the applied stress direction. Slip in the transformed-β occurred at 90° and 60° to the direction of the α-platelets. From T.E.M. observations, these directions in the transformed-β correspond to the basal and prism slip planes, respectively.

A preference for crack initiation along planar slip bands in the primary-α grains was observed in the present work (section 6.3.2). A similar preference has been found for room temperature low cycle fatigue crack initiation in many duplex, α+β processed titanium alloys (see section 2.5.6) including Ti-6Al-4V [21], Ti-17 [135], Ti-6246 [165, 166] and IMI 834 [168, 169].

Dowson *et al.* [168, 169] observed the low cycle fatigue crack initiation response in IMI 834 containing volume fractions of 5, 15 and 25% primary-α phase. The material had been processed according to the heat treatments presented in Table 7.6 [168, 169]. Load controlled, low cycle fatigue tests were carried out at 20°C under either three point bend or tension-tension loading with R = 0.1 or 0.7, f = 25 Hz and a peak stress, $\sigma_{max} \leq$ 90% of the 0.2% P.S. From the results of tensile fatigue tests, Dowson *et al.* found that fatigue cracks initiated exclusively in the primary-α phase and were associated with the formation of intense slip bands which ultimately

extended across the full grain diameter. Under three point bend testing, cracks were again associated with slip bands, however, initiation sites within the transformed-β grains were occasionally observed [168]. Crack initiation in a 15 $^{v}/_{o}$ primary-α microstructure, which was fatigued at 80% of the 0.2% P.S., was found to be associated with the development of intense slip bands at between 30° and 70° to the principal stress axis [169]. In the present investigation, slip bands in the primary-α were found between 40° and 90° to the applied stress direction and initial primary cracks and secondary cracks were found between approximately 45° and 90° to the applied stress direction in specimens fatigued at 95 or 100% of the 0.2% P.S. The greater applied stresses in the present investigation may explain the larger range of initial crack orientations observed. Apart from this larger range of slip band and initial crack orientations, the observations made in the present study are in agreement with the results of Dowson *et al.* [168, 169].

Attempts by Dowson *et al.* [168] to quantify the initiation process in terms of various test parameters were unsuccessful. No correlation between the number of cycles to crack initiation and the level of applied stress was found. In addition, crack initiation was determined to be insensitive to variations in the primary-α phase volume fraction (5, 15 and 25 $^{v}/_{o}$) despite the general preference for cracks to initiate in the primary-α phase [168].

Dowson *et al.* [169] found that many secondary cracks propagated linearly at an angle to the applied stress for a significant period before finally being deflected towards the expected crack propagation direction (which is 90° to the applied stress direction) at a grain or colony boundary. These observations suggested that the initial paths of propagating cracks were along favourably orientated slip bands. Similar findings were made in the present work with the observation that there was a preference for short crack paths to propagate more easily

through the transformed-β at 90° to the α-platelets (see Figures 6.5, 6.6 and 6.8). From T.E.M. observations this direction corresponds to the basal plane in the transformed-β grains. The propagating cracks changed direction so that this orientation could be followed preferentially. Beyond about 300 μm in length, this preference was not as pronounced. Dowson suggested that slip compatibility between neighbouring primary-α and transformed-β grains was an important consideration in the process of crack formation. The results of the present investigation agree with this suggestion and further suggest that it is less tortuous for a crack to propagate from an initiating primary-α grain if the α-platelets in adjacent transformed-β colonies are orientated such that the crack can follow a path at 90° to the α-platelet boundaries, *i.e.* propagate along the basal plane.

Dowson *et al.* [168, 169] concluded that the crack initiation response and the global crack propagation characteristics of IMI 834 were relatively independent of the volume fraction of primary-α (up to 25 $^{v}/_{o}$) for the limited stress range studied. The crack propagation was governed primarily by the crack length, the level of cyclic damage introduced prior to crack initiation and by the magnitude of the applied stress. The results of Dowson *et al.* suggest that an optimum volume fraction of primary-α in IMI 834 is not as critical for fatigue properties as suggested by Neal [31] and Daeubler *et al.* [192] (section 7.1.2.2).

7.3.3 Fracture Surfaces

A macroscopically visible change in fracture surface appearance from a shiny semi-circular region up to 3 mm in radius around the fatal crack origins to a matt region at greater distances was observed on all failed specimens (section 6.4.2). S.E.M. examinations of the two regions revealed that the semi-circular region close to the origin contained a large number of flat facets (Figure 6.14). In

the matt region beyond the transition fluting and micro-serrated ridges produced a more ductile fracture surface appearance.

A similar, macroscopically visible, transition in fracture appearance was observed by Wanhill *et al.* [206] in compact tension specimens of Ti-6Al-4V containing a duplex microstructure. A detailed summary of the pre-transition and post-transition fractographic features was presented [206]. The fracture surface features found in failed specimens of IMI 834 correspond well with those reported by Wanhill *et al.* [206]. In the present investigation, characteristic pre-transition features found close to the crack origins were; (i) cleavage facets in the primary-α phase which contained river markings and (ii) micro-serrated ridges resulting from fracture of the transformed-β phase. Typical post-transition features were a blocky fracture appearance and rough cleavage containing micro-serrated ridges which give the more ductile appearance of the fracture surfaces in these regions.

Many studies of titanium alloys have shown that this transition in fractographic appearance occurs at a change in the gradient of fatigue crack growth rate (da/dn (m/cycle)) versus ΔK ($MPam^{1/2}$) curve [97, 102, 161, 171, 206, 207]. From a detailed investigation of fatigue crack growth in Ti-6Al-4V, Wanhill *et al*. [206] concluded that a transition in the fatigue crack growth rate curve correlated with a change from a structure-sensitive to a continuum-mode of crack growth, which in turn was associated with the transformed-β grain size. Analysis of the fatigue crack growth curve transition was made by correlating the cyclic plastic zone sizes of the propagating cracks with microstructural features such as the grain and colony sizes [206]. The cyclic plastic zone sizes were calculated using the formulae proposed by Hahn *et al.* [208]. The most useful formula was that for the cyclic plastic zone size in the y direction, which

determined the maximum extent of the plastic zones:

$$[r^c]_y = 0.132(\Delta K/2[\sigma^c]_y)^2 \qquad (7.4)$$

where:

$[r^c]_y$ = the cyclic plastic zone size (m)
$[\sigma^c]_y$ = the yield strength (MPa)
ΔK = the alternating stress intensity factor ($MPam^{1/2}$)

From their results, and a similar investigation of Ti-6Al-4V by Yoder *et al.* [161], Wanhill *et al.* concluded that the fatigue crack growth curve gradient transition probably occurred; (i) as a consequence of the maximum extent of the cyclic plastic zone becoming equal to, and exceeding, the average colony size and (ii) a change from a structure-sensitive facetted and branched mode of crack growth to a continuum-mode of crack growth which was characterised by fatigue striations. Similar conclusions to (i) have also been made by Thompson *et al.* [207] in Ti-6Al-4V and by Gardiner [102] in IMI 550. Thompson *et al.* [207] used a similar formula to equation 7.4 with a pre-multiplying factor of 0.106 which was calculated for Ti-6Al-4V by Irving and Beevers [209].

Using equation 7.4 and the results in Table 6.3, the average cyclic plastic zone sizes in the present investigation are 46 μm, 44.4 μm and 43.3 μm for tests at σ_{max} = 95%, 90% and 85% of the 0.2% P.S., respectively. If the pre-multiplying factor of Irving and Beevers [209] (0.106) is used, values of 37.3 μm, 35.6 μm and 34.8 μm are obtained for the same respective σ_{max} values. The average colony size measured in IMI 834 is 35 ± 16 μm (section 4.2), whereas the average transformed-β grain size is 66.4 ± 30 μm. It therefore seems probable that the transition in macroscopic fractographic appearance in four point bend specimens of IMI 834 occurs when the reverse plastic zone size equals, or exceeds, the average colony size of the transformed-β. This is clear evidence

that it is the colony size which is important for fatigue properties, rather than the prior-β grain size.

By tracing back the river markings, which are a feature of the flat facets in the pre-transition region of the fracture surfaces, two fatal crack origins were identified using S.E.M. (Figure 6.12 and Figure 6.13). Both origins occurred in primary-α grains and contained similar features, namely, very smooth areas of about 5 μm in radius. The smooth areas imply that the fatigue cracks initiated crystallographically across a slip plane. The path of the cracks did not deviate from this slip plane over the radius of the smooth regions. Beyond these smooth regions river markings were produced where the crack front changes to a parallel slip plane due to imperfections in the crystal lattice.

Elliptical features of between 2 and 3 μm in length occurred close to the centre of both crack origins. It was found that these features were complementary on matching fracture surfaces (Figure 6.13). It is suggested that an alternative crack path may have been followed in these regions by the linkage of more than one crack on parallel planes in the primary-α. T.E.M. observations that may explain this behaviour are discussed later (section 7.4.3).

7.4 T.E.M. OBSERVATIONS OF FATIGUED MATERIAL

The stress profile (from the fatigue surface to the neutral axis) of a four point bend specimen at below the 35.0 x 10.0 mm area of maximum stress is shown in Figure 7.4. Cross-sectional thin foil observations of the fatigued microstructure were made within 100 μm of the surface. At this depth there is a small reduction in the maximum stress of 16.5 MPa compared to that at the fatigue surface (for specimens tested at 95% P.S., see Figure 7.4). Thus, differences in the deformation behaviour over this depth range are likely to be

negligible.

7.4.1 Slip Systems in Primary-α Grains

In this section the results of T.E.M. observations from back-thinned and cross-sectional foils are discussed. The foils were taken from specimens which were fatigue tested with a maximum stress of 95% or 100% of the 0.2% P.S.

In the present study, intense planar slip bands across the primary-α grains were characteristic of fatigue damage accumulation in IMI 834 (section 6.5.5). Basal (0001) slip was found to be the preferred deformation mode in these grains and secondary slip on prism $\{10\bar{1}0\}$ planes and pyramidal $\{10\bar{1}1\}$ planes was observed. Occasionally, $\langle \underline{c} + \underline{a} \rangle$ slip was found in primary-α grains close to the fatigue surface (see section 7.4.2). The preference for slip on the basal planes, rather than the prism planes, in primary-α grains of IMI 834 is due to the high Al_e in these grains (section 7.1.1). The relatively high interstitial content of the primary-α grains also contributes to this slip preference (section 7.1.1). Observations which support these preferences are discussed in this section and are substantiated further in section 7.4.1.1 by the influence of oxygen and aluminium on the nature of slip in titanium alloys.

Many investigations of fatigue crack initiation and short crack growth in titanium alloys having a duplex microstructure found that the crack nucleation sites were associated with slip bands in the primary-α phase [21, 135, 165, 166, 168, 169]. However, observations of the slip systems responsible are less commonly reported.

The majority of observations on slip systems in primary-α grains were made in α-titanium alloys. The crystallography and deformation modes in α-titanium were determined by Churchman [109] and other workers [110-112] (section 2.4). From the results of many studies on the

deformation modes of single crystals and polycrystals of α-titanium at low temperatures (section 2.4.3) the principal deformation mode in titanium was established as prismatic $1/3\langle 11\bar{2}0\rangle\{10\bar{1}0\}$ slip [100, 109, 111, 112, 124-128, 155, 159, 210, 211]. The stresses required to activate the different slip systems in hexagonal metals are very dependent upon the orientation of the stress axis (equation 2.6) and the critical resolved shear stresses (CRSS) of the different slip systems. In commercially pure titanium with a low interstitial content, there is a preference for prismatic slip due to the lower CRSS required to activate slip on the prism planes (see Table 2.7 and Figure 2.12). The results of many studies on the deformation of α-titanium, particularly those of Conrad and co-workers [100] (Figure 2.12, section 2.4.3), indicate that the ratio of CRSS for basal and prism slip decreases with an increase in the interstitial content (even though the absolute values of both increase). At interstitial contents approaching 1 at%, the curves of CRSS for basal and prism slip converge and, above this level, slip on the basal plane becomes the preferred deformation mode [100] (Figure 2.12). The ordering of oxygen in titanium has also been used to explain the changes in the dominant slip mode from prismatic slip to pyramidal slip in some commercial titanium alloys [100].

Blackburn and Williams [118] studied the dislocation arrangements in deformed specimens of titanium containing up to 25 at% aluminium and 0.3 to 0.6 at% oxygen (see section 2.4.4). Prismatic slip was found to be the preferred mode at low strains but at higher strains, slip on pyramidal $\{10\bar{1}1\}$ planes and basal (0001) planes was observed [118]. Thus, the CRSS for prismatic slip is lower than that for pyramidal and basal slip in these alloys. Jones and Hutchinson [121] reported that <a> type basal, prismatic and pyramidal slip occurs with almost equal ease in Ti-6Al-4V, suggesting that the CRSS's required to activate the three slip systems are similar in this alloy.

Evidence by Paton and Spurling [212] indicates that the aluminium content of titanium alloys also influences the CRSS's of the slip systems. It was found that basal slip becomes equally favoured to prismatic slip when the aluminium content is increased to 6.6 wt%. In support of this observation, a preference for basal slip in transformed-β grains of the high Al*, near-α titanium alloy, IMI 829, has been found by Woodfield *et al.* [64] and White *et al.* [178] (see section 7.4.2).

7.4.1.1 Effect of Aluminium and Oxygen Content

In view of observations made in the literature, the combined effects of; (i) a very high Al* (9.14 wt%), (ii) the occurrence of the ordered phase (Ti_3Al) and (iii) the oxygen content (Table 7.1) of IMI 834 are considered to be responsible for the intense planar slip bands observed on the basal planes of primary-α grains in the present study.

Williams *et al.* [118, 129] found that the principal parameters affecting the nature of slip in α-titanium were the aluminium content, oxygen concentration and the grain size. The effect of aluminium additions was investigated [118]. At low aluminium contents (0 to 5 at%), the dislocations in deformed specimens formed a cellular structure and as the aluminium content increased, a more homogeneous distribution of dislocations was observed (section 2.4.4). At greater than 10 at% (6 wt%) aluminium, very planar arrays of dislocations were observed with a consequent reduction in cross-slip [118]. The widths of the planar slip bands narrowed as the aluminium content increased further and were also narrowed by the formation of the ordered α_2 phase or Ti_3Al precipitates (section 2.2.5.1). In addition to the effects of aluminium, increases in oxygen concentrations promoted planar slip in the α phase [129]. Lim *et al.* [213] investigated the effect of α_2 and oxygen on the mechanical

behaviour of Ti-8Al. The precipitation of α_2 led to a marked increase in the tendency for planar, sharply defined slip bands. This in turn produced internal stress concentrations at arrested slip bands (*e.g.* at grain boundaries) and increased the propensity for cleavage fracture. Increases in the oxygen content of titanium-aluminium alloys stabilised the α_2 phase which increased the brittleness. It was suggested that oxygen partitioned preferentially to the α_2 phase in $\alpha + \alpha_2$ alloys [213]. The effect of oxygen on the slip planarity was suggested to be approximately ten times stronger than that of aluminium [129].

Many examples of paired dislocations were also found in the present study (see section 6.5, Figures 6.17, 6.22, 6.26 and 6.52). The spacing of these dislocation pairs varied between 20 and 40 nm. A number of investigators have reported similar dislocation pairs on preferred slip bands in various titanium alloys.

In a study of the deformation modes operating in titanium-aluminium alloys, Blackburn and Williams [118] found dislocation pairs at the head of planar arrays on the prism planes. The dislocation pairs were found only in alloys of greater than 6 wt% aluminium and their spacing was said to depend upon the aluminium content and the size of Ti_3Al particles [118]. Vijayakar [214] found that dislocation pairs approximately 30 nm apart were associated with short range order of Ti_3Al in planar slip bands lying on the prism $\{10\bar{1}0\}$ planes of Ti-8Al-1Mo-1V. In a more detailed study of titanium-aluminium alloys, Gysler [215] observed that the separation of the leading pair of dislocations was approximately 20 nm and that the spacings increased with distance from the head of the pile-up until only single dislocations were observed. The transition from paired to single dislocation configurations, indicated that the Ti_3Al particles had totally sheared by a particle cutting mechanism proposed by Lütjering [216]. This mechanism allows an estimate of

the ordered particle size to be made [215].

In primary-α grains of Ti-6Al-4V which had been aged for 67 hours at 350°C and strained by 2%, Welsch *et al.* [197] observed dislocation pairs, on the pyramidal ($\{01\bar{1}1\}$) planes, which were separated by approximately 25 nm. The dislocation pairing suggested that short range order was present in the primary-α grains, but surprisingly, no evidence of α_2 formation was found, even after the 67 hour ageing treatment. This observation suggested that titanium and aluminium were immobile at 350°C [197]. The diffusion of oxygen in titanium was possible at 350°C and it was concluded that oxygen and not α_2 was responsible for the short range order (*i.e.* dislocation pairing) [197].

Liu and Welsch [217] investigated the dislocation structure formed in the alloy Ti-6Al-2V with oxygen concentrations of between 0.65 and 0.07 wt%. The alloy was solution treated, quenched and some specimens were aged, prior to straining by 2%. Evidence of oxygen order was found in the as-quenched 0.65 wt% oxygen alloy as <**a**> type superdislocation pairs formed approximately 10 nm apart. The two member dislocations of superdislocations had identical Burgers vectors and, as a consequence, the spacing between them did not change with the reversal of **g**. In the aged specimens containing 0.65 wt% oxygen, no superdislocations were found. It was suggested that oxygen had partitioned to the octahedral sites in the Ti_3Al formed during ageing. This partitioning possibly caused a reduction in the bulk oxygen concentration and was said to explain why no superdislocations were observed in the aged material [217]. In the alloy with 0.07 wt% oxygen some dislocation pairs were observed. However, because the distances between the members of the dislocation pairs changed with the reversal of **g**, these dislocation pairs were dipoles (with opposite Burgers vectors) and not superdislocations.

The paired dislocations observed in the present investigation are an indication of ordering in the primary-α grains of IMI 834. It is proposed that they are superdislocations formed by a combination of aluminium and oxygen ordering which is enhanced by the segregation of these elements to the primary-α during α+β processing (section 7.1.1). The addition of carbon to IMI 834 was advantageous for the reasons listed in section 7.1.1. However, the segregation of this α-stabiliser to the primary-α phase will increase the Al* in these grains probably enhancing the ordering process by a similar mechanism to oxygen.

The tendency for planar slip to occur in the primary-α grains suggests that cyclic softening has occurred which is associated with the passage of superdislocation pairs shearing the coherent Ti_3Al particles. The continued shearing of the particles by subsequent superdislocations destroys the particles and reduces the dislocation glide stress on the slip plane, consequently causing slip to concentrate preferentially on the same basal slip plane.

7.4.1.2 Effect of Silicon Additions

In the present investigation, the effect of silicon on the precipitation of Ti_3Al and hence the planarity of the basal slip in the primary-α could not be established. However, the effects of silicon on the ordering and ductility of IMI 829 (Ti-5331-S) were compared to a silicon-free experimental alloy Ex-Ti-5331 with a similar Al* to both IMI 829 and IMI 834 [44, 64]. Despite the similar Al*, the extent of ordering in IMI 829 which was aged for only 100 hours at 575°C was found to be the same as that in Ex-Ti-5331 after 1000 hours at 575°C. In contrast to IMI 829, ageing Ex-Ti-5331 for 1000 hours at 575°C caused no observed ductility loss. Woodfield *et al.* [64] argued that the precipitation and fracture of silicides effectively enhanced the ordering process and reduced the ductility of IMI 829. Their work suggested

that, in addition to the Al*, the silicon content of the alloy was important in determining the degree of ordering. Additional qualitative evidence given by Lütjering and Weissmann [216] showed that silicon atoms may precipitate within the Ti_3Al particles in ternary Ti-Al-Si alloys. Further work is required to establish whether the addition of silicon enhances the ordering process in IMI 834.

7.4.1.3 <c + a> Slip

In the present investigation, slip with a Burgers vector of the <c + a> type was occasionally observed in primary-α grains adjacent to the fatigue surface. It has been shown in the literature that <c + a> slip can play a major role in the plastic deformation of single crystals of titanium [119], polycrystalline α-titanium [118, 122] and Ti-6Al-4V [32, 120, 121]. Blackburn and Williams [118] determined that <c + a> slip of the type $1/3\langle 11\bar{2}3\rangle\{10\bar{1}1\}$ occurred as planar groupings in titanium-aluminium alloys containing up to 17 at% aluminium. The individual dislocations were more irregular than <a> type dislocations, often being paired and were observed to interact with <a> type dislocations [118]. Similar dislocation pairing and interactions with <a> type dislocations on the basal plane were observed in the present study of IMI 834 (Figure 6.30B). Blackburn and Williams suggested that such interactions may arise as a result of the reaction:

$$1/3[11\bar{2}3] + 1/3[11\bar{2}\bar{3}] = 1/3[11\bar{2}0] \qquad (7.5)$$

Analysis of the CRSS for <c + a> slip was made by Bowen [32] and Jones and Hutchinson [121]. Bowen determined that the CRSS for <c + a> slip was four times that for <a> type slip in Ti-6Al. However, Jones and Hutchinson determined the CRSS for <c + a> slip to be a factor 1.5 times that of <a> type slip in Ti-6Al-4V. The comparatively easy operation of <c + a> slip in Ti-Al-4V was said to limit the potential for texture strengthening

in this alloy [121].

A number of factors may have contributed to the occurrence of the <c + a> slip observed in the present investigation. During fatigue, the fatigue surface is subjected to the highest stresses in the specimen and therefore the grains adjacent to the fatigue surface receive the stresses likely to reach the CRSS necessary for <c + a> slip. In the two examples where <c + a> slip was found in the present study, the basal planes occurred at an angle of 20° to the fatigue surface (Figures 6.30A and 6.30B). The resolved shear stress acting on the basal planes was low in these grains and the occurrence of basal slip alone was insufficient to accommodate the imposed stresses. The orientation of these grains was such that the CRSS for <c + a> slip was attained. In one of the grains of interest, illustrated in Figure 6.30A, a contribution to the stresses required to activate the <c + a> slip may have come from the intense basal slip which had built up at the primary-α/transformed-β grain boundary in an adjacent transformed-β colony (see Figure 6.44). The basal slip pile-up caused a stress concentration in the primary-α which increased the imposed stresses in this grain. <c + a> slip was, however, a minor feature of the fatigue damage accumulation in the present study of IMI 834.

7.4.1.4 Effect of CRSS and Grain Orientation

A preference for slip on the basal plane of primary-α grains was found due to the high Al* present in these grains (discussed in section 7.4.1.1). However, the observation that basal slip occurred even where the resolved shear stress was low, was surprising. Two measurements were made in each primary-α grain where slip was observed (section 6.5.2.3): (i) The orientation of the grain was determined at 0° tilt by T.E.M. From this orientation, the angle which would be required to tilt the basal slip to an edge-on position was calculated (section 6.5.2.3, Table 6.7). (ii) The angle between the slip band

and the fatigue surface was also recorded. Figure 7.5 schematically shows these angles which are hereafter termed ψ and θ, respectively. Figure 7.6 shows the observed orientation of the basal slip with respect to the fatigue surface and secondary slip systems. Secondary slip on the prismatic or pyramidal planes was found in grains close to the fatigue surface when the θ was > 70° (section 6.5.5). When θ was approximately 20°, $\langle \underline{c} + \underline{a} \rangle$ slip was found to operate in some grains adjacent to the fatigue surface. At 20° < θ < 70°, basal slip was the only deformation mode observed. The significance of these observations is discussed here with reference to the grain orientations.

The dominance of basal slip at 30° < θ < 70° can be explained by comparing the CRSS's of the different slip modes. The CRSS for basal slip has the lowest of all the slip systems in the primary-α grains. At 30° < θ < 70°, a high resolved shear stress for at least one of the slip directions ($\langle 11\bar{2}0 \rangle$) operates on the basal plane. Although the Schmid factor of other slip systems (prismatic/pyramidal) may be favourable in these grains, deformation on these slip systems does not occur because a slip system with a lower CRSS (basal slip) is able to operate. Thus, only basal slip is expected to operate at these angles.

In several circumstances where θ was close to 90°, the value of ψ was found to be low. For example, in Figures 6.25 and 6.26, basal slip occurred at close to 90° to the fatigue surface and the value of ψ was 15°. This gave a value of ϕ of close to 15°, where ϕ is the angle between the applied stress direction and the normal to the applied stress. Under such circumstances the resolved shear stress on the basal plane is expected to be very low. In the primary-α grain of interest, pyramidal slip at 45° to the fatigue surface also occurred. It is considered that the plane stress condition of the free surface has promoted basal slip even though the resolved shear stress

on this plane is very low and that the CRSS for slip on the pyramidal plane is also reached since the Schmid factor for slip on this plane is close to its maximum.

In some primary-α grains adjacent to the fatigue surface, where $\theta \leq 20°$ (Figures 6.30A and 6.30B), <c + a> slip was found. The fact that basal slip also occurred in these grains suggests that the CRSS for basal slip is much lower than that for <c + a> slip. It is considered that the low CRSS for basal slip results from the high overall Al*, the partitioning of α-stabilising elements to the primary-α (section 7.1.1) and, importantly, the formation of Ti_3Al and the segregation of interstitials to these precipitates. The effect of this ordering is sufficient to cause the formation of superdislocations. Slip on the basal planes is therefore highly planar in nature and restricted to a small number of planes in each primary-α grain.

The effect of slip on basal cleavage planes at angles approaching 90° to the fatigue surface is highly significant in the consideration of fatigue crack initiation. The resolved tensile stress on such planes is high. The combination of a high dislocation density on a limited number of basal planes, with a high resolved tensile stress may provide a clear mechanism for fatigue crack initiation. As θ and ψ approach a maximum resolved shear stress (*i.e.* $\theta = 45°$), the resolved tensile stress falls, and the dislocation density is likely to increase. Unfortunately it is not clear which mechanism is more likely to initiate a crack; (i) a plane with θ close to 90° and ψ close to 0°, with a resolved tensile stress close to σ_{appl}, or (ii) a plane with θ closer to 45° where the dislocation density and resolved shear stress are high, but the resolved tensile stress is lower. It is probable that the plane which ultimately cracks will involve a combination of these events (*i.e.* basal slip bands at $45° < \theta < 80°$), and may require an additional factor to activate a fatigue crack. For example, a given

grain may have a greater slip length (and hence a higher dislocation density), a particularly potent dislocation barrier such as a primary-α/transformed-β grain boundary, a silicide or β particle, or an especially high Al*. The above conditions suggest that a strong texture may have a significant effect on the fatigue behaviour.

7.4.2 Slip Systems in Transformed-β Grains

Both prism (1/3<11$\bar{2}$0>{10$\bar{1}$0}) and basal (1/3<11$\bar{2}$0>(0001)) slip were found as the preferred slip systems in the transformed-β colonies of IMI 834. The two slip systems were observed with about equal preference. The basal slip was found to occur across the widths of the transformed-β colonies with little or no resistance from the retained-β along the α-platelet boundaries, and was arrested at colony or grain boundaries. Some restriction to the dislocation motion in prism slip bands was observed at the α-platelet boundaries (Figures 6.40 and 6.41B), however, the major barriers to prism slip were also the colony or transformed-β grain boundaries. Similar barriers to the progress of slip bands in the transformed-β have been widely reported [24, 38, 42, 64, 178].

Due to the increased interest in the more creep resistant, high temperature, β-processed, near-α titanium alloys over the more established, duplex microstructured, α+β titanium alloys, a number of recent investigations have studied the slip characteristics of the transformed-β grains in near-α titanium alloys.

The observations in the present work have shown; (i) that an inhomogeneous distribution of deformation both within and between thin foils occurred, (ii) a variation of dislocation density in the transformed-β grains such that some colonies were highly deformed whereas others were completely undeformed, (iii) a higher dislocation density in transformed-β grains closer to the fatigue surface was observed, (iv) that the most commonly observed slip

systems in the transformed-β were 1/3<11$\bar{2}$0>{10$\bar{1}$0} and 1/3<11$\bar{2}$0>(0001) and (v) that a quantitative measurement of the dislocation density was difficult due to the inhomogeneous distribution of deformation in the transformed-β grains. These observations are in agreement with those made by White *et al.* [178] in a T.E.M. study of the damage accumulation mechanisms in β-processed IMI 829 (fatigued in tension at σ_{max} = 800 to 900 MPa, R = 0, f = 10 cpm).

Woodfield *et al.* [64] observed the damage in IMI 829 which had been tensile tested in various β-processed, as-quenched and aged conditions. In both the unaged and aged materials, the most active slip system was of the type 1/3<11$\bar{2}$0>(0001), followed by 1/3<11$\bar{2}$0>{10$\bar{1}$0}. Similar preferred deformation modes were found in both Ti-11 and IMI 685 [42]. <$\underline{c}$ + $\underline{a}$> slip of the type 1/3<11$\bar{2}$3>{10$\bar{1}$1} was observed in the transformed-β grains of IMI 829 [64], IMI 685 [42] and Ti-6Al-4V [24]. In the present investigation <$\underline{c}$ + $\underline{a}$> slip is observed in occasional, suitably orientated primary-α grains near the fatigue surfaces (section 7.4.1.3). However, despite no <$\underline{c}$ + $\underline{a}$> slip being found in the transformed-β in the present study, such slip may occur in suitably orientated colonies. <$\underline{c}$ + $\underline{a}$> slip would be difficult to image because of the high dislocation density present in the transformed-β grains.

The occurrence of both prismatic and basal slip in the transformed-β grains of IMI 834 suggests that the CRSS's for slip on these planes are similar in the transformed-β. Slip in these grains is also more homogeneous in nature than in the primary-α. These observations suggest that the Al* in the transformed-β is lower than in the primary-α. This is confirmed by the difference in the reflections from Ti_3Al which were much more intense in the primary-α than in the transformed-β (section 4.4.1). STEM analysis of IMI 834 by Shollock [191] (section 7.1.1) confirmed a higher Al* in the primary-α compared to the

transformed-β. It is also suggested in the present work (section 7.1.1) that the diffusion of interstitial elements to the primary-α phase will also increase the Al* of the primary-α phase. Whether prism or basal slip operates in a given transformed-β grain is probably more dependent upon the grain orientation than in the primary-α.

7.4.3 Damage Accumulation and Microcracking

Fatigue crack initiation in the present study was found to occur preferentially in the primary-α phase, in agreement with the observations in similar duplex microstructures [168, 169]. Crack initiation was associated with the development of intense planar slip bands in grains favourably orientated with respect to the applied stress direction (section 6.3.2.1). Four microcracks were observed in thin foils (section 6.5.4) which were wholly contained in the thin area, and were found in foils where the hole was free from cracking. The microcracks are considered unlikely to be a result of the thinning process, however, the possibility that the cracks opened up as a result of the residual stresses and the removal of surface constraints during foil preparation cannot be totally ruled out.

It is well established that the fatigue crack initiation and early fatigue crack growth in high temperature titanium alloys occurs in a crystallographic manner along intense planar slip bands inclined to the stress axis [40, 42, 104, 162, 165, 168, 169, 218]. Crack or slip band arrest is most frequently found at grain boundaries where slip transferral into adjacent grains/colonies is not possible due to the high angles created at the grain boundaries. In β-processed microstructures, intense slip bands were observed across colonies of similarly orientated α-platelets [9, 17, 38, 40, 42, 43, 73, 95, 164] and the length of slip bands was controlled by the effective colony size in the alloy (section 2.5.6.3)[43].

Although the retained-β phase at the α-platelet boundaries offered some resistance to the dislocation motion in the α phase, it did not act as a major barrier to slip, except in slow cooled microstructures (section 2.5.6.3). In duplex, α+β processed microstructures the planar slip, on which the majority of fatigue cracks initiated, occurred across the width of primary-α grains [21, 135, 165-169].

As a result of the crystallographic mechanism of crack initiation and early crack propagation, the fracture surfaces close to the crack origins of failed specimens have been characterised by several authors as having smooth, transgranular cleavage-like facets on the scale of the primary-α/colony size of the alloys [40, 52, 104 164, 206]. S.E.M. studies of the fracture surfaces have determined that the initial fatigue cracks occurred on, or near to, the basal (0001) plane [66, 104, 164, 180, 219-221]. The observation of cracking on apparently irrational planes close to (0001), such as $\{10\bar{1}7\}$ and $\{10\bar{1}8\}$ [23, 161, 222], was explained by the consequence of crystallographic cracking on a combination of (0001) and $\{10\bar{1}0\}$ planes [164].

In the present work, the path of the microcrack found in a transformed-β grain (Figure 6.45) suggests that an α-platelet or colony boundary was followed and that the crack had changed direction at slip bands or silicides in the boundary. However, because of the high density of deformation around the cracking (Figure 6.46), accurate analysis of its path was not possible.

T.E.M. observations of microcracking in the primary-α phase were more easily characterised (section 6.5.4.2). A microcrack observed in a back-thinned foil occurred on the basal plane of the primary-α (Figures 6.48 to 6.50). The crack plane was determined by tilting the foil so that the basal dislocations at the crack tip were imaged edge-on when the crack was imaged edge-on. The analysis of

selected area diffraction patterns under this condition confirmed that the cracking occurred on the basal plane. The superdislocations at the crack tip, and the presence of extra reflections in the diffraction pattern, Figure 6.51, indicate that short range order is present in the primary-α grain (section 7.4.1.1). No evidence of any slip band pile-up associated with the crack could be seen, however, the foil was back-thinned and therefore such information may have been removed during electropolishing.

Two parallel microcracks were found in a cross-sectional thin foil at approximately 15 μm below the fatigue surface (Figure 6.53). The microcracking occurred parallel to planar slip bands at 75° to the fatigue surface in a primary-α grain. Analysis of the microcracks under g = [0002] (Figure 6.55) showed that they were edge-on under this condition and thus occurred on the basal plane. The longer of the two microcracks was arrested at the tip closest to the fatigue surface by a β phase particle. It it is suggested that the elliptical features observed at the crack initiation sites by S.E.M. (Figures 6.12 and 6.13) may have formed by the linkage of two cracks on the same plane to avoid a β phase particle in the primary-α. This is therefore evidence for cracking on parallel basal planes in the primary-α, however the possibility of crack linkage remains unresolved. The microcracking observed by T.E.M. further substantiates the optical and S.E.M. observations (sections 7.3.2 and 7.3.3) that short cracks initiate along planar slip bands in the primary-α and shows that these initial cracks occur on the basal planes. In addition, the cracking occurs at 75° to the fatigue surface; this agrees with the suggestion that a high resolved tensile stress may be required for fatigue crack initiation (section 7.4.1.4).

7.4.3.1 Mechanisms of Fatigue Crack Initiation

Fatigue crack initiation in pure metals and alloys occurs at microscopic sites of high local plastic strain

concentration such as slip bands, twin boundaries, grain boundaries and inclusions [135]. In high temperature titanium alloys, crack initiation on slip bands is most widely reported. However, existing evidence of crack initiation mechanisms reported in the literature have largely been indirect. Many observations have been made using surface replication techniques and S.E.M. studies and as such, these fail to differentiate between surface and sub-surface features.

The important parameters which control the onset of fracture in α phase alloys were those which control the character of the slip, *i.e.* the aluminium and oxygen equivalents (section 7.4.1.1), and those which control the pile-up length, *i.e.* the grain size [129]. Planar slip in the primary-α phase of the α-alloy Ti-8.6% Al led to relatively intense dislocation pile-ups at the grain boundaries [129]. When the local stress reached a critical value [223], crack initiation occurred by grain boundary cracking and crack growth along slip bands [129]. It was suggested that, if the density of dislocations was not high enough for crack propagation along the slip bands, then the cracks propagated along the grain boundaries [129]. Similar crack nucleation sites were found in low temperature α+β processed Ti-17 [135]. Crack initiation along slip bands in the primary-α phase was considered to represent situations where the resolved shear stress along them was high. Conversely, crack initiation along the grain boundaries suggested that the resolved shear stress along the slip bands was low [135]. However, these suggestions were made from S.E.M. observations of plastic replicas and, as such, the resolved shear stresses along the slip bands could not be determined. A more conclusive determination of the slip band orientations with respect to the fatigue surface and the resolved shear stresses on these bands has been obtained from cross-sectional thin foil observations in the present investigation (section 7.4.1.4).

Fatigue crack initiation along slip bands in the primary-α grains of Ti-6Al-4V was observed by Brown and Smith [27]. Detailed S.E.M. studies of surface replicas indicated that a single region of localised slip of less than 3 μm in length initiated a crack in the α phase. The slip was located adjacent to a β particle and neither the decohesion of the α/β interface nor the failure of the β particle were responsible for the fatigue crack initiation. A mechanism of crack initiation was proposed [27]: Dislocations in a slip band in the primary-α phase piled up against a β particle. When the stresses at the head of the pile-up reached a sufficient magnitude, a crack initiated and grew back along the plane of weakness represented by the slip line. Figures 6.12 and 6.53 provide more direct evidence of such a mechanism than results from the S.E.M. of surface replicas which cannot differentiate between surface/sub-surface activity. From the evidence obtained in the present investigation, it is likely that a similar mechanism of fatigue crack initiation may have occurred in the primary-α grains of IMI 834 (see section 7.5).

Large shear offsets at the α-platelet boundaries of β-processed IMI 685 have been reported [42, 73, 224] and have been attributed to the differences in deformation characteristics of the α and β phases [224]. Shearing on either the basal [42, 56] or prismatic [42] slip planes was observed and the offset produced depended upon the number of pile-up systems [42]. If the slip band density was high, up to ten pile-up systems per micron were observed and the shear was divided among them producing only a small amount of shear on each band. The shear produced by an isolated band was more pronounced and represented the passage of hundreds, perhaps thousands of dislocations [42]. Such shear offsets provided points for void nucleation [73, 224], the growth of which led to fatigue crack initiation along the α-platelet boundaries [224] or along slip bands [42, 56] in the transformed-β. In a T.E.M. study of the room temperature tensile

properties of tensile tested IMI 829 (β-processed air cooled or oil quenched and aged at 575°C for 1000 hours) slip bands were observed to intersect with silicide particles which had precipitated on the α-platelet boundaries [64, 66]. In regions where slip bands intersected with silicide particles, cracking or voiding occurred at the matrix-silicide interface. It was suggested that fracture of the silicides occurred when the fracture stress was exceeded at the slip band with the longest dislocation pile-up length. Once a particle had fractured, it was argued that slip on the same plane continued until a second silicide particle was encountered. Since the slip band was then longer, the second particle was subjected to a higher stress and consequently fractured more readily. As a result, the strain became highly localised leading to an overall loss in ductility. It was suggested that continued basal slip across a colony would result in the growth of these cracks or voids with consequent fracture on the basal plane, giving rise to the crystallographic facets which were observed in the S.E.M. The linkage of cracks initiated on parallel (0001) planes in a colony was suggested to explain why the facet plane analysed in the S.E.M. often deviated from the expected (0001) plane [64]. In a fractographic analysis of β-processed IMI 685, Hoeppner [220] also found that silicide precipitation promoted crack initiation.

The silicide particles at the α-platelet boundaries in the present study of IMI 834 (aged for 2 hours at 700°C) were < 0.3 μm in length and neither slip band pile-ups or shearing of the silicide particles was observed. It is unlikely that fatigue crack initiation occurs at the silicide particles in α+β processed IMI 834 unless the material is aged for much longer times to permit the growth of the silicide particles. The grain boundaries or boundaries between colonies of high misorientation are the most probable sites for crack initiation in the transformed-β, however, this mode of crack initiation is

secondary to crack initiation in the primary-α, discussed in section 7.5.

7.5 FATIGUE CRACK INITIATION IN IMI 834

In the present investigation it is proposed that fatigue damage accumulation in IMI 834 leads to a preferred crack initiation mechanism on basal slip bands in primary-α grains. The occurrence of such planar slip in the primary-α is influenced by contributions from a number of factors including the interstitial and aluminium content (section 7.4.1.1) and grain orientation (section 7.4.1.4).

Short range ordering of Ti_3Al in the primary-α grains causes the strain in these grains to become very localised. Intense slip bands in the primary-α arise due to the shearing of Ti_3Al particles by moving superdislocation pairs on the basal planes. The successive shearing of the small particles leads to their breakdown and gives rise to large dislocation pile-ups at the primary-α grain boundaries or at a barrier such as a β particle.

If the dislocation pile-ups occur at a high angle to the fatigue surface (*i.e.* θ = close to 90°) then the tensile stresses acting to open up a crack along the slip band are high (see section 7.4.1.4). Alternatively, if two similarly orientated primary-α grains are crossed by the slip band then the length of the dislocation pile-up is effectively doubled (see Figure 6.12), thus the stresses tending to open up a crack along the slip band are significantly increased. Both these cases are illustrated schematically in Figure 7.7.

When the stresses at the head of the pile-up reach a sufficient magnitude, it is suggested that a crack initiates and grows back along the plane of weakness represented by the slip band. This condition is most likely to be satisfied if two adjacent primary-α grains,

at or close to the fatigue surface, are both orientated such that the angle of the basal slip is between 45° and 80° to the fatigue surface.

The proposed fatigue crack initiation mechanism requires that the crack initiates at a barrier to dislocations (*e.g.* a grain boundary, silicide or β particle). This suggests that crack initiation will occur at a subsurface site and that the crack will propagate towards the fatigue surface. No evidence was found in the present investigation for a surface intrusion/extrusion mechanism of crack initiation. Such a mechanism is promoted by the formation of dislocation dipoles at the edge of a persistent slip band (P.S.B.) (see section 2.5.5, and references [136-138, 141-143, 147-151]). The planar slip bands observed in the present study were widely spaced and no evidence of dipoles within them was found. Thus P.S.B. formation does not play a significant role in the mechanism of fatigue crack initiation in IMI 834.

The improvements in the fatigue performance of IMI 834 which result from an increase in the yield strength and a decrease in the grain size compared to other near-α alloys are off-set by the high Al_e, and hence basal slip planarity in the primary-α grains.

CHAPTER EIGHT

CONCLUSIONS

Microstructure

* The lattice parameters for titanium in the alloy IMI 834 were determined by X-ray diffraction and confirmed by T.E.M. diffraction pattern measurements to be $\underline{a}$ = 0.2952 nm and $\underline{c}$ = 0.4686 nm for the α phase and $\underline{a}$ = 0.3264 nm for the retained-β phase.

* The α-platelet boundaries of the transformed-β colonies contain thin, discontinuous films of the retained-β phase. A high dislocation density was observed in the vicinity of the α-platelet boundaries which accommodated the lattice mismatch generated between the α and retained-β phases when the material was oil quenched.

* Silicides of the S_2 type, $(TiZr)_6(SiSn)_3$, occurred on α-platelet, colony and grain boundaries and occasionally on dislocations within the α-platelets. The following orientation relationship between the silicides and α-titanium was determined:

$$[01\bar{1}1]_\alpha // [\bar{2}110]_s \; ; \; (\bar{2}110)_\alpha // (01\bar{1}0)_s$$

* The primary-α grains in unfatigued foils were usually found to contain a low density of dislocations. However, high dislocation densities in the form of hexagonal dislocation arrays and sub-grain networks were occasionally observed. These were considered to have formed during the initial forging of the compressor disc.

* The occurrence of the ordered phase, Ti_3Al, in the primary-α grains of IMI 834 was established by the presence of additional reflections in diffraction patterns imaged from zone axes. The presence of Ti_3Al was not detected in the majority of transformed-β grains.

* A tentative suggestion of the preferred texture in the compressor disc section has been obtained using X-ray diffraction. It is proposed that the basal planes preferentially face at or between the tangential and radial directions in the compressor disc according to Figure 4.6. A low volume fraction of grains were orientated such that the basal planes within them faced in the axial direction.

Artefactual Interface Phase

* A face centred cubic interface phase with $\underline{a}$ = 0.434 ± 0.004 nm was identified to form along some of the α-platelet boundaries in thin foils prepared by techniques involving ion-beam milling. No evidence of any interface phase was found in foils which had been electropolished. This is in conflict with observations published in the literature [85]. It is proposed that water may have been an impurity in the argon gas used during ion-beam milling and that hydrogen ions derived from the water may be responsible for the formation of the interface phase.

* From observations of cross-sectional thin foils, it is postulated that the nickel plating process had caused hydrogen absorption into the plated IMI 834. As the hydrogen content increased: (i) An fcc interface formed along the α-platelet boundaries. (ii) An acicular phase about 0.1 μm in width occurred in specific crystallographic orientations across the α-platelet width. (iii) At high hydrogen concentrations, the entire microstructure was altered.

Fatigue Crack Initiation

* Optical and scanning electron microscopy revealed that fatigue crack initiation in IMI 834 occurs preferentially in the primary-α phase and is associated with the development of intense slip bands across favourably orientated primary-α grains.

* The results of the present investigation suggest that it is less tortuous for a crack to propagate from an initiating primary-α grain if the α-platelets in adjacent transformed-β colonies are orientated such that the crack can follow a path at 90° to the α-platelet boundaries, *i.e.* propagate along a basal plane in the transformed-β phase.

* Short fatigue crack growth in IMI 834 was shown to be facetted, with initiation sites at, or just below the fatigue surface. A macroscopically visible transition in fracture appearance was noted on all failed test specimens. The transition occurred when the reversed plastic zone size of the material became equal to, or exceeded, the transformed-β colony size.

* Cross-sectional thin foils were successfully prepared from fatigued specimens. The technique enabled the build up and relative depth of damage below the fatigue surface, and the orientation of slip bands with respect to the fatigue surface, to be observed and characterised.

* Damage accumulation in the transformed-β grains was more homogeneous in nature than in the primary-α grains. Two preferred deformation modes were found to be operative, namely, the basal $(1/3\langle 11\bar{2}0\rangle(0001))$ and prismatic $(1/3\langle 11\bar{2}0\rangle\{10\bar{1}0\})$ slip systems. The most effective barriers to slip in the transformed-β were the grain boundaries and boundaries between colonies which were orientated such that continued slip in the

adjacent colony was unfavourable. Some restriction to the motion of slip on the prismatic planes was observed at the α-platelet boundaries, however, these were not considered to be major barriers to slip.

* Intense planar slip on the basal (0001) planes was the dominant mode of deformation in primary-α grains under the testing conditions studied. Basal slip occurred on widely spaced planes with no tendency to form PSB's via numerous closely spaced planes. The preference for slip on the basal planes was caused by the high aluminium equivalent and interstitial content in the primary-α grains which reduces the ratio; $(CRSS)_{basal}/(CRSS)_{prism}$ to less than one.

* Basal slip was observed in all the primary-α grains which contained slip bands. Some of these grains also contained either prismatic $(1/3\langle 11\bar{2}0\rangle\{10\bar{1}0\})$ slip, pyramidal $(1/3\langle 11\bar{2}0\rangle\{10\bar{1}1\})$ slip or $\langle \underline{c} + \underline{a}\rangle$ slip. These secondary slip systems were found to occur when the angle between the basal plane and the fatigue surface gave rise to a low resolved shear stress on the basal plane; $\langle \underline{a}\rangle$ type slip on the prismatic and pyramidal planes was found in primary-α grains where the angle between the basal slip and the fatigue surface was $\geq 70°$ and $\langle \underline{c} + \underline{a}\rangle$ type slip was observed in grains which contained basal slip at low angles to the fatigue surface. Between these two extremes, basal slip was the only slip system observed. Thus, it appears that the critical resolved shear stress for slip on the basal planes in primary-α grains of IMI 834 is significantly lower than that for slip on the other available slip systems.

* Basal slip was found to occur when orientated at close to 90° to the applied tensile axis, i.e. when the resolved shear stress on the basal plane was very low. The resolved tensile stress on such planes would have been high, increasing the propensity for crack

initiation on these planes.

* The occurrence of paired dislocations in many of the basal slip bands was indicative of the presence of short range order (Ti_3Al) which promotes planar slip in the primary-α grains. It is suggested that the effect of Ti_3Al is enhanced by the partitioning of the interstitial elements, oxygen and carbon into the enlarged octahedral sites in the ordered phase.

* Due to the high propensity for slip to occur on the basal planes and the preference for fatigue cracks to initiate in the primary-α grains of IMI 834, it is proposed that all slip band cracking occurs on the basal planes. It is suggested that fatigue crack initiation in the primary-α phase occurs by the pile-up of dislocations on a basal plane at either the boundary between a primary-α grain and an adjacent transformed-β grain or at a β phase particle on the boundary between two similarly orientated primary-α grains. When the stresses at the head of the pile-up reach a sufficient magnitude, a crack may initiate and grow back along the plane of weakness *i.e.* the basal cleavage plane.

* Fatigue crack initiation was found to be just sub-surface. No evidence was observed for an intrusion/extrusion or persistent slip band mechanism of crack initiation.

* Crack initiation in the primary-α grains is controlled by: (i) The composition (Al* and interstitial content) of the primary-α grains. (ii) The density of dislocations on the basal planes. (iii) The effectiveness of a microstructural barrier to dislocation motion. (iv) The magnitude of the resolved shear stress on the basal planes.

CHAPTER NINE

IMPLICATIONS AND FURTHER WORK

IMPLICATIONS

Composition

The overriding factor which controls the nature of fatigue damage accumulation in IMI 834 is the aluminium equivalent, Al^*. The high Al^* (> 9 wt%) in the primary-α phase; (i) causes the formation of the ordered phase, Ti_3Al and (ii) reduces the ratio $(CRSS)_{basal}/(CRSS)_{prism}$, so that slip on the basal plane is the preferred deformation mode. The formation of Ti_3Al increases the slip planarity, the effect of which may be enhanced by the presence of interstitial elements. In order to reduce the propensity for such planar slip on the basal planes, the Al^* must be decreased by careful alteration of the alloy composition.

The exact role of carbon in IMI 834 remains uncertain, but it may affect the damage accumulation mechanisms, and thus merits further investigation.

Texture

Fatigue cracking on the basal plane may be reduced by refining the texture of the alloy so that, in service, the basal planes are orientated such that they are least likely to cause deformation. The most probable sites for fatigue failure in a compressor disc are close to the bore region where the hoop stresses are acting at a maximum. In order to minimise the propensity for fatigue crack initiation in these regions requires that the basal planes are orientated radially within the compressor disc.

SUGGESTIONS FOR FURTHER WORK

* To observe the effect of extended ageing on the distribution and size of the ordered Ti_3Al precipitates and the consequent effects this has on the deformation behaviour of IMI 834.

* To determine whether larger silicide precipitates, which may be present after extended ageing, can arrest slip in the transformed-β grains and affect the mechanism of fatigue crack initiation in the transformed-β grains of IMI 834.

* To determine the effect of different specimen orientations on their fatigue lifetimes and thus whether there is an influence of a preferred texture in the compressor disc.

* To determine the number of cycles to fatigue crack initiation of fatal cracks by taking surface replicas at appropriate intervals during fatigue cycling.

* The introduction of a dwell at maximum load into the fatigue cycle is suggested to enhance basal cleavage and crack density (section 2.5.7). It is suggested that further work should be carried out, under similar loading conditions to those studied in the present work, to observe the effects of introducing a dwell at maximum load on the fatigue behaviour of IMI 834.

CHAPTER TEN

REFERENCES

1 G. Asquith and A. C. Pickard, *Full Scale Testing of Components and Structures*, pp. 210-234. Butterworths, Sevenoaks, U.K. (1988).

2 T. W. Farthing, *Proc. Conf. Titanium '80, Science and Technology* (edited by H. Kimura and O. Izumi), Vol. I, pp. 29-37 (1980). T.M.S.-A.I.M.E., Warrendale, Pa (1980).

3 T. W. Farthing, *Proc. Conf. The Metallurgy of Light Alloys*, pp. 9-31. I.O.M. Conf. No. 20. (1983).

4 D. Eylon, S. Fujishiro, P. J. Postans and F. H. Froes, *J. Metals* **11**, 55 (1984).

5 P. A. Blenkinsop, *Proc. Fifth World Conf. on Titanium* (edited by G. Lütjering, U. Zwicker and W. Bunk), Munich, Vol. IV, pp. 2323-2338 (1984). Deutsche Gesellschaft für Metallkunde e.V., F.R.G. (1985).

6 R. E. Goosey, *Metals and Materials* **5**(8), 451 (1989).

7 R. M. Duncan, R. E. Goosey, R. H. Jeal and P. J. Postans, *Proc. Conf. Titanium '80, Science and Technology* (edited by H. Kimura and O. Izumi), Vol. I, pp. 429-439 (1980). T.M.S.-A.I.M.E., Warrendale, Pa (1980).

8 J. S. Park, S. H. Reichman and R. G. Broadwell, *Proc. Sixth World Conf. on Titanium* (edited by P. Lacombe, R. Tricot and G. Béranger), Cannes, France, Vol. III, pp. 1283-1288 (1988). Les Ulis Cedex, France (1989).

9 D. F. Neal, *Proc. Fifth World Conf. on Titanium* (edited by G. Lütjering, U. Zwicker and W. Bunk), Munich, Vol. III, pp. 1519-1526 (1984). Deutsche Gesellschaft für Metallkunde e.V., F.R.G. (1985).

10 P. J. Postans, *Metals Fight Back*, Rolls-Royce Reprint NR 90640. London, 17 October 1989.

11 E. W. Collings, *The Physical Metallurgy of Titanium Alloys* (edited by H. L. Gegel). A.S.M., Metals Park,

Ohio (1984).

12 C. Hammond and J. Nutting, *Forging and Properties of Aerospace Materials*, Leeds, U.K. pp. 75-102 (1977). T.M.S., London (1978).

13 M. J. Donachie Jr., *Titanium; A Technical Guide*. A.S.M., Metals Park, Ohio (1988).

14 D. Driver, *Metals and Materials* 1(6), 345 (1985).

15 J. A. Hall, *Proc. Conf. The Metallurgy of Light Alloys*, pp. 116-131. I.O.M. Conf. No. 20. (1983).

16 W. A. Baeslack III, D. W. Becker and F. H. Froes, *J. Metals* 36(5), 46 (1984).

17 R. Penelle, *Proc. Sixth World Conf. on Titanium* (edited by P. Lacombe, R. Tricot and G. Béranger), Cannes, France, Vol. III, pp. 1457-1465 (1988). Les Ulis Cedex, France (1989).

18 N. W. Kearns and J. E. Restall, *Proc. Sixth World Conf. on Titanium* (edited by P. Lacombe, R. Tricot and G. Béranger), Cannes, France, Vol. IV, pp. 1753-1758 (1988). Les Ulis Cedex, France (1989).

19 H. M. Flower, *Proc. Fifth World Conf. on Titanium* (edited by G. Lütjering, U. Zwicker and W. Bunk), Munich, Vol. III, pp. 1651-1658 (1984). Deutsche Gesellschaft für Metallkunde e.V., F.R.G. (1985).

20 G. W. Meetham, *Metall. Mater. Tech.* 8(11), 589 (1976).

21 C. H. Wells and C. P. Sullivan, *Trans. A.S.M.* 62, 263 (1969).

22 R. Brown and G. C. Smith, *Proc. Conf. Fatigue '81; Materials Experimentation and Design in Fatigue* (edited by F. Sherrat and J. B. Sturgeon), Warwick University, England, pp. 22-32 (1981). I.P.C. Science and Technology Press Ltd, Guildford (1981).

23 D. F. Neal and P. A. Blenkinsop, *Acta metall.* 24, 59 (1976).

24 J. Ruppen, P. Bhowel, D. Eylon and A. J. McEvily, *Proc. Conf. Fatigue Mechanisms* (edited by J. T. Fong), pp. 47-68. A.S.T.M.-S.T.P. 675 (1979).

25 C. M. Gilmore and M. A. Iman, *Proc. Conf. Titanium and Titanium Alloys; Scientific and Technological*

Aspects (edited by J. C. Williams and A.F. Belov), Moscow, U.S.S.R., **Vol. I**, pp. 637-648 (1976). Plenum Press, N.Y. (1982).

26 R. Brown and G. C. Smith, *Scripta metall.* **15**, 357 (1981).

27 R. Brown and G. C. Smith, *Metallography* **15**, 269 (1982).

28 P. J. Bania, *Proc. Sixth World Conf. on Titanium* (edited by P. Lacombe, R. Tricot and G. Béranger), Cannes, France, **Vol. II**, pp. 825-830 (1988). Les Ulis Cedex, France (1989).

29 P. J. Bania, *J. Metals* **40**(3), 20 (1988).

30 J. D. Alexander and M. Jezioro, *Proc. Sixth World Conf. on Titanium* (edited by P. Lacombe, R. Tricot and G. Béranger), Cannes, France, **Vol. III**, pp. 1151-1155 (1988). Les Ulis Cedex, France (1989).

31 D. F. Neal, *Proc. Sixth World Conf. on Titanium* (edited by P. Lacombe, R. Tricot and G. Béranger), Cannes, France, **Vol. I**, pp. 253-258 (1988). Les Ulis Cedex, France (1989).

32 M. T. Cope and M. J. Hill, *Proc. Sixth World Conf. on Titanium* (edited by P. Lacombe, R. Tricot and G. Béranger), Cannes, France, **Vol. I**, pp. 153-158 (1988). Les Ulis Cedex, France (1989).

33 P. S. Bate, P. L. Blackwell and J. W. Brooks, *Proc. Sixth World Conf. on Titanium* (edited by P. Lacombe, R. Tricot and G. Béranger), Cannes, France, **Vol. I**, pp. 287-292 (1988). Les Ulis Cedex, France (1989).

34 G. Sridhar, V. V. Kutumbarao and D. S. Sarma, *Metall. Trans.* **18A**, 877 (1987).

35 D. Eylon, *Scripta metall.* **12**, 349 (1978).

36 J. C. Williams, *Proc. Conf. Titanium Science and Technology* (edited by R. I. Jaffee and H. M. Burte), Cambridge, Massachusetts, **Vol. III**, pp. 1433-1494 (1972). T.M.S.-A.I.M.E., Plenum Press, N.Y. (1973).

37 A. T. K. Assadi, H. M. Flower and D. R. F. West, *Metals Tech.* **6**(1), 16 (1979).

38 F. S. Lin, E. A. Starke Jr., S. B. Chakrabortty and

A. Gysler, *Metall. Trans.* **15A**, 1229 (1984).

39 W. Cho, J. W. Jones, J. E. Allison and W. T. Donlon, *Proc. Sixth World Conf. on Titanium* (edited by P. Lacombe, R. Tricot and G. Béranger), Cannes, France, **Vol. I**, pp. 187-192 (1988). Les Ulis Cedex, France (1989).

40 D. Eylon and J. A. Hall, *Metall. Trans.* **8A**, 981 (1977).

41 I. W. Hall and C. Hammond, *Mater. Sci. Engng* **32**, 241 (1978).

42 D. Schechtman and D. Eylon, *Metall. Trans.* **9A**, 1018 (1978).

43 D. Eylon, *Metall. Trans.* **10A**, 311 (1979).

44 H. W. Rosenberg, *Proc. Conf. The Science, Technology and Applications of Titanium* (edited by R. I. Jaffee and N. E. Promisel), pp. 851-859 (1968). Pergamon Press, New York (1970).

45 D. F. Neal, *Proc. Sixth World Conf. on Titanium* (edited by P. Lacombe, R. Tricot and G. Béranger), Cannes, France, **Vol. I**, pp. 175-180 (1988). Les Ulis Cedex, France (1989).

46 K. C. Antony, *Trans. metall. Soc. A.I.M.E.* **242**, 1454 (1968).

47 H. M. Flower, P. R. Swann and D. R. F. West, *Metall. Trans.* **2**, 3289 (1971).

48 N. E. Paton, W. M. Mahoney, W. M. Paris and J. A. Hall, *Metall. Trans.* **7A**, 1685 (1976).

49 A. T. K. Assadi, H. M. Flower and D. R. F. West, *Metals Tech.* **6**(1), 8 (1979).

50 C. Ramachandra and V. Singh, *Metall. Trans.* **13A**, 771 (1982).

51 D. Banerjee, J. E. Allison, F. H. Froes and J. C. Williams, *Proc. Fifth World Conf. on Titanium* (edited by G. Lütjering, U. Zwicker and W. Bunk), Munich, **Vol. III**, pp. 1519-1526 (1984). Deutsche Gesellschaft für Metallkunde e.V., F.R.G. (1985).

52 C. Ramachandra and V. Singh, *Metall. Trans.* **16A**, 227 (1985).

53 S. R. Seagle, G. S. Hall and H. B. Bomberger, *Metals*

Engng Quart. **18**, 48 (1978).

54 M. R. Winstone, R. D. Rawlings and D. R. F. West, *J. Less Common Metals* **39**, 205 (1975).

55 H. M. Flower, K. Lipscombe and D. R. F. West, *J. Mater. Sci.* **17**, 1221 (1982).

56 L. S. Chumbley, B. C. Muddle and H. L. Fraser, *Acta metall.* **36**(2), 299 (1988).

57 G. McIntosh and T. N. Baker, *Phase Transformations '87* (edited by G. W. Lorimer) pp. 115-118. I.O.M. (1988).

58 A. P. Woodfield and M. H. Loretto, *Scripta metall.* **21**, 229 (1987).

59 G. McIntosh and T. N. Baker, *Proc. Sixth World Conf. on Titanium* (edited by P. Lacombe, R. Tricot and G. Béranger), Cannes, France, **Vol. III**, pp. 1571-1576 (1988). Les Ulis Cedex, France (1989).

60 D. Banerjee, *Scripta metall.* **21**, 1615 (1987).

61 C. Ramachandra and V. Singh, *Metall. Trans.* **23A**, 689 (1992).

62 S. Ankem, D. Banerjee, D. J. McNeish, J. C. Williams and S. R. Seagle, *Metall. Trans.* **18A**, 2015 (1987).

63 G. Sridhar and D. S. Sarma, *Metall. Trans.* **19A**, 3025 (1988).

64 A. P. Woodfield, P. J. Postans, M. H. Loretto and R. E. Smallman, *Acta metall.* **36**(3), 507 (1988).

65 C. Ramachandra and V. Singh, *J. Mater. Sci.* **23**, 835 (1988).

66 A. P. Woodfield, A. M. Wardle and M. H. Loretto, *Proc. Sixth World Conf. on Titanium* (edited by P. Lacombe, R. Tricot and G. Béranger), Cannes, France, **Vol. I**, pp. 357-362 (1988). Les Ulis Cedex, France (1989).

67 G. Sridhar and D. S. Sarma, *Metall. Trans.* **20A**, 55 (1989).

68 G. Sridhar and D. S. Sarma, *Metall. Trans.* **22A**, 1125 (1991).

69 C. G. Rhodes and J. C. Williams, *Metall. Trans.* **6A**, 1670 (1975).

70 C. G. Rhodes and N. E. Paton, *Metall. Trans.* **10A**, 209

(1979).

71 I. W. Hall, *Scand. J. Metals* **8**, 17 (1979).

72 P. Hallam and C. Hammond, *Proc. Conf. Titanium '80, Science and Technology* (edited by H. Kimura and O. Izumi), **Vol. II**, pp. 1435-1441 (1980). T.M.S.-A.I.M.E., Warrendale, Pa (1980).

73 I. W. Hall and C. Hammond, *Metal Sci.* **12**(7), 339 (1978).

74 G. F. Pittinato and W. D. Hanna, *Metall. Trans.* **3A**, 2905 (1972).

75 I. W. Hall, *Metall. Trans.* **9A**, 815 (1978).

76 I. W. Hall, *Scand. J. Metals* **7**, 277 (1978).

77 C. Hammond, R. A. Spurling and N. E. Paton, *Metall. Trans.* **15A**, 813 (1984).

78 G. C. Morgan and C. Hammond, *Proc. Conf. Titanium '80, Science and Technology* (edited by H. Kimura and O. Izumi), **Vol. II**, pp. 1443-1451 (1980). T.M.S.-A.I.M.E., Warrendale, Pa (1980).

79 D. Banerjee and V. S. Arunachalam, *Acta metall.* **29**, 1685 (1981).

80 D. Banerjee, *Metall. Trans.* **13A**, 681 (1982).

81 D. Banerjee and J. C. Williams, *Scripta metall.* **17**, 1125 (1983).

82 N. R. Moody, F. A. Greulich and S. L. Robinson, *Metall. Trans.* **15A**, 1955 (1984).

83 D. Banerjee, C. G. Rhodes and J. C. Williams, *Proc. Fifth World Conf. on Titanium* (edited by G. Lütjering, U. Zwicker and W. Bunk), Munich, **Vol. III**, pp. 1597-1604 (1984). Deutsche Gesellschaft für Metallkunde e.V., F.R.G. (1985).

84 G. H. Isaac and C. Hammond, *Proc. Fifth World Conf. on Titanium* (edited by G. Lütjering, U. Zwicker and W. Bunk), Munich, **Vol. III**, pp. 1605-1612 (1984). Deutsche Gesellschaft für Metallkunde e.V., F.R.G. (1985).

85 D. Banerjee, C. G. Shelton, B. Ralph and J. C. Williams, *Acta metall.* **36**(1), 125 (1988).

86 C. Servant, C. Quesne, T. Baudin and R. Penelle, *J. Mater. Res.* **6**(5), 987 (1991).

87 H. Margolin, E. Levine and M. Young, *Metall. Trans.* **8A**, 373 (1977).

88 C. G. Shelton and B. Ralph, *Proc. Conf. The Metallurgy of Light Alloys*, pp. 180-183. I.S.O.M. Conf. No. 20. (1983).

89 R. A. Spurling, C. G. Rhodes and J. C. Williams, *Metall. Trans.* **5A**, 2597 (1979).

90 C. Ramachandra, A. K. Singh and G. M. K. Sarma, *Metall. Trans.* **24A**, 1273 (1993).

91 M. W. Kearns, *Proc. Conf. The Metallurgy of Light Alloys*, pp. 105-110. I.S.O.M. Conf. No. 20. (1983).

92 P. J. Postans and R. H. Jeal, *Proc. Conf. Titanium '80, Science and Technology* (edited by H. Kimura and O. Izumi), **Vol. I**, pp. 441-455 (1980). T.M.S.-A.I.M.E., Warrendale, Pa (1980).

93 J. A. Hall, C. M. Pierce, D. L. Ruckle and R. A. Sprague, *Mater. Sci. Engng* **9**, 197 (1972).

94 S. R. Seagle and L. J. Bartlo, *Metals Engng Quart.* **8**, 1 (1968).

95 D. Eylon, J. A. Hall, C. M. Pierce and D. L. Ruckle, *Metall. Trans.* **7A**, 1817 (1976).

96 D. Banerjee, D. Mukherjee, R. L. Saha and K. Bose, *Metall. Trans.* **14A**, 413 (1983).

97 N. D. R. Goddard, Ph.D. thesis, Imperial College of Science and Technology, London (1988).

98 H. M. Flower, *Mater. Sci. Tech.* **6**, 1082 (1990).

99 S. Saal, L. Wagner, G. Lütjering, H. Pillhofer and M. A. Daeubler, *Z. Metallk.* **81**, 535 (1990).

100 H. Conrad, *Progr. Mater. Sci.* **26**, 123 (1982).

101 A.S.T.M. Designation E399-83, Book of A.S.T.M. Standards, Vol. 03.01 (1988).

102 R. W. Gardiner, *Proc. Conf. The Metallurgy of Light Alloys*, pp. 245-251. I.S.O.M. Conf. No. 20. (1983).

103 I. W. Hall and C. Hammond, *Proc. Conf. Titanium and Titanium Alloys, Scientific and Technological Aspects* (edited by J. C. Williams and A. F. Belov), Moscow, U.S.S.R., pp. 601-613 (1976). Plenum Press, New York (1982).

104 K.S. Chan and D.A. Koss, *Mater. Sci. Engng* **43**, 177

(1980).

105 I. W. Hall and C. Hammond, *Proc. Conf. Titanium Science and Technology* (edited by R. I. Jaffee and H. M. Burte), Cambridge, Massachusetts, **Vol. II**, pp. 1365-1376 (1972). T.M.S.-A.I.M.E., Plenum Press, N.Y. (1973).

106 A. W. Bowen, *Acta metall.* **26**, 1423 (1978).

107 P. G. Partridge, *Review 118, Metals Mater.* **1**(387), 169 (1967).

108 D. Hull and D. J. Bacon, *Introduction to Dislocations*, Third Edition, pp. 112-140 (1984). Pergamon press (1992).

109 A. T. Churchman, *Proc. R. Soc. A* **226**, 216 (1954).

110 D. N. Williams and D. S. Eppelscheimer, *J. Inst. Metals* **81**, 553 (1952-3).

111 F. D. Rosi, C. A. Dube and B. H. Alexander, *T.M.S.-A.I.M.E. J. Metals* **197**, 257 (1953).

112 E. A. Anderson, D. C. Jillson and S. R. Dunbar, *T.M.S.-A.I.M.E. J. Metals* **197**, 1191 (1953).

113 C. J. Beevers and J. L. Robinson, *J. Less Common Metals* **17**, 345 (1969).

114 G. I. Taylor, *J. Inst. Metals* **62**(1), 307 (1938).

115 U. F. Kocks, *Acta metall.* **6**, 85 (1958).

116 G. W. Groves and A. Kelly, *Phil. Mag.* **8**, 877 (1966).

117 W. J. McG. Tegart, *Phil. Mag.* **9**, 339 (1964).

118 M. J. Blackburn and J. C. Williams, *Trans. A.S.M.* **62**, 398 (1969).

119 N. E. Paton and W. A. Backofen, *Metall. Trans.* **1**, 2839 (1970).

120 M. A. W. Lowden and W. B. Hutchinson, *Metall. Trans.* **6A**, 441 (1975).

121 K. S. Chan, C. C. Wojcik and D. A. Koss, *Metall. Trans.* **12A**, 1899 (1981).

122 H. Numakura, Y. Minonishi and M. Koiwa, *Scripta metall.* **20**, 1581 (1986).

123 A. W. Bowen, *Proc. Sixth World Conf. on Titanium* (edited by P. Lacombe, R. Tricot and G. Béranger), Cannes, France, **Vol. I**, pp. 93-98 (1988). Les Ulis Cedex, France (1989).

124 E. D. Levine, *Trans. metall. Soc. A.I.M.E.* **236**, 1558 (1966).

125 R. Zeyfang, R. Martin and H. Conrad, *Mater. Sci. Engng* **8**, 134 (1971).

126 G. Sargent and H. Conrad, *Scripta metall.* **3**, 43 (1969).

127 T. Tanaka and H. Conrad, *Acta metall.* **20**, 1019 (1972).

128 A. Akhtar and E. Teghtsoonian, *Metall. Trans.* **6A**, 2201 (1975).

129 J. C. Williams and G. Lütjering, *Proc. Conf. Titanium '80, Science and Technology* (edited by H. Kimura and O. Izumi), **Vol. I**, pp 671-681 (1980). T.M.S.-A.I.M.E., Warrendale, Pa (1980).

130 K. J. Miller, *J. Mech. Engng Sci.* **205**(C5), 291 (1991). I.Mech.E. Proc.C, 27th *John Player Lecture*, pp. 1-13 (1991).

131 M. A. Daeubler and D. Helm, *Proc. Conf. High Temperature Materials for Power Engineering*, Liege, Belgium, **Vol. II**, pp. 1717-1726 (1990).

132 K. J. Miller, *Fatigue Fract. Engng Mater. Structures* **10**, 75 (1987).

133 P. P. Benham and R. J. Crawford, *Mechanics of Engineering Materials*, Fifth Impression (1991). Longman Singapore Publishers, Pte Ltd, Singapore (1991).

134 K. J. Miller, *Fatigue Fract. Engng Mater. Structures* **10**, 93 (1987).

135 A. W. Funkenbusche and L. F. Coffin, *Metall. Trans.* **9A**, 1159 (1978).

136 M. R. Lin, M. E. Fine and T. Mura, *Acta metall.* **34**, 619 (1986).

137 J. W. Provan, *Proc. 10th Canadian Fract. Conf.*, Waterloo, Ontario, Canada, pp. 131-154 (1983).

138 J. W. Provan and Z. H. Zhai, *Proc. 11th Canadian Fract. Conf.*, Waterloo, Ontario, Canada, pp. 201-212 (1984).

139 D. Jun and Q. Jianchen, *Fatigue Fract. Engng Mater. Structures* **12**, 627 (1989).

140 J. Polák, *Mater. Sci. Engng* **92**, 71 (1980).
141 Z. S. Basinski and S. J. Basinski, *Acta metall.* **33**, 1307 (1985).
142 Z. S. Basinski and S. J. Basinski, *Acta metall.* **33**, 1319 (1985).
143 A. Hunsche and P. Neumann, *Acta metall.* **34**, 207 (1986).
144 G. Venkataraman, Y. W. Chung and T. Mura, *Acta metall. mater.* **39**, 2631 (1991).
145 J. A. Ewing and J. C. W. Humfrey, *Phil. Trans. R. Soc.* **A200**, 241 (1903).
146 D. F. Watt, J. D. Embury and R. K. Ham, *Phil. Mag.* **17**, 199 (1968).
147 D. Kuhlman-Wilsdorf and C. Laird, *Mater. Sci. Engng* **46**, 209 (1980).
148 J. Polák, T. Lepistö and P. Kettunen, *Mater. Sci. Engng*, **74**, 85 (1985).
149 P. Lukás, L. Kunz, Z. Knézl, B. Weiss and R. Stickler, *Mater. Sci. Engng* **70**, 91 (1985).
150 J. Polák and P. Liskutín, *Fatigue Fract. Engng Mater. Structures* **13**, 119 (1990).
151 J. G. Antonopoulos and A. T. Winter, *Phil. Mag.* **33**, 87 (1976).
152 P. G. Partridge, *Phil. Mag.* **12**, 1043 (1965).
153 R. Stevenson and J. E. Breedis, *Acta Metall.* **23**, 1419 (1975).
154 M. Sugano and C. M. Gilmore, *Metall. Trans.* **11**, 539 (1980).
155 A. Suhua, W. Zhongguang and X. Yeubo, *Scripta metall.* **19**, 1089 (1985).
156 D. E. MacDonald and W. A. Wood, *J. Inst. Metals* **100**, 73 (1972).
157 D. Munz, V. Bachman and H. Rachmanto, *Mater. Sci. Engng* **8**, 244 (1971).
158 D. Munz, *Engng Fract. Mechanics* **5**, 353 (1973).
159 N. E. Paton, J. C. Williams and G. P. Rauscher, *Proc. Conf. Titanium Science and Technology* (edited by R. I. Jaffee and H. M. Burte), Cambridge, Massachusetts, **Vol. II**, pp. 1049-1069 (1972).

T.M.S.-A.I.M.E., Plenum Press, N.Y. (1973).

160 H. Numukara, Y. Minonishi and M. Koiwa, *Phil. Mag.* **63A**, 785 (1991).

161 G. R. Yoder, L. A. Cooley and T. W. Crooker, *Metall. Trans.* **8A**, 1737 (1977).

162 K. S. Ravichandran, E. S. Dwarakasada and D. Banerjee, *Scripta metall.* **25**, 2115 (1991).

163 R. B. Sparks and J. R. Long, *A.F.M.L. Report TR73-0301* (1974).

164 C. C. Wojcik, K. S. Chan and D. A. Koss, *Acta metall.* **36**, 1261 (1988).

165 Y. Mahajan and H. Margolin, *Metall. Trans.* **13A**, 257 (1982).

166 Y. Mahajan and H. Margolin, *Metall. Trans.* **13A**, 269 (1982).

167 L. Wagner and G. Lütjering, *Proc. Sixth World Conf. on Titanium* (edited by P. Lacombe, R. Tricot and G. Béranger), Cannes, France, **Vol. I**, pp. 345-350 (1988). Les Ulis Cedex, France (1989).

168 A. L. Dowson, A. C. Hollis and C. J. Beevers, *Int. J. Fatigue* **14**, 261 (1992).

169 A. L. Dowson, C. J. Beevers and L. Grabowski, *Proc. Seventh World Conf. on Titanium*, California, (1992). To be published.

170 M. A. Hicks and C. W. Brown, *Int. J. Fatigue* **4**, 167 (1982).

171 K. S. Ravichandran, *Acta metall.* **39**, 401 (1991).

172 G. R. Yoder and D. Eylon, *Metall. Trans.* **10A**, 1808 (1979).

173 J. T. Ryder, D. E. Pettit, W. E. Krupp and D. W. Hoeppner, *Final Report on Evaluation of Mechanical Property Characteristics of IMI 685*, Lockheed-California Company, Rye Canyon Laboratory (1973).

174 P. J. Postans and R. H. Jeal, *Forging and Properties of Aerospace Materials*, Leeds, U.K. pp. 192-198 (1977). T.M.S., London (1978).

175 W. J. Evans and C. R. Gostelow, *Metall. Trans.* **10A**, 1837 (1979).

176 P. J. Bania and D. Eylon, *Metall. Trans.* **9A**, 847 (1978).

177 W. J. Evans, *Scripta metall.* **21**, 469 (1987).

178 J. White, M. H. Loretto, R. E. Smallman and M. R. Winstone, *Proc. Fifth World Conf. on Titanium* (edited by G. Lütjering, U. Zwicker and W. Bunk), Munich 1984, **Vol. IV**, pp. 2297-2304 (1984). Deutsche Gesellschaft Für Metallkunde e.V., F.R.G. (1985).

179 C. A. Stubbington and S. Pearson, *Engng Fract. Mech.* **10**, 723 (1978).

180 D. L. Davidson and D. Eylon, *Metall. Trans.* **11A**, 737 (1980).

181 W. J. Evans, *Strength of Materials and Alloys* (ICMA8), Tampere, Finland, **Vol. 2**, pp. 659-664 (1988).

182 J. E. Hack and G. R. Leverant, *Metall. Trans.* **13A**, 1729 (1982).

183 W. J. Evans, *J. Mater. Sci. Letters* **6**, 571 (1978).

184 W. J. Evans, *Proc. Third Int. Conf. Creep and Fracture Engng Mater. Structures*, Swansea (1987).

185 P. J. Goodhew, *Thin Foil Preparation for Electron Microscopy* (edited by A. M. Glauert), pp. 139-153. Elsevier, Oxford (1985).

186 S. B. Newcombe, W. M. Stobbs and C. B. Boothroyd, *J. Microscopy* **140**, 195 (1985).

187 S. B. Newcombe, C. S. Baxter and E. G. Bithell, *Inst. Phys. Conf. Ser.*, **No. 93** : Volume 1. Euram. (1988).

188 J. C. Chesnutt and J. C. Williams, *Metall. Trans.* **8A**, 514 (1977).

189 A. C. Pickard, *The Application of 3-Dimensional Finite Element Methods to Fracture Mechanics and Fatigue Life Prediction*, EMAS Ltd, Chapter 6, (1986). Chameleon Press Ltd., London, U.K. (1986).

190 B. Borchert and M. A. Daeubler, *Proc. Sixth World Conf. on Titanium* (edited by P. Lacombe, R. Tricot and G. Béranger), Cannes, France, **Vol. I**, pp. 467-472 (1988). Les Ulis Cedex, France (1989).

191 B. Shollock, *Rolls-Royce Research Brochure* PVJ2-118D (RGR 10088) Final Report, University of Oxford

(1991).

192 M. A. Daeubler, D. Helm and D. F. Neal, *Proc. 1990 Int. Conf. on Titanium Products and Applications*, **1**, pp. 78-87. Titanium Development Assoc. Dayton, Ohio (1990).

193 X-ray powder data file (edited by J. V. Smith), Inorganic Vol. PD1S 5iRB, 5-682. A.S.T.M. Pennsylvania (1967).

194 W. B. Pearson, *International Series of Monographs on Metal Physics and Physical Metallurgy,* **Vol. 4**, *A Handbook of Lattice Spacings and Structures of Metals and Alloys* (edited by G. V. Raynor), 1044. Pergamon Press, London (1958).

195 R. M. Powers and H. A. Wilhelm, *U.S. A.E.C. Publ. ISC* **228**, (1952).

196 B. W. Levinger, *J. Metals* **5**, 195 (1953).

197 G. Welsch, G. Lütjering, K. Gazioglu and W. Bunk, *Metall. Trans.* **8A**, 169 (1977).

198 A. P. Woodfield, M. H. Loretto and R. E. Smallman, *Proc. Fifth World Conf. on Titanium* (edited by G. Lütjering, U. Zwicker and W. Bunk), Munich, **Vol. III**, pp. 1527-1534 (1984). Deutsche Gesellschaft für Metallkunde e.V., F.R.G. (1985).

199 A. P. Woodfield, J. White and M. H. Loretto, *Scripta metall.* **19**, 33 (1985).

200 L. Zhang and Z. Li, *Mater. Sci. Engng* **A113**, 185 (1989).

201 S. P. Agrawal, G. A. Sargent and H. Conrad, *Metall. Trans.* **5**, 2415 (1974).

202 N. M. Grinberg, E. N. Aleksenko, V. A. Moskalenko, A. R. Smirnov, L. F. Yakovenko, A. V. Mozhaev and I. A. Arinushkin, *Mater. Sci. Engng* **A165**, 117 (1993).

203 D. J. Smith, *Proc. Sixth World Conf. on Titanium* (edited by P. Lacombe, R. Tricot and G. Béranger), Cannes, France, **Vol. III**, pp. 1277-1281 (1988). Les Ulis Cedex, France (1989).

204 M. A. Daeubler and D. Helm, *Proc. Conf. MTU Titanium 1990: Products and Applications*, Florida, U.S.A. **Vol 1**, pp. 244-255 (1990). Titanium Development Assoc.,

P.O. Box 2503, Dayton, Ohio (1990).

205 J. R. Yates, Final Report for Rolls-Royce Brochure B1J1-81D SMP 1058/3 (1990).

206 R. J. Wanhill, R. Galatolo and C. E. W. Looije, National Aerospace Laboratory (Netherlands) pp. 1-30. N90-11877/9/XAB, 30 June 1988.

207 A. W. Thompson, J. D. Frandsen and J. C. Williams, *Metals Science* **9**, 46 (1975).

208 G. T. Hahn, R. G. Hoagland and A. R. Rosenfield, *Metall. Trans.* **3**, 1189 (1972).

209 P. E. Irving and C. J. Beevers, *Metall. Trans.* **5**, 391 (1974).

210 H. Conrad, M. Doner and B. de Meester, *Proc. Conf. Titanium Science and Technology* (edited by R. I. Jaffee and H. M. Burte), Cambridge, Massachusetts, **Vol. II**, pp. 969-1005 (1972). T.M.S.-A.I.M.E., Plenum Press, N.Y. (1973).

211 W. J. Evans, *Proc. Second Int. Conf. Creep and Fracture Engng Mater. Structures*, Swansea (1986).

212 N. E. Paton and R. A. Spurling, *Metall. Trans.* **7A**, 1769 (1976).

213 J. Y. Lim, C. J. McMahon Jr., D. P. Pope and J. C. Williams, *Metall. Trans.* **7A**, 139 (1976).

214 S. J. Vijayakar, E. S. K. Menon, S. Banerjee and R. Krishnan, *Proc. Conf. Titanium '80, Science and Technology* (edited by H. Kimura and O. Izumi), **Vol. II**, pp. 1221-1230 (1980). T.M.S.-A.I.M.E., Warrendale, Pa (1980).

215 A. Gysler and S. Weissman, *Mater. Sci. Engng* **27**, 181 (1977).

216 G. Lütjering and S. Weissman, *Acta metall.* **18**, 785 (1970).

217 Z. Liu and G. Welsch, *Proc. Sixth World Conf. on Titanium* (edited by P. Lacombe, R. Tricot and G. Béranger), Cannes, France, **Vol. I**, pp. 99-104 (1988). Les Ulis Cedex, France (1989).

218 D. A. Koss and K. S. Chan, *Acta metall.* **28**, 1245 (1980).

219 R. J. H. Wanhill, *Acta metall.* **21**, 1253 (1973).

220 D. Hoeppner, *Metallography* **11**, 129 (1978).

221 C. M. Ward-Close and C. J. Beevers, *Metall. Trans.* **11A**, 1007 (1980).

222 D. A. Meyn, *Metall. Trans.* **5**, 2405 (1974).

223 G. Terlinde and G. Lütjering, *Metall. Trans.* **13A**, 1283 (1982).

224 Y. Krishna, M. Rao, V. V. K. Rao and P. R. Rao, *Mater. Sci. Engng* **A110**, 193 (1989).

ACKNOWLEDGEMENTS

Firstly, I would like to thank my supervisor Dr Mark Rainforth for the organisation of this project and for his encouragement, help and support throughout the course of my PhD.

I am grateful to Dr Leon Grabowski for the set up of the project and for his collaboration during the last three years. The provision of test specimens by Rolls-Royce and the financial support of both Rolls-Royce and the Science and Engineering Research Council are acknowledged.

Special thanks are given to Dr P. Korgul and Dr M. Al Khafaji for their help with T.E.M. analysis and the technical staff in the Department of Engineering Materials, particularly Dave Manvell for help with the mechanical testing and Dawn for assistance with the preparation of specimens for electron microscopy.

The support and encouragement (particularly laterly) of my fellow researchers, in both the electron microscopy and hot-working groups, are valued.

I would like to thank my parents and Alan for their understanding of the task undertaken. Finally, and most importantly, I am deeply indebted to Nicky for her interest and constant encouragement throughout the whole PhD and for the thorough proof reading of this thesis.

APPENDIX 1

BURGERS VECTOR CALCULATIONS

Reflection		Burgers vectors of perfect dislocations ($\times \frac{1}{2}$)									
		$\pm[11\bar{2}0]$	$\pm[\bar{1}2\bar{1}0]$	$\pm[\bar{2}110]$	$\pm[11\bar{2}3]$	$\pm[\bar{1}2\bar{1}3]$	$\pm[\bar{2}113]$	$\pm[11\bar{2}\bar{3}]$	$\pm[\bar{1}2\bar{1}\bar{3}]$	$\pm[\bar{2}11\bar{3}]$	$\pm[0003]$
1	$10\bar{1}0$	±1	0	∓1	±1	0	∓1	±1	0	∓1	0
	$01\bar{1}0$	±1	±1	0	±1	±1	0	±1	±1	0	0
	$\bar{1}100$	0	±1	±1	0	±1	±1	0	±1	±1	0
2	0002	0	0	0	±2	±2	±2	∓2	∓2	∓2	±2
3	$10\bar{1}1$	±1	0	∓1	±2	±1	0	0	∓1	∓2	±1
	$10\bar{1}\bar{1}$	±1	0	∓1	0	∓1	∓2	±2	±1	0	∓1
	$01\bar{1}1$	±1	±1	0	±2	±2	±1	0	0	∓1	±1
	$01\bar{1}\bar{1}$	±1	±1	0	0	0	∓1	±2	±2	±1	∓1
	$\bar{1}101$	0	±1	±1	±1	±2	±2	∓1	0	0	±1
	$\bar{1}10\bar{1}$	0	±1	±1	∓1	0	0	±1	±2	±2	∓1
4	$10\bar{1}2$	±1	0	±1	±3	±2	±1	∓1	∓2	∓3	±2
	$10\bar{1}\bar{2}$	±1	0	±1	∓1	∓2	∓3	±3	±2	±1	∓2
	$01\bar{1}2$	±1	±1	0	±3	±3	±2	∓1	∓1	∓2	±2
	$01\bar{1}\bar{2}$	±1	±1	0	∓1	∓1	∓2	±3	±3	±2	∓2
	$\bar{1}102$	0	±1	±1	±2	±3	±3	∓2	∓1	∓1	±2
	$\bar{1}10\bar{2}$	0	±1	±1	∓2	∓1	∓1	±2	±3	±3	∓2
5	$11\bar{2}0$	±2	±1	∓1	±2	±1	∓1	±2	±1	∓1	0
	$\bar{1}21\bar{0}$	±1	±2	±1	±1	±2	±1	±1	±2	±1	0
	$\bar{2}110$	∓1	±1	±2	∓1	±1	±2	∓1	±1	±2	0
6	$10\bar{1}3$	±1	0	∓1	±4	±3	±2	∓2	∓3	∓4	±3
	$10\bar{1}\bar{3}$	±1	0	∓1	∓2	∓3	∓4	±4	∓3	±2	∓3
	$01\bar{1}3$	±1	±1	0	±4	±4	±3	∓2	±4	∓3	±3
	$01\bar{1}\bar{3}$	±1	±1	0	∓2	∓2	∓3	±4	∓2	±3	∓3
	$\bar{1}103$	0	±1	±1	±3	±4	±4	∓3	±4	∓2	±3
	$\bar{1}10\bar{3}$	0	±1	±1	∓3	∓2	∓2	±3	∓2	±4	∓3
7	$11\bar{2}2$	±2	±1	∓1	±4	±3	±1	0	∓1	∓3	±2
	$11\bar{2}\bar{2}$	±2	∓1	∓1	0	∓1	∓3	±4	±3	±1	∓2
	$\bar{1}21\bar{2}$	±1	±2	±1	±3	±4	±3	∓1	0	∓1	±2
	$\bar{1}21\bar{2}$	±1	±2	±1	∓1	0	∓1	±3	0	±3	∓2
	$\bar{2}112$	∓1	±1	±2	±1	±3	±4	∓3	±3	0	±2
	$\bar{2}11\bar{2}$	∓1	±1	±2	∓3	∓1	0	±1	±1	±4	∓2

Values of $\underline{g}.\underline{b}$ for the first seven reflections and $1/3\langle 11\bar{2}0\rangle$, $1/3\langle 11\bar{2}3\rangle$ and $\langle 0001\rangle$ type Burgers vectors- [107].

APPENDIX 2

CALCULATION OF F_{max} AND F_{mean}

The second moment of area,

$$I = bd^3/12 \ (m^4) \qquad (1)$$

where: b = specimen breadth (m)
d = specimen depth (m)

The bending moment,

$$M = \sigma_{ps} I/y \ (Nm) \qquad (2)$$

where: σ_{ps} = 0.2% P.S. stress (N/m^2)
y = specimen centre-line depth (m)
or depth of neutral axis
= d/2 (m).

The maximum load required,

$$F_{max} = 2MA/100a \ (N) \qquad (3)$$

where: A = percent of 0.2% P.S. (σ_{ps}).
a = separation of outer and inner rollers (m)
= 17.5×10^{-3} m (see Figure 3.5).

From equations 1 to 3 and substituting for a;

$$F_{max} = 0.1905\sigma_{ps} bd^2 A \ (N) \qquad (4)$$

From R = 0.1, it follows that;

$$F_{min} = F_{max}/10 \qquad (5)$$

and therefore;

$$F_{mean} = (F_{max} - F_{max}/10)/2$$
$$F_{mean} = 0.0857\sigma_{ps} bd^2 A \ (N) \qquad (6)$$

APPENDIX 3

CALCULATION OF DIMPLE DEPTH

(1) The average diameter, d (μm), of the dimple at the surface of the disc was calculated using a travelling microscope. The radius, r = d/2.

(2) The diameter, D (μm), of the tool used for dimpling was measured with a micrometer. The radius, R = D/2.

(3) The depth of the dimple was designated as δ:

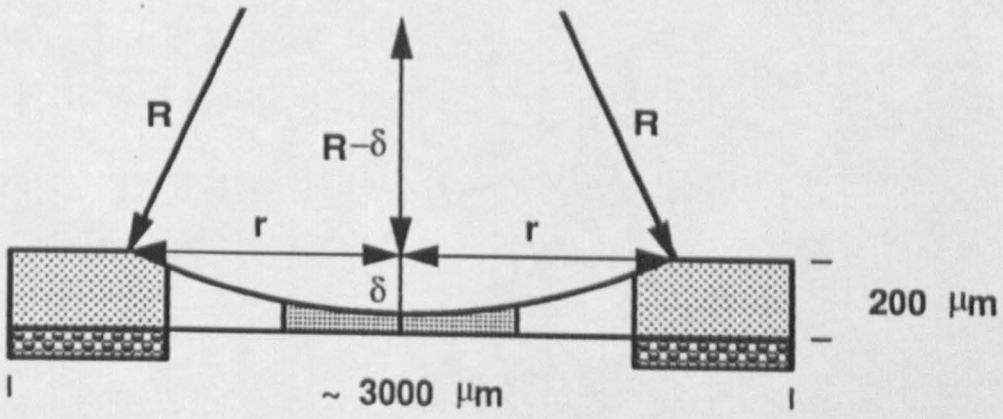

(4) By Pythagoras; $R^2 = (R-\delta)^2 + r^2$

The radius of the tool, R, used for dimpling was 7095 μm. From this value, a conversion table was drawn up which compared the depth, d, of the dimple with the diameter, d, of the dimple at the disc surface.

d (μm)	1000	2000	2100	2200	2300	2400	2500	2600	2700	2800
δ (μm)	17	71	78	86	94	102	111	120	130	140

Thus, for a dimple 120 μm in depth, a diameter, d, of 2600 μm was required at the disc surface. It was important to re-check the diameter, D, of the dimpling tool each time it was used so that these figures could be altered if the tool had been worn during any intervening period.